Photovoltaic Neural Interfaces Based on Nanowires and Quantum Dots to Restore Vision

by

Tarık Safa Kaya

A Dissertation Submitted to the
Graduate School of Sciences and Engineering
in Partial Fulfillment of the Requirements for
the Degree of

Master of Science

in

Materials Science and Engineering

KOÇ ÜNİVERSİTESİ

July 30, 2025

Photovoltaic Neural Interfaces Based on Nanowires and Quantum Dots to Restore Vision

Koç University

Graduate School of Sciences and Engineering

This is to certify that I have examined this copy of a master's thesis by

Tarık Safa Kaya

and have found that it is complete and satisfactory in all respects,
and that any and all revisions required by the final
examining committee have been made.

Committee Members:

_____

Prof. Sedat Nizamoğlu (Advisor)

_____

Prof. Önder Metin

_____

Assoc. Prof. Caner Ünlü

Date: _____

To my mom, the heart behind all my dreams...

ABSTRACT

Photovoltaic Neural Interfaces Based on Nanowires and Quantum Dots to Restore Vision

Tarık Safa Kaya

Master of Science in Materials Science and Engineering

July 30, 2025

Optoelectronic biointerfaces have emerged as a promising platform for controlling the nervous system at the cellular, tissue, and organ levels with potential clinical applications via transduction of light energy to ionic currents. In this thesis, we presented a solution-processed photovoltaic nanoassembly comprising a ZnO nanowire (NW) array sensitized with $AgBiS_2$ nanocrystals that enables efficient near-infrared (NIR) neural stimulation through capacitive photocurrents. Nanowires have served as a transformative platform for advanced neural and tissue interfaces. While their photovoltaic properties hold exceptional promise for neural modulation, existing photostimulation approaches predominantly rely on visible-light-activated photoelectrochemical mechanisms. By optimizing nanowire morphology and nanocrystal interdigitation, the platform achieved high charge injection densities (tens of μC cm^{-2}) at low NIR intensities (<1 mW mm^{-2}). The nanoassembly was subretinally placed in an ex-vivo blind rat retina, where it elicited repeatable and robust responses in retinal ganglion cells (RGCs) under NIR pulses. Notably, these responses were achieved at light intensities significantly below established ocular safety limits. We further demonstrated a bioelectronic design where $AgBiS_2$ quantum dots (QDs) served as the photoabsorption material, hole transport medium, and pseudocapacitive electrode–electrolyte interface. The power-law behavior of the anodic and cathodic peaks suggested that diffusion-controlled and capacitive processes contributed to the charge storage mechanism. Furthermore, 3D Bode capacitance maps and phase angle responses indicated a high capacitance of 3.3 mF cm^{-2} at the half-wave potential (0.044 V vs Ag/AgCl) in artificial cerebrospinal fluid (aCSF). For efficient transduction of light to electrical stimulation, $AgBiS_2$ QDs are embedded onto ZnO NWs in a photovoltaic device architecture, which produced twice the photocurrent (1.9±0.3 mA cm^{-2}) and nearly three times the charge injection (29±2.3 μC

cm^{-2}) compared to the planar devices without NWs. Moreover, photostimulation of hippocampal neurons was demonstrated on the device without inducing significant oxidative stress. Collectively, these findings demonstrated an unconventional and efficient bioelectronic device via pseudocapacitive optoelectronic nanocrystals, as well as the nexus of neuronal systems and nanoassemblies, which offers significant potential for enabling unconventional visual prosthetics and advanced neuromodulation therapies. Notably, proven efficacy in eliciting retinal responses within ex vivo models of retinal degeneration underscores its potential for next-generation visual prosthetics and broader neuromodulation applications.

ÖZETÇE

Görüşü Yeniden Kazandırmak İçin Nanotel ve Kuantum Nokta Tabanlı Fotovoltaik Nöral Arayüzler

Tarık Safa Kaya

Malzeme Bilimi ve Mühendisliği, Yüksek Lisans

30 Temmuz 2025

Optoelektronik biyoarayüzler, ışık enerjisinin iyonik akımlara dönüştürülmesi yoluyla sinir sisteminin hücresel, doku ve organ seviyelerinde kontrol edilmesi için klinik uygulama potansiyeli taşıyan umut verici bir platform olarak ortaya çıkmıştır. Bu tezde, $AgBiS_2$ nanokristalleri ile duyarlılaştırılmış bir ZnO nanotel (NW) dizisinden oluşan çözelti işlemeli bir fotovoltaik nano-yapı sunulmuştur. Bu yapı, kapasitif fotoakım yoluyla verimli yakın kızılötesi (NIR) nöral uyarım sağlamaktadır. Nanoteller, gelişmiş sinir ve doku arayüzleri için dönüştürücü bir platform görevi görmüştür. Fotovoltaik özellikleri nöral modülasyon için olağanüstü potansiyel taşırken, mevcut fotostimülasyon yaklaşımları ağırlıklı olarak görünür ışıkla aktive olan fotoelektrokimyasal mekanizmalara dayanmaktadır. Nanotel morfolojisinin ve nanokristal iç içe geçme yapısının optimize edilmesiyle, bu platform düşük NIR yoğunluklarında (<1 mW mm^{-2}) yüksek yük enjeksiyon yoğunlukları (onlarca µC cm^{-2}) elde etmiştir. Nano-yapı, ex-vivo kör sıçan retinasında subretinal olarak yerleştirilmiş ve NIR darbeleri altında retinal ganglion hücrelerinde (RGC'ler) tekrarlanabilir ve güçlü yanıtlar oluşturmuştur. Özellikle, bu yanıtlar, göz güvenlik sınırlarının önemli ölçüde altındaki ışık şiddetlerinde elde edilmiştir. Ayrıca, bu çalışmada $AgBiS_2$ kuantum noktalarının (QD'ler) ışık emilim malzemesi, deşik taşıma ortamı ve psödokapasitif elektrot-elektrolit arayüzü olarak görev yaptığı bir biyoelektronik tasarım sunulmuştur. Anodik ve katodik piklerin üstel davranışı, yük depolama mekanizmasına difüzyon kontrollü ve kapasitif süreçlerin katkıda bulunduğunu göstermiştir. Ayrıca, 3D Bode kapasitans haritaları ve faz açısı yanıtları, yapay beyin-omurilik sıvısında (aCSF) yarım-dalga potansiyelinde (0.044 V vs Ag/AgCl) 3.3 mF cm^{-2} gibi yüksek bir kapasitans değeri olduğunu ortaya koymuştur. Işığın elektriksel uyarıma verimli dönüşümü için, $AgBiS_2$ QD'ler, ZnO NW'ler ile bir fotovoltaik cihaz mimarisine gömülmüş olup, NW içermeyen düzlemsel cihazlara kıyasla iki kat daha fazla foto-

akım (1.9 ± 0.3 mA cm^{-2}) ve yaklaşık üç kat daha fazla yük enjeksiyonu (29 ± 2.3 µC cm^{-2}) sağlamıştır. Üstelik, bu cihaz üzerinde hipokampal nöronların fotostimülasyonu, önemli oksidatif stres oluşturmadan gerçekleştirilmiştir. Sonuç olarak, bu bulgular, psödokapasitif optoelektronik nanokristaller aracılığıyla alışılmadık ve verimli bir biyoelektronik cihazın yanı sıra nöronal sistemler ile nano-yapıların kesişimini ortaya koymuştur. Bu yaklaşım, alışılmadık görsel protezler ve ileri nöromodülasyon terapileri için önemli potansiyel sunmaktadır. Özellikle, retinal dejenerasyonun ex-vivo modellerinde retinal yanıtların uyarılmasındaki kanıtlanmış etkinlik, yeni nesil görsel protezler ve daha geniş nöromodülasyon uygulamaları için umut vaat etmektedir.

ACKNOWLEDGMENTS

First and foremost, I would like to express my deepest gratitude to my supervisor, Prof. Sedat Nizamoğlu, the head of the Innovative DEvices and InterfAces LABoratory (IDEALAB) at Koç University. From our very first meeting, when I expressed my desire to reach my full potential, he assured me that this was precisely the goal of his lab. In the last three years, he not only provided me with an exceptional research environment characterized by high academic standards but also offered unwavering support, invaluable guidance, and immense patience throughout my MSc journey. I am profoundly grateful for the trust he placed in me by entrusting me with key projects, which continually challenged me to push my limits and strive for excellence. It has been both a privilege and an honor to be a member of his research group, and for that, I owe him my sincerest thanks.

I would like to express my sincere gratitude to my thesis committee members, Prof. Önder Metin and Assoc. Prof. Caner Ünlü, for their invaluable guidance, insightful suggestions, and valuable time.

I would like to extend my deepest gratitude to my collaborators for their invaluable scientific contributions to our joint research and projects. My sincere thanks go to Prof. Rezan Demir-Çakan and Dr. Selin Sarıyer (Gebze Technical University), Prof. Günther Zeck and Dr. Andrea Corna (Technische Universität Wien), as well as Dr. Serge Picaud, Dr. Antoine Chaffiol, and Corentin Joffrois (Institut de la Vision, Sorbonne University). Their expertise, insightful discussions, and collaborative efforts have been instrumental in advancing our work. I would also like to express my sincere gratitude to Dr. Hadi Jahangiri and Dr. Barış Yağcı from Koç University Surface Science and Technology Center (KUYTAM), as well as Dr.

Gülcan Çorapçıoğlu from Koç University Nanofabrication and Nanocharacterization Center for Scientific and Technological Advanced Research (n2STAR), for their invaluable support and expert guidance throughout the materials characterization process. Their insights and assistance were instrumental in the successful completion of this work. I would like to express my sincere gratitude to the Koç University Research Center for Translational Medicine (KUTTAM) for providing access to their exceptional services and facilities. This work was made possible through the generous support of the Republic of Turkey Ministry of Development, and I sincerely appreciate their commitment to advancing research.

I would like to express my sincere gratitude to the Scientific and Technological Research Council of Turkey (TÜBİTAK) for their generous support through Project Nos. 121C310, 121E376, and 124E646, as well as to the European Union (ERC, MESHOPTO, 101045289) for their funding. It is important to note that the views and opinions presented in this work are solely those of the author(s) and do not necessarily reflect the official positions of the European Union or the European Research Council Executive Agency.

I would like to express my deepest gratitude to all my current and former colleagues and friends at the Innovative DEvices and InterfAces LABoratory (IDEALAB) for their unwavering support, stimulating discussions, and invaluable fellowship throughout my research journey. Their contributions have been instrumental in shaping this work. I am particularly grateful to Dr. Güncem Özgün Eren, Dr. Onuralp Karatüm, Lokman Kaya, Rıdvan Balamur, Dr. Hümeyra Nur Kaleli, Dr. Asım Önal, Ömer Faruk Özelci, Saad Ullah Khan, Muhammad Hassnain, Uğur Berkay Çalışkan, Parsa Kaviani, Gizem Yıldız, Eren Tekinay, Melike Öztopal, Gülsu Kahraman, and Alp Yılmaz for their encouragement and collaboration. I also extend my sincere appreciation to the Metin Research Group, especially Dr. Buse Sündü, Dr. Zafer Eroğlu, Dr. Melek Şermin Özer, and Aleyna Başak, for their kindness

and support. Although we may not have collaborated on the same project, their encouragement has been a constant source of my motivation. Through countless discussions, shared challenges, and moments of insight, my colleagues have not only made this journey intellectually enriching but also deeply rewarding on a personal level. Their friendship, laughter, and solidarity during difficult times have made this experience truly memorable.

I would like to express my deepest gratitude to Prof. Önder Metin, whose guidance and support marked the beginning of my academic journey at Koç University. It is thanks to his encouragement that I had the privilege of meeting my esteemed advisor, Prof. Sedat Nizamoğlu, as well as the many wonderful colleagues and mentors who have enriched my experience here. His belief in my potential allowed me to grow beyond my expectations, shaping me into more than just an engineer. For this, I will always remain profoundly grateful, and he will forever hold a special place in my life.

I would like to express my deepest gratitude to my longtime friends, Tuğser Yılmaz and Fatih Uçar, with whom I had the privilege of graduating from Istanbul Technical University. The countless hours we spent studying together, the sleepless nights we endured, and the shared dreams of our futures have left an indelible mark on my academic journey. I am truly fortunate to have such enduring friendships, and I take great pride in the remarkable individuals they have become. Thank you both for your unwavering camaraderie and support over the years.

I would also like to express my deepest gratitude to my beloved girlfriend, Sevgi, for her unwavering love, endless patience, understanding, and steadfast support throughout this journey. Her presence in my life has been a constant source of strength and happiness, and I am truly grateful for her.

Finally, and most importantly, I would like to express my deepest gratitude to my beloved family, my father, Recep Kaya; my mother, Meryem Kaya; and my sister, Melisa Kaya. They have been my greatest source of motivation and the driving force behind this journey. Their unwavering support and encouragement have given me the strength to overcome every challenge along the way.

A special dedication goes to my dearest mother, Meryem Kaya, my greatest inspiration. She has been my steadfast supporter, lifting me up in moments of difficulty and celebrating my achievements with boundless joy. I am endlessly grateful for the love and blessings of my family. With them by my side, I believe no goal is beyond reach.

TABLE OF CONTENTS

LIST OF TABLES

LIST OF FIGURES

ABBREVIATIONS

aCSF	Artificial cerebrospinal fluid
TMS	Bis(trimethylsilyl)sulfide
CSCc	Cathodic charge storage capacity
CTG	CellTiter-Glo
CBD	Chemical bath deposition
CE	Counter electrode
CV	Cyclic voltammogram
H_2DFCDA	2',7'-dichlorodihydrofluorescein diacetate
EIS	Electrochemical impedance spectroscopy
ETL	Electron transfer layer
FDTD	Finite-difference time-domain
FTIR	Fourier transform infrared spectroscopy
HMS	Hexamethyldisilathiane
HTL	Hole transfer layer
HEPES	4-(2 hydroxyethyl)-1-piperazineethanesulfonic acid
ITO	Indium tin oxide
INL	Inner nuclear layer
LDH	Lactate dehydrogenase
MP	Maximum permissible radiant power
MEA	Microelectrode array
MMP	Mitochondrial membrane potential
NC	Nanocrystal
NW	Nanowire

NIR	Near-infrared
NBM	Neurobasal medium
ODE	Octadecene
OD	Optical density
PBS	Phosphate buffered saline
P3HT	Poly(3-hexylthiophene)
PLL	Poly-L-Lsysine
QD	Quantum dot
ROS	Reactive oxygen species
RE	Reference electrode
RGC	Retinal ganglion cells
RuO_2	Ruthenium oxide
SEM	Scanning electron microscopy
SDF	Spike density function
SPEIS	Staircase potentio electrochemical impedance spectroscopy
TMAI	Tetra-methyl-ammonium iodide
TEM	Transmission electron microscopy
WE	Working electrode
XRD	X-ray diffraction
XPS	X-ray photoelectron spectroscopy
ZnO	Zinc oxide

Chapter 1

INTRODUCTION

Today, we face many nervous system conditions, including alzheimer's disease, epilepsy, parkinson's disease, and paralysis. These neurological diseases are the number one cause of ill-health and the number two cause of disability-adjusted life years (DALYs) [Feigin et al., 2019, Vázquez-Guardado et al., 2020], affecting approximately 3.4 billion people (43% of the global population) in 2021. Over the past three decades, the number of cases of these disorders has increased by 18%. Therefore, bioelectronic medicine, an innovative field, which employs electrical impulses to treat diseases, has gained increasing attention as a promising therapeutic approach for complex neurological conditions [Arnold, 2018].

The modern era of bioelectronic medicine began in 1958 with the first fully implanted pacemaker. Today, over 4 million individuals worldwide rely on cardiac pacemakers. Following this breakthrough, the first cochlear implant, which was designed to aid individuals with profound hearing loss in 1961. Since then, more than 120,000 individuals globally have regained auditory function through cochlear implants. Later, advancements shifted toward neurostimulation with the approval of deep brain stimulation (DBS) in 2002 for treating neurological disorders such as Parkinson's disease. By 2013, DBS had been implanted in approximately 40,000 patients.

Retinal prostheses are currently under development as a potential solution for vision restoration. Among the conditions driving the need for such innovations is retinal degeneration, which is particularly age-related macular degeneration (AMD)

and genetic retinitis pigmentosa (RP), both primary causes of severe vision impairment [Cen and Ng, 2018]. These diseases affect hundreds of millions worldwide, and their prevalence continues to rise due to aging populations. In retinal degenerative disorders, photoreceptors, which is the specialized cells that convert light into neural signals, progressively deteriorate and lose function. However, a key therapeutic opportunity arises from the fact that the remaining retinal neural circuitry often remains intact. This preservation suggests that targeted stimulation of these surviving pathways could potentially restore visual perception. To date, Alpha (AMS and IMS) and Argus (I and II) retinal implants have been tested on over a hundreds of patients. The Alpha subretinal prosthesis incorporates silicon photodiodes that transform ambient light into electrical impulses. Clinical results demonstrate that these implants enable users to recognize objects, detect light, and perform mobility tasks [Bloch et al., 2019]. Since the generated output remains insufficient to effectively stimulate retinal neurons, the Alpha implants require a wired power source, leading to prolonged surgical procedures and raising additional concerns regarding invasiveness. Additionally, both the Alpha IMS and Argus II retinal implant systems have been ceased. At present, there are no established clinical treatments available to prevent or reverse these conditions once they manifest.

Bioelectronic interfaces represent a cutting-edge platform for precise neural modulation across from cellular to organ levels. By converting light energy into ionic currents, these systems hold significant potential for clinical applications in nervous system control, thereby exhibiting high promise in delivering artificial vision to individuals affected by retinal degenerative diseases [Vagni et al., 2022, Parameswaran et al., 2018]. The charge injection performance, which is a critical factor in neural stimulation, can be enhanced by integrating additional supercapacitor materials, such as PEDOT, TiN, and IrOx, as a separate layer on nanoassemblies at the electrode-electrolyte interface. Here, our first study presents a novel bioelectronic architecture utilizing $AgBiS_2$ quantum dots (QDs) as a multifunctional component, serving simultaneously as a hole transport medium, a photoabsorbing nanomaterial, and an electrode–electrolyte interface with pseudocapacitive properties, which ex-

hibit a dual charge storage mechanism, supported by both capacitive and diffusion-controlled processes, as evidenced by the power-law behavior of the cathodic and anodic peaks. Furthermore, the device enables photostimulation of hippocampal neurons without generating substantial oxidative stress. This work presents an innovative and high-performance bioelectronic device utilizing pseudocapacitive optoelectronic quantum dots.

Expanding upon this groundwork, our subsequent research presents a biocompatible optoelectronic platform composed of ZnO NW / $AgBiS_2$ QD-based photovoltaic nanoassembly integrated with RuO_2, engineered to operate under near-infrared (NIR) illumination. This combination was carefully constructed using a layer-by-layer deposition technique, resulting in the creation of a precisely controlled and well-defined interdigitated active layer. The performance of the nanoassembly was investigated with respect to varying lengths of ZnO NWs and different thicknesses of the $AgBiS_2$ QD layer. To assess translational potential, ex-vivo experiments were conducted on retinal explants from a blind rat model of photoreceptor degeneration. Overall, our work introduces a promising approach for wireless neural interfaces with applications in vision restoration, neuroprosthetics, and future developments in bioelectronic medicine.

In our third study, we explore NIR-sensitive nanowire and quantum dot-based tandem photodiodes. To overcome the limitations of single-cell devices, which exhibited strong capacitive photocurrents but limited open-circuit voltage (Voc), we developed a tandem photodiode architecture with an optically transparent gold interlayer. This ZnO NW/$AgBiS_2$ QD-based tandem device achieved over a two-fold increase in V_{oc} under NIR illumination while enhancing charge injection in artificial cerebrospinal fluid, demonstrating its potential for efficient neural stimulation.

In summary, this thesis advances the development of bioelectronic interfaces for precise neural modulation by introducing innovative optoelectronic architectures based on quantum dots and nanowires. The first study presents a multifunctional

$AgBiS_2$ quantum dot system that combines photoresponsive, charge storage, and neurostimulatory capabilities, which enables efficient neural activation with minimal oxidative stress. Building upon this principles, in the second study, we present a near-infrared-sensitive ZnO NW / $AgBiS_2$ QD-RuO_2 platform, which was optimized for enhanced charge injection and validated in ex-vivo retinal stimulation, demonstrating its potential for vision restoration. Finally, in the third study, we overcome voltage limitations in single-cell photodiodes by introducing a tandem photodiode design, which significantly improves open-circuit voltage and charge injection performance under NIR illumination. Collectively, these works accomplish a versatile and high-performance framework for next-generation bioelectronic interfaces, with broad implications in neuroprosthetics, artificial vision, and bioelectronic medicine.

Chapter 2

SCIENTIFIC BACKGROUNDS

2.1 Quantum Dot Based Optoelectronic Biointerfaces

2.2 Colloidal Quantum Dots

Quantum dots (QDs), semiconductor nanocrystals, are in the size range of 2-10 nanometers, which present unique properties, including size/shape/composition-dependent wide spectral tunability via quantum confinement effect, relatively high PLQY across the visible and near-infrared (NIR) regions, and excellent solution processability combined with good photo/chemical stability [Brus, 1984, Norris and Bawendi, 1996, Onal et al., 2024]. These advantageous characteristics make them highly valuable for a variety of applications, including optoelectronic devices, such as photodetectors, solar cells, and light-emitting diodes, as well as biomedical uses like bioimaging and photocatalysis [Bernechea et al., 2016]. Additionally, QDs exhibit absorption coefficients significantly higher than those of silicon material, which facilitates the development of flexible and ultrathin optoelectronic devices. Their scalable, low-cost synthesis methods and compatibility with solution-processable fabrication techniques, such as spin-coating and dip-coating, make them suitable for developing economically viable neural implants with broad applicability [Balamur et al., 2024b]. Given these advantages, QDs present a a high potential for next-generation optoelectronic neural interfaces [Han et al., 2022a].

2.3 Optoelectronic Biointerfaces Using Quantum Dots

Neuromodulation studies have utilized QDs such as HgTe and PbS, which are composed of toxic heavy metals. These materials may present risks for long-term applications because of their toxicity. As a safer alternative, researchers have explored

more biocompatible QDs, such as InP and AlSb, for neuronal photostimulation.

HgTe QDs exhibit a strong photoresponse extending into the near-infrared range; however, their Faradaic coupling mechanism with neurons may induce undesirable pH changes in the cellular medium [Pappas et al., 2007]. Alternatively, PbS QDs have shown promise in enabling safe capacitive neural interfacing [Karatum et al., 2022a]. However, the potential degradation of these nanomaterials raises concerns about lead leakage, which poses challenges for their clinical translation. While InP QDs, developed as a substitute for Cd-based nanomaterials, demonstrate advantageous optoelectronic properties and facilitate bidirectional optical voltage control of neurons, they may trigger irreversible Faradaic reactions [Karatum et al., 2021]. In contrast, AlSb QDs facilitate neural stimulation through double-layer capacitive charging and discharging, which do no induce redox reactions [Han et al., 2021]. This mechanism provides highly controlled, biocompatible, and reversible neurostimulation. However, double-layer capacitance permits only transient charge injection during light onset/offset due to rapid photovoltage changes, restricting achievable charge injection levels. Alternatively, $AgBiS_2$ QDs, which is presented in this thesis [Balamur et al., 2025], enable reversible Faradaic reactions, enhancing charge injection while maintaining safety and efficacy. Their combination of high charge injection capacity and broad photoabsorption (visible to near-infrared) renders $AgBiS_2$-based biointerfaces particularly suitable for neural stimulation and deep-tissue applications.

Chapter 3

BIOINTERFACING WITH $AGBIS_2$ QUANTUM DOTS FOR PSEUDOCAPACITIVE PHOTOSTIMULATION

This chapter is reproduced (adapted) from the publication "*Biointerfacing with $AgBiS_2$ Quantum Dots for Pseudocapacitive Photostimulation*" R. Balamur, T. S. Kaya, S. Sariyer, H. N. Kaleli, A. Onal, U. B. Caliskan, M. Hasanreisoğlu, R. Demir-Cakan, S. Nizamoglu, Advanced Functional Materials, 2025, 2422083.

3.1 Introduction

Optoelectronic biointerfaces have emerged as an exciting platform for optical control of living systems [Vagni et al., 2022, Parameswaran et al., 2018, Jakešová et al., 2019, Han et al., 2022b]. They have been used in a wide variety of translational medicine applications from cardiac stimulation for heartbeat control to retinal stimulation for artificial vision [Li et al., 2024, Palanker et al., 2022, Muqit et al., 2024]. These devices advantageously enable wireless control of cellular activity via conversion of light to photovoltage [Lee et al., 2022], which induces anionic photocurrent between the stimulation and return electrodes. So far, various silicon and organic photodiodes have been used for light-to-current conversion [Vagni et al., 2022, Parameswaran et al., 2018, Jakešová et al., 2019, Han et al., 2022b, Li et al., 2024, Palanker et al., 2022, Muqit et al., 2024] and supercapacitor materials such as IrOx, TiN, and PEDOT have additionally been integrated into the electrode–electrolyte interface to enhance charge injection [Vagni et al., 2022, Huang et al., 2021, Jakešová et al., 2024].

Quantum dots (QDs), which earned the Nobel Prize in Chemistry in 2023 [Liz-Marzán et al., 2023], offer advantageous properties for neural interfaces, such as

tunable energy levels via the quantum confinement effect [Norris and Bawendi, 1996, Liao et al., 2023, Anoshkin et al., 2024, De Bastiani et al., 2021], neurological signal sensing [Marshall and Schnitzer, 2013], high stability [Kim et al., 2020, Flatae et al., 2019], targeted delivery [Matea et al., 2017], and wavefunction engineering [Demir et al., 2011, Diroll et al., 2023]. Recently, QDs have demonstrated their applicability for optoelectronic biointerfaces [Han et al., 2022a]. For instance, QDs have been integrated into photovoltaic devices designed for neuronal stimulation. In these devices, QDs act as photoabsorbers, converting light into electron–hole pairs and transferring them at the electrode–electrolyte interface for cell stimulation. However, toxic heavy-metal-based QDs, such as HgTe [Pappas et al., 2007] and PbS [Karatum et al., 2022a], may pose risks for long-term use due to their potential toxicity and generation of harmful byproducts, such as the release of mercury and lead ions.

Alternatively, a safer and more biocompatible alternative is the toxic-heavy-metal-free QDs. InP QDs, which emerged as a replacement for CdSe with favorable properties [Jalali et al., 2022], showed bidirectional optical voltage control of neurons [Karatum et al., 2021], but they may induce irreversible Faradaic reactions (Figure 3.1, left) [Sun et al., 2023]. In contrast, AlSb QDs can induce the charging and discharging of double-layer capacitance without involving redox reactions (Figure 3.1, middle) [Han et al., 2021]. Double-layer capacitor-based neural stimulation offers a highly controlled, reversible, and biocompatible method for neurostimulation. However, double-layer capacitance only allows transient charge injection during the onset and offset of light when there is a sudden photovoltage change, which limits the charge injection level. Alternatively, reversible Faradaic reactions can enhance the charge injection level via a safe and effective approach for neurostimulation. According to our best knowledge, cell-interfacing QDs that utilize light-induced reversible Faradaic processes have not been reported yet, where controlled redox reactions could provide enhanced light-mediated photostimulation (Figure 3.1, right).

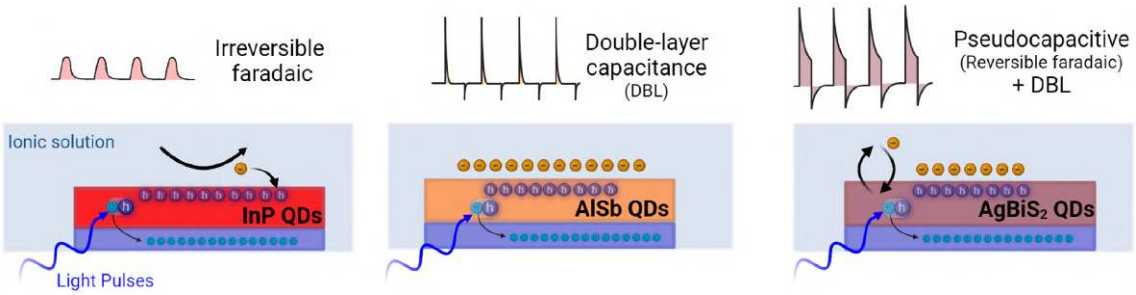

Figure 3.1: **Schematic of photovoltaic devices using quantum dots for biointerfacing (bottom). Their typical photocurrent profile under light pulses is shown (top).** These devices can generate photocurrent through irreversible Faradaic processes (left), double-layer capacitive processes (middle), and pseudocapacitive charge transfer processes (right).

Here, we present a novel bioelectronic interface using $AgBiS_2$ QDs, which simultaneously mediate light absorption, hole transport, and pseudocapacitive interaction at the electrode–electrolyte interface. The power-law relationship observed in the anodic and cathodic peaks indicates a combined contribution of both diffusion-controlled and capacitive processes, which enhances charge storage and interaction with the biological medium. Furthermore, electrochemical analysis of $AgBiS_2$ QD electrodes inartificial cerebrospinal fluid (aCSF) revealed a high capacitance of 3.3 mF cm^{-2}.

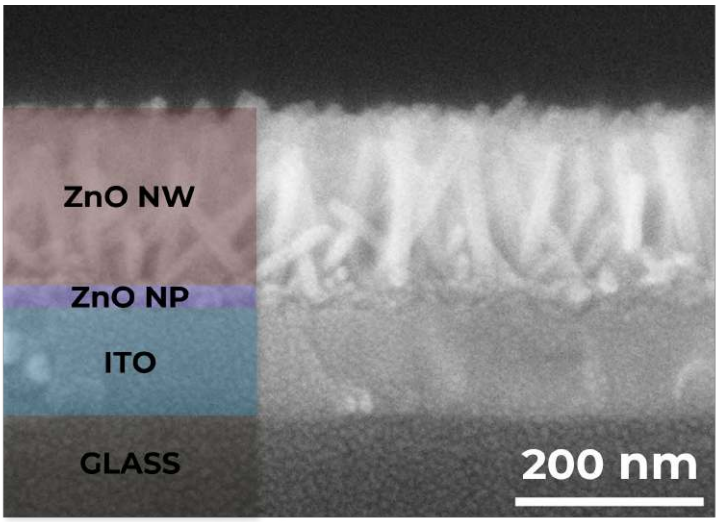

Figure 3.2: **Characterization of ZnO NWs.** Cross-sectional SEM image of ZnO NWs on ITO substrate.

For efficient conversion of light to photocurrent, $AgBiS_2$ QDs are embedded on ZnO nanowires (NWs) within a photovoltaic device architecture (Figure 3.2). The device showed good biocompatibility, and light pulses triggered photostimulation of neurons. The combination of reversible charge storage dynamics and robust photocapacitive behavior positions QDs as an exciting candidate for next-generation bioelectronic devices.

3.2 Methods

3.2.1 Synthesis of $AgBiS_2$ Quantum Dots

$AgBiS_2$ QDs were synthesized by following previously reported low-temperature hot-injection methods using standard Schlenk techniques with small modifications [Bernechea et al., 2016]. All chemicals were purchased from Sigma–Aldrich. In brief, 6.4 mmol silver (I) acetate and 8 mmol bismuth (III) acetate were pumped with argon with 136 mmol oleic acid and 35 mL 1-octadecene (ODE) with raising the temperature. After reaching 100 °C, the reaction vessel was maintained in a vacuum environment for 1 h to generate silver and bismuth oleates. 8 mmol bis(trimethylsilyl)sulfide (TMS) solution diluted in 5 mL ODE was swiftly injected into the reaction vessel after switching the reaction atmosphere to Ar. The color of the solution was immediately changed to dark brown, which means the formation of $AgBiS_2$ QDs. To conduct the purification process, the reaction flask was cooled down in a water bath and the crude solution was precipitated with acetone using a centrifuge at 4500 rpm for 5 min. Sediments were collected and re-precipitated with toluene and acetone and this purification cycle was repeated two times. The resulting $AgBiS_2$ QDs were finally dispersed in toluene with a concentration of 20 mg ml^{-1} to fabricate the bioelectronic interfaces.

3.2.2 Characterization of $AgBiS_2$ Quantum Dots

Solution UV-visible (UV-Vis) absorption measurement was carried out with a Cary 5000 spectroscopy. The XRD measurements were conducted by a Rigaku SmartLab powder diffractometer using Cu Kα radiation with the Bragg–Brentano geome-

try. TEM measurements were performed in the Scientific and Technological Centers of the University of Barcelona (CCiT-UB). TEM micrograph was measured by a JEOL2100 microscope operating at an accelerating voltage of 200 kV.

3.2.3 Synthesis of ZnO NWs

ZnO NWs were synthesized via chemical bath deposition (CBD) on indium tin oxide (ITO) substrates. A 30 nm-thick ZnO seed layer was initially spin-coated onto the ITO. ZnO NWs were then grown by immersing the ITO/ZnO seed layer in a solution containing deionized water, hexamethylenetetramine (0.025 mol L^{-1}), $NH_3 \cdot H_2O$ (0.7 mol L^{-1}), polyethyleneimine (0.06 mol L^{-1}), and zinc nitrate hexahydrate (0.05 mol L^{-1}). The ZnO NWs were grown on the seed layer through a chemical reaction within the solution at 90 °C for 25 min.

3.2.4 Fabrication of ZnO NW-Based Biointerface

Photoelectrodes were fabricated onto the glass substrates covered with indium tin oxide (ITO) (Ossila, S111). The substrate cleaning procedure consists of sonication in NaOH solution for 5 min, in tension-active agent mixed with deionized water solution (HELLMANEX II, 3%) for 15 min, in deionized water for 15 min, in pure acetone for 5 min, and finally in isopropyl alcohol for 5 min all at 55 °C. Subsequent to the cleaning procedure, the substrates were dried in an oven at 40 °C for 45 min. The cleaned substrates were treated with UV–ozone for 20 min to eliminate any other possible residues on the ITO surface.

First, a sol–gel precursor solution of ZnO was prepared. Zinc acetate dihydrate ($Zn(CH_3CO_2)_2 \cdot 2H_2O$) (219.4 mg) was dissolved in 2-methoxyethanol ($C_3H_5O_2$) (2 mL), followed by the addition of ethanolamine ($HOCH_2CH_2NH_2$) (75 mg). The resulting mixture was stirred for 3 min and subsequently subjected to sonication for 30 min at 50 °C. Finally, the ZnO solution was filtered through a 0.22 µm polyvinylidene fluoride (PVDF) membrane. For the ZnO NW/$AgBiS_2$ QD biointerface fabrication, a ZnO precursor sol–gel solution was spin-coated onto ITO substrates at 2000 rpm

for 60 s. Subsequent annealing at 275 °C for 15 min yielded a ZnO seed layer. Chemical bath deposition (CBD) was then employed to synthesize ZnO NWs with a mean length of 180 ± 20 nm on an ITO/ZnO seed layer by immersing the substrate in a ZnO NW solution at 90 °C for 25 min, then an annealing process was conducted at 200 °C for 20 min.

Subsequently, $AgBiS_2$ QDs were incorporated into ZnO NWs via a layer-by-layer dip-coating deposition method. This technique, executed using a dip coating machine, permitted precise control over the interdigitated nanocrystal layer thickness. Infiltration of QDs into ZnO NWs was achieved by introducing a toluene solution containing $AgBiS_2$ QDs (20 g L^{-1}). To enhance the electronic properties of the QDs, the insulating oleate ligands were substituted with iodide ions through the introduction of a tetra-methyl-ammonium iodide (TMAI)-methanol solution (1 g L^{-1}) and held for 45 s. Then, in order to remove excess oleic acid and TMAI ligands, the substrate was immersed in a methanol solution and subjected to a rinsing process for 30 s. Finally, an annealing process at 110 °C for 10 min was conducted. A 2-cycle dip coating process was employed to fabricate a 204 nm thick QD layer. This resulted in a structure consisting of a NW array with a length of 180 nm, overcoated by a 24 nm thick QD layer.

3.2.5 Chronoamperometry and Chronopotentiometry Measurements

For the electrochemical experiments, an Autolab Potentiostat Galvanostat PG-STAT (Metrohm, Netherlands) was used. The three-electrode configuration utilizes Ag/AgCl (Sat'd KCl) as the reference electrode, platinum wire as the counter electrode, and connection to the photovoltaic biointerface as the working electrode. All measurements were carried out in a modified aCSF medium as the electrolyte solution at room temperature. The device was excited with blue and red LEDs. The optical power was controlled with an optical power meter (Newport 843-R). The data was analyzed using the NOVA software.

3.2.6 Electrode Preparation, Cyclic Voltammetry, and SPEIS Measurements

Initially, the $AgBiS_2$ electrode, conductive carbon (Super P), and binder (PVdF, Poly(vinylidene fluoride)) were ground in a mortar for 15 min. The mass ratio of the active material to Super P is 70:20. After that NMP (n-methyl-2-pyrrolidone) solvent was added to the composition to obtain the desired diluted slurry. Subsequently, the slurry was stirred overnight to acquire the homogeneous dispersion. 10 µL of the solution was sprayed with an airbrush (Timbertech) onto a graphite current collector. Then, the deposited electrode was dried at 80 °C for 2 h. CV (at scan rates of 0.5, 1, 3, 5, 10, and 20 mV s^{-1}) tests of $AgBiS_2$ electrode in a three-electrode cell configuration were carried out in the potential range from -0.3 V to 0.3 V versus Ag/AgCl (3.5 m KCl) in 140 mm NaCl, 2 mm CaCl 2, 3 mm KCl, 1 mm $MgCl_2$ as well as aCSF electrolytes. Pt wire was used as the counter electrode. All electrochemical studies were performed with a Bio-Logic VMP3 potentiostat/galvanostat. The SPEIS (Staircase Potentio Electrochemical Impedance Spectroscopy) measurement was carried out to investigate the electrochemical reaction kinetics of the $AgBiS_2$ electrode. In the SPEIS method, sequential electrochemical impedance measurements were performed in 20 mV intermittent potential steps from -0.3 V to 0.3 V versus Ag/AgCl (3.5 m KCl) over a frequency range from 5 mHz to 100 kHz using an AC amplitude 10 mV. In addition, 10 min as a preconditioning step before collecting impedance data was applied to ensure that the equilibrium state was reached at each step. The 3D bode map was generated considering the low-frequency data extending from 10 mHz to 10 Hz. These maps indicate the relationship between capacitance (denoted as C'), frequency, and potential, as well as the phase angle, frequency, and potential across the XYZ axes.

3.2.7 Preparation of Substrates for Neuron Culture

ITO and fabricated $AgBiS_2$-based nanowire devices were sterilized for cell culture experiments through 70% ethanol rinsing and 30 min UV sterilization. Sterilized materials were placed in culture plates and coated with poly-L-lysine (PLL, Sigma–Aldrich, MO, USA) to enhance cell attachment on the surface. The next day

following PLL coating, materials were washed and left to dry under a laminar flow cell culture hood to perform cell seeding.

3.2.8 Primary Neuron Isolation

All experimental procedures were approved by the Institutional Animal Care and Use Committees of Koç University (No: 2021.HADYEK.022 and 2021.HADYEK.017) according to Directive 2010/63/EU of the European Parliament and of the Council on the Protection of Animals Used for Scientific Purposes. Detail of neuron isolation procedures was described in our previous research [Balamur et al., 2024b].

3.2.9 Live/Death Assay with Calcein AM and PI

Neurons were washed twice with 1X Hanks Balanced Salt Solution, HBSS (Invitrogen Cat. no. 14025–092) and incubated with 2 µm calcein AM working solution (Invitrogen Cat.no. C1430) prepared in HBSS for 30 min at 37 °C in a 5% CO_2 incubator. After incubation, the dye solution was removed and propidium iodide (PI) solution (Abcam Cat no. ab14083) prepared in HBSS 1X was added to cells and incubated for 10 min at room temperature. After incubation, cell swere rinsed with HBSS 1X, and fluorescence signals were observed under a confocal laser scanning microscope (Leica DMI8 SP8, Leica, Wetzlar, Germany).

3.2.10 Intracellular Oxidative Stress Measurement

The intracellular oxidative stress level was measured by cellular ROS assay kit 2′, 7′-dichlorodihydrofluorescein diacetate (H_2DFCDA) (ab113851, Abcam). Primary hippocampal neurons were seeded on the control and device as 500 000 cells per well and cultured until DIV14. As a positive control, neurons grown on the control were subjected to 100 µm H_2O_2 for 30 min. All groups were incubated with 20 µm H_2DFCDA in live cell solution (Invitrogen Cat no A59688DJ) for 45 min before imaging at 37 °C, 5% CO_2.Hoechst (0.6 mg mL^{-1}) was used to stain the nuclear compartment of cells. After incubation, cells were washed and incubated with a live cell solution for 10 min at room temperature to stabilize the signals. All immunofluo-

rescence images were taken in the same light intensity, exposure, and magnification with a confocal laser scanning microscope (DMI8SP8, Leica, Wetzlar, Germany), and mean fluorescence intensity was measured by LASX software. Light exposure was performed with 780 nm LED (Thorlabs M780LP1 LED driven with Thorlabs DC2200 LED Driver), illumination: 5 Hz stimulus frequency, 20 ms pulse-width, 1.5 $mW.mm^{-2}$ optical power density. The florescence intensity of the ITO control was acceptedas %100 in the relative fluorescence intensity comparison.

3.2.11 Mitochondrial Membrane Potential (MMP) Assay

Primary hippocampal neurons were seeded on the control and device as 500 000 cell per well and cultured for 5–7 days. The cells were stained with 1 µm JC-1 dye (T3168, Invitrogen) prepared in live cell solution at 37 °C and incubated for 30 min in the dark. After washing cells, JC-1 signals were observed under a confocal laser scanning microscope (DMI8 SP8, Leica, Wetzlar, Germany). Cells were subjected to 780 nm light for 20 s between 20 and 40 switch 5 Hz stimulus frequency, 20 ms pulse-width, 1.5 $mW.mm^{-2}$ optical power density. The mean florescence intensity of JC-1 red aggregate and JC-1 green monomer was quantified and processed using LASX software (Leica, Germany).

3.2.12 Intracellular Calcium influx

Cells were incubated with 1 µm Fluo-4 AM (F14201, Invitrogen) and an equal volume of Pluronic-127 in the neurobasal medium for 40 min at 37 °C in a 5% CO_2. Then they were washed and incubated with a neurobasal medium for 15 min at room temperature to stabilize the signals. Time-lapse recordings were taken with an inverted live cell fluorescence microscope (Axio Observer Z1, ZEISS, Oberkochen, Germany). After 1 min recording, 780 nm LED illumination was applied for 10 s (Thorlabs M780LP1 LED driven with Thorlabs DC2200 LED Driver) during 180 s recording. Changes in the fluorescence intensity of 11 neuron over time were measured by Zen Blue software. Normalized fluorescence changes were calculated as $\Delta F/F_0$, where F_0 is the baseline intensity.

3.3 Results

3.3.1 Material Synthesis and Characterization

$AgBiS_2$ QDs were synthesized by using a low-temperature hot-injection technique. [29] Briefly, the synthesis process involved the reaction of silver and bismuth oleate with hexamethyldisilathiane (HMS) in 1-octadecene at 100 °C. The powder X-ray diffraction (XRD) angles correspond to the (111), (200), (220), (311), and (222) crystal planes (Figure 3.3a), which affirm the presence of cubic rock-salt $AgBiS_2$ QDs.

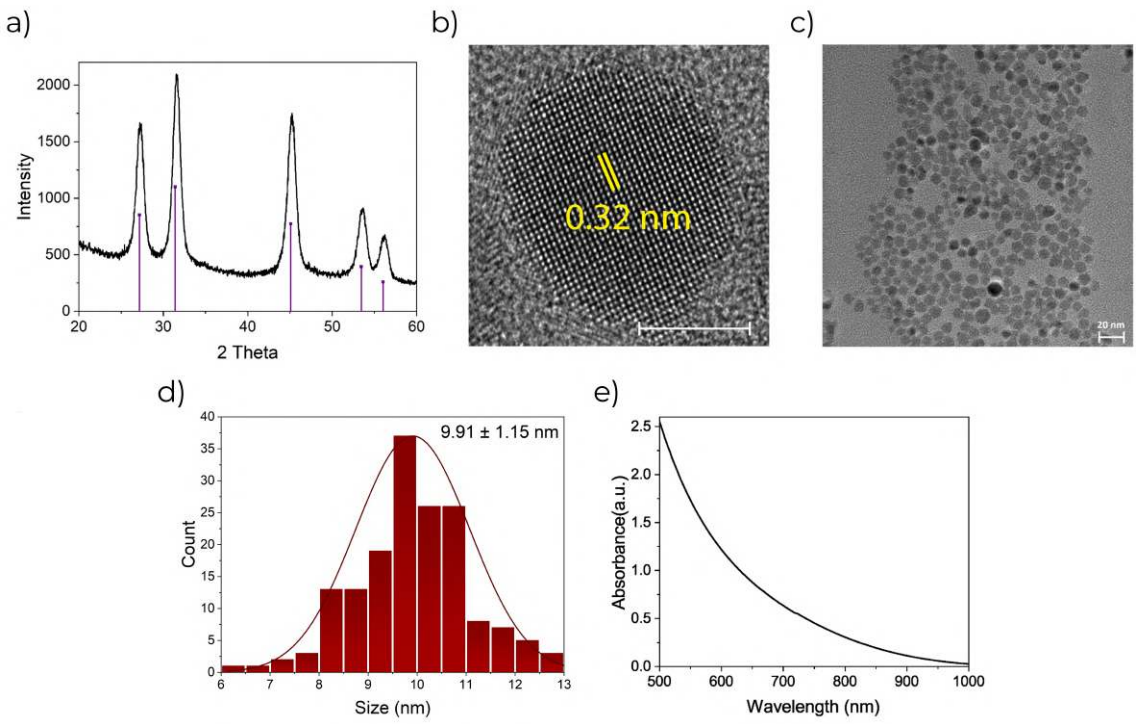

Figure 3.3: **Characterization of $AgBiS_2$ QDs and NW-based devices.** a) XRD of $AgBiS_2$ QDs. b) HRTEM image of $AgBiS_2$ QDs (Scale bar: 5 nm). c) TEM image of the $AgBiS_2$ QDs (Scale bar: 20 nm). d) Size distribution of the $AgBiS_2$ QDs. e) Absorbance of $AgBiS_2$ QDs.

To further analyze the morphology and crystal structure of the $AgBiS_2$ QDs, we conducted a high-resolution TEM (HRTEM) analysis. As illustrated in Figure 3.3b, it reveals a distinct lattice spacing of 0.32 nm, which agrees with the (111) interplanar distances of the $AgBiS_2$ cubic rock-salt lattice structure. The TEM image of the $AgBiS_2$ QDs shows a size distribution of particles with an estimated mean diameter

of approximately 9.91 nm (Figure 3.3c, d). Furthermore, the absorbance reveals the photon absorption up to the band gap in the NIR (Figure 3.3e).

3.3.2 Photo-Electrochemical Performance

We incorporated $AgBiS_2$ QDs as the biointerfacing layer into a photovoltaic device architecture. We characterized the $AgBiS_2$ QDs by performing additional FTIR and XPS measurements. $AgBiS_2$ QDs initially stabilized with insulating oleate ligands and exhibited suboptimal device performance. Therefore, small-chain iodide ions were exchanged with long oleate ligands by introducing tetra-methyl-ammonium iodide (TMAI) to enhance surface passivation and improve the electronic properties of the QDs, facilitating increased charge and photocurrent level. Fourier transform infrared spectroscopy (FTIR) confirmed the removal of oleates, as evidenced by the disappearance of characteristics –CH2- and -CH3- absorption bands (2850–2960 cm^{-1}) of the oleate ligands within the FTIR spectra (Figure 3.4).

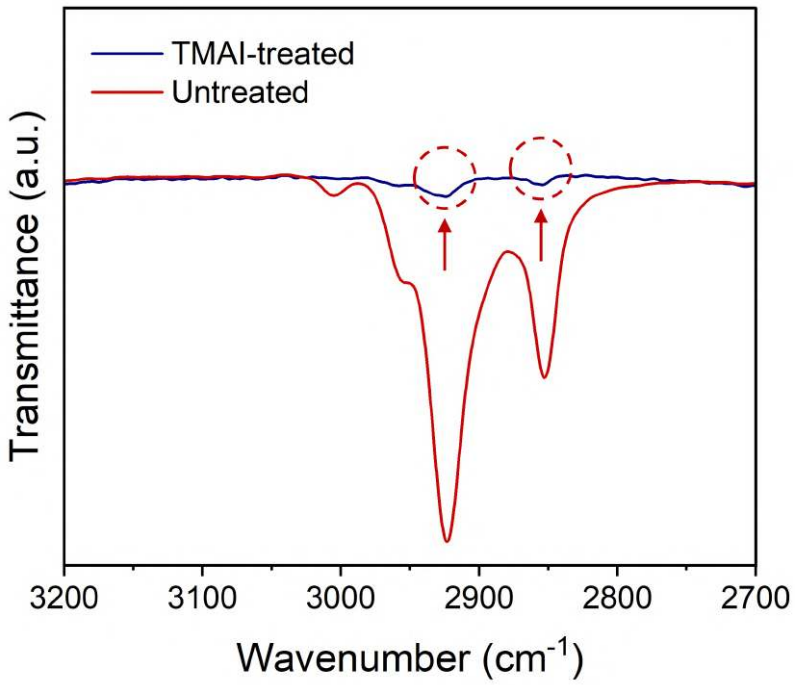

Figure 3.4: **Characterization of $AgBiS_2$ QDs after the ligand exchange process by performing FTIR measurement.** FTIR spectrum of ZnO NW/$AgBiS_2$ QD device before and after the ligand exchange process.

X-ray photoelectron spectroscopy (XPS) analysis further corroborated this ligand exchange process, evident in a shift toward higher binding energies for Ag 3d (367.7 and 373.7 eV) and Bi 4f (159 and 164.3 eV) peaks observed in the XPS spectra (Figure 3.5), indicating effective TMAI treatment and the replacement of oleate ligands with iodide ions.

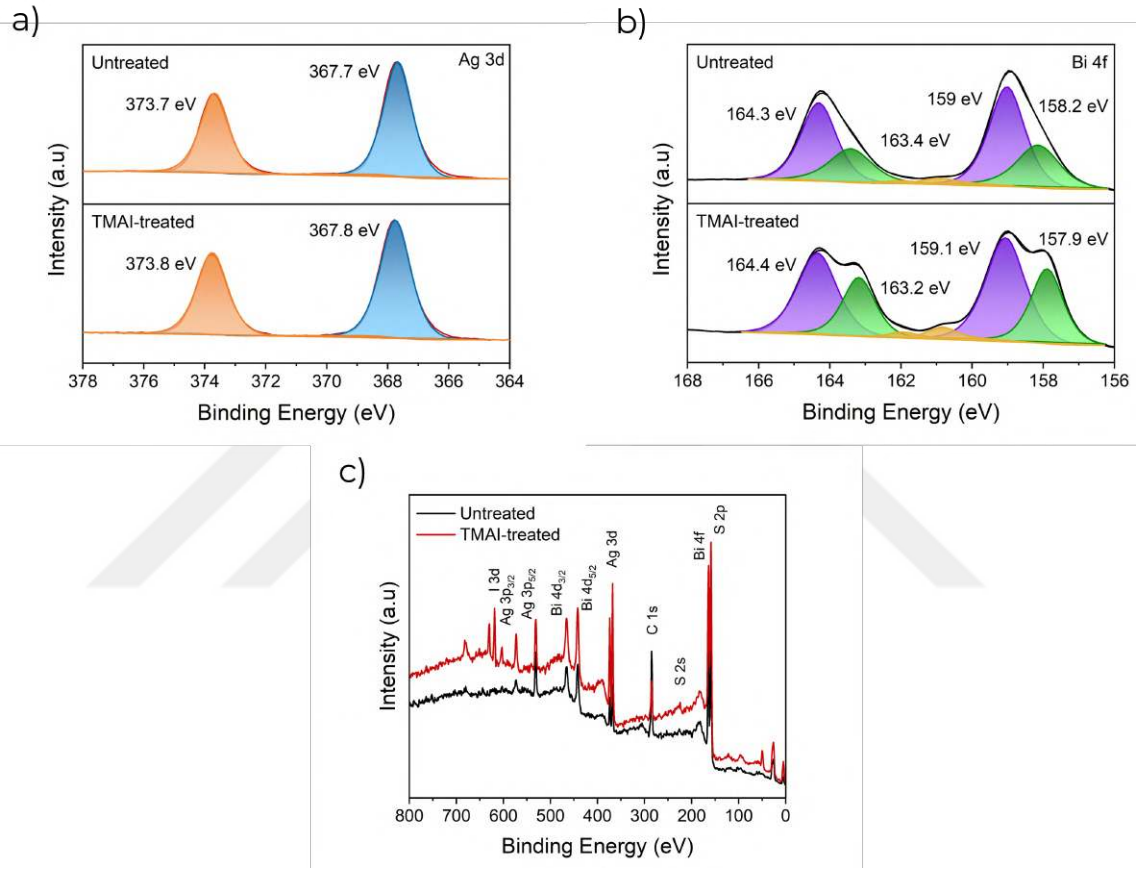

Figure 3.5: **Characterization of $AgBiS_2$ QDs after the ligand exchange process by performing XPS measurement.** XPS spectra of (a) Ag 3d, (b) Bi 4f, and (c) survey spectra of $AgBiS_2$ QDs before and after the ligand exchange process for the ZnO NW/$AgBiS_2$ QD devices.

The device (i.e., NW-QD) consists of a conductive ITO layer, a ZnO seed layer, $AgBiS_2$ QDs infiltrated into the ZnO NW layer, and an $AgBiS_2$ capping layer (Figure 3.6a, b). After photogeneration in the QDs, electron–hole dissociation occurs at the ZnO-$AgBiS_2$ heterojunction (Figure 3.6c). ZnO has a slightly lower conduction band level than $AgBiS_2$, facilitating electron transport to the ITO layer while blocking holes due to its lower valence band level.

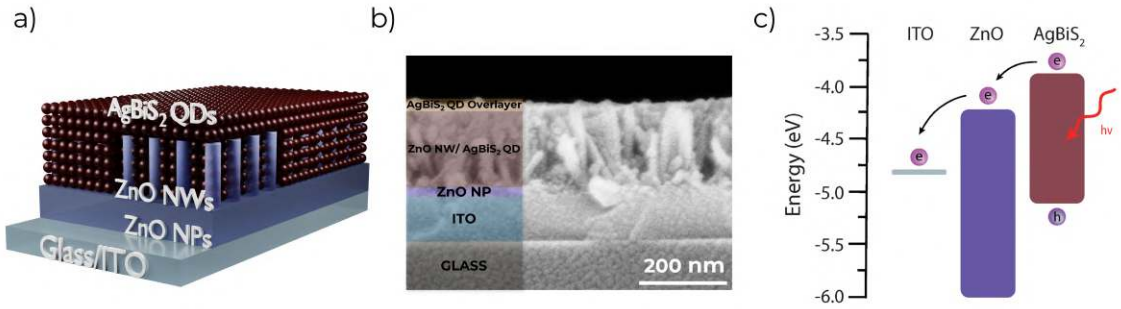

Figure 3.6: **ZnO NW/$AgBiS_2$ QD device structure and operation.** a) Schematic and b) SEM of the pseudocapacitive device structure. c) Energy band diagram of the pseudocapacitive device, and the electron and hole movement under illumination.

Consequently, the holes remain primarily localized in the $AgBiS_2$ QDs enabling hole transport for pseudocapacitive charge transfer at the electrode–electrolyte interface. We measured the photocurrent and photovoltage characteristics using a potentiostat/galvanostat system, where the photovoltaic devices serve as the working electrode, platinum (Pt) as the counter electrode, and Ag/AgCl as the reference electrode (Figure 3.7a).

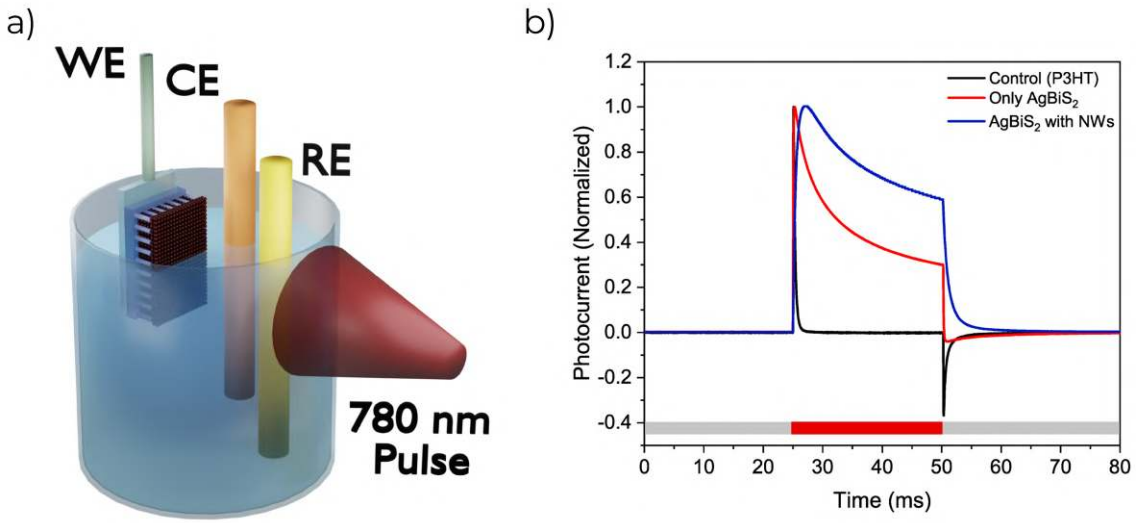

Figure 3.7: **Photo-Electrochemical characterization of the ZnO NW/$AgBiS_2$ QD device.** a) Schematic of electrochemistry setup used for characterization of the photovoltaic device. b) Photocurrent of the control (ITO/ZnO seed/P3HT), devices with ITO/ZnO seed/$AgBiS_2$ and NW-QD under pulsed light illumination. The red line at the bottom indicates when the light is on, while the gray bar represents when the light is off.

We compared NW-QD against two other configurations: a planar device made from P3HT, which serves as the control, and another device with $AgBiS_2$ layer, both of which are on an ITO/ZnO seed layer (Figure 3.7b).

The control group exhibited two spikes during the turn-on and turn-off phases of light exposure. This indicates that the photocurrent is sensitive to the light intensity variation indicating a double-layer assisted photocurrent generation. After replacing P3HT with a planar $AgBiS_2$ QD layer, we observed a noticeable increase in decay time during the period when the light is on, which is indicative of a Faradaic charge transfer mediated photoresponse. Planar devices with an 8 nm-thick QD layer demonstrated the lowest photocurrent performance due to insufficient absorption of incoming light at 780 nm. The champion device, with an $AgBiS_2$ layer thickness of 22 nm, exhibited a peak photocurrent of 0.88 mA cm^{-2} (Figure 3.8) and a charge level of 8.13 ± 0.7 µC cm^{-2} (mean ± SEM, n = 5) under 780 nm irradiation. In planar devices with QD layer thicknesses exceeding 22 nm, although absorption increased, the photocurrent decreased due to the limited carrier diffusion length of $AgBiS_2$ QDs [Xiao et al., 2021].

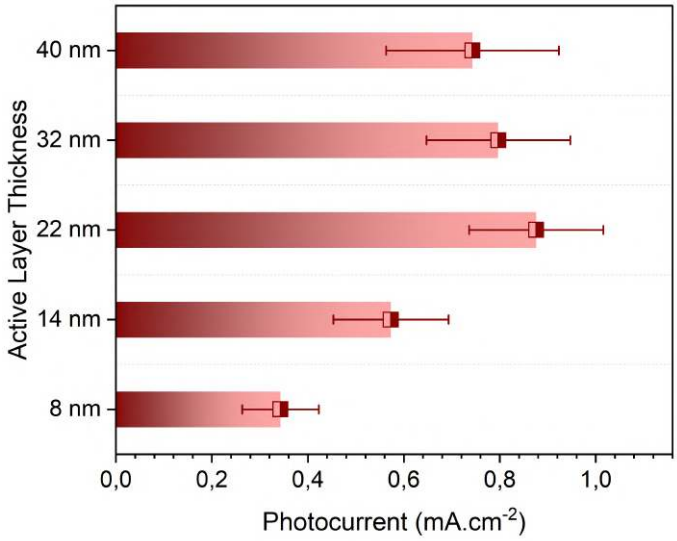

Figure 3.8: **Photocurrent optimization for planar QD-based device.** Optimization of photocurrent for planar QD-based device (without NWs). Photocurrent peak for different $AgBiS_2$ layer thickness under 780 nm NIR light illumination.

To further enhance device performance, $AgBiS_2$ QDs were interdigitated into the ZnO NWs (Figure 3.6b). The NW-QD device showed more than two times higher photocurrent peak (1.9 ± 0.3 mA cm^{-2}) and 3 times higher charge injection (29 ± 2.3 µC cm^{-2}) than the optimized QD-based device without NWs (Figure 3.9 and Table 3.1). The better performance of the NW-based devices arises from several factors. First, the interpenetrating electrodes of ZnO with QDs provide a higher surface area, which facilitates better charge extraction efficiency [Xiao et al., 2021]. Moreover, while the planar morphology of the $AgBiS_2$ layer limits electron diffusion length and effective photogenerated charge dissociation, the interpenetrating electrodes enhance charge collection by reducing the effective distance to the electron transport layer and increasing the heterojunction area between ZnO and QDs. Hence, NWs enable a thicker photoabsorption layer, thereby increasing optical absorption. For instance, while the maximum current in planar morphology was achieved with a thickness of 22 nm (Figure 3.8), the NW device allows the total thickness of the QD layer to increase by nearly an order of magnitude to 204 nm, with a 180 nm NW length and a 24 nm QD overlayer on top of the nanowire array.

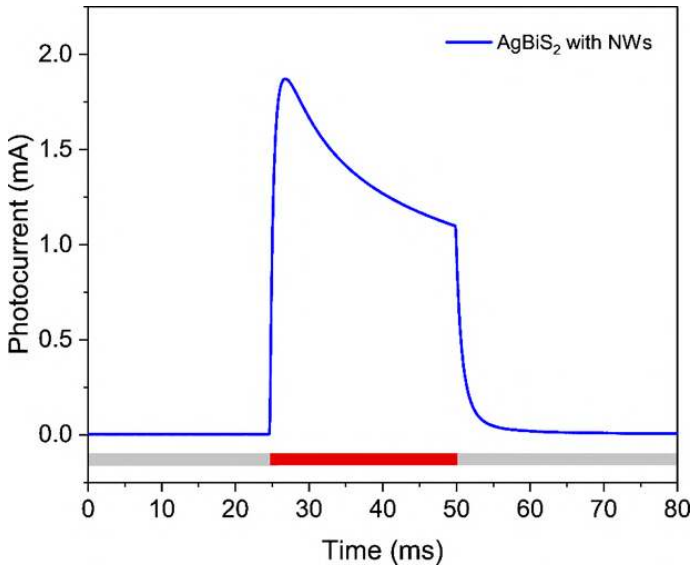

Figure 3.9: **Photocurrent measurement for NW-based device.** Photocurrent of the photovoltaic biointerface with ITO/ZnO-seed/ZnO-NWs/$AgBiS_2$ (Illumination: 25 ms, 780 nm, 58 mW cm^{-2}).

Table 3.1: Electrochemical measurements of different device configurations. The illumination is 25 ms, and 58 mW.cm^{-2}. 450 nm and 780 nm light illumination is used with the same power for P3HT and $AgBiS_2$ devices, respectively (SEM, n=5).

Conductive Layer	**ETL**	**Photoactive Material**	**Photocurrent (mA.cm^{-2})**	**Charge (µC.cm^{-2})**	**Photovoltage (mV)**
ITO	ZnO-seed	P3HT	1.82 ± 0.19	0.6 ± 0.13	220 ± 3.9
ITO	ZnO-seed	$AgBiS_2$	0.88 ± 0.13	11 ± 1.27	167 ± 5.3
ITO	ZnO NWs	$AgBiS_2$	1.9 ± 0.34	29 ± 2.33	197 ± 8.3

As the light intensity increases from 15 mW cm^{-2} to 58 mW cm^{-2}, the total charge injection rises from 5.2 ± 0.8 to 29 ± 2.3 µC cm^{-2} (Figure 3.10a), which is sufficiently high to stimulate a wide variety of tissues in vivo such as retina, sciatic nerve [Cogan, 2008] and even reaches to the defined damage thresholds for deep brain stimulation [Kuncel and Grill, 2004].

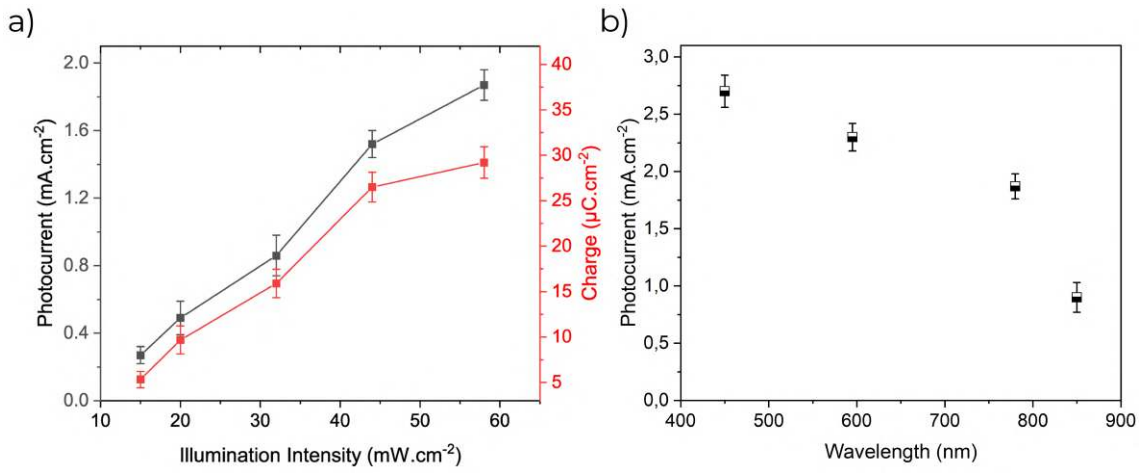

Figure 3.10: **Photocurrent characterization for NW-based device.** c) Charge as a function of illumination intensities under 780 nm light for 20 ms. d) Photocurrent peak levels as a function of illumination wavelengths of 450, 595, 780, and 850 nm.

Figure 3.10b shows that the device generates 1.6 times higher photocurrent under 450-nm blue illumination compared to 780-nm NIR illumination at the same intensity, attributed to the increased absorption of QDs. Moreover, it can also produce a significant amount of photocurrent under 850 nm illumination. To evaluate the operational stability of the ZnO NW/$AgBiS_2$ QD devices in aCSF, we investigated their photostability under repeated illumination cycles. Photocyclic stability assessments demonstrated that the charge injection performance at the biointerface exhibited a consistent level of approximately $55 \pm 5\%$ (mean $\pm$ SEM, n = 5) relative to the initial values throughout 10 000 consecutive illumination cycles (Figure 3.11).

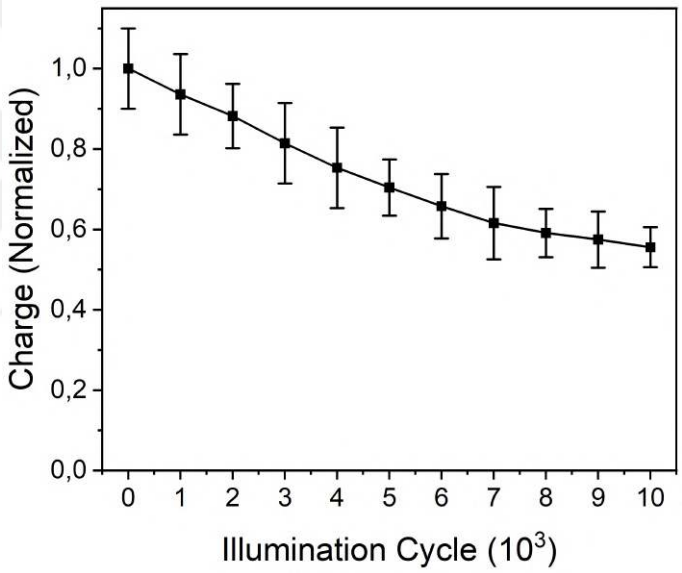

Figure 3.11: **The operational stability of the NW-based device.** The photocyclic stability of the ZnO NW-based biointerfaces, assessed by monitoring the variation in charge injection for 10.000 photo-cycles. Illumination parameters are 780 nm wavelength, 20 ms pulse width, and 58 mW cm^{-2} light intensity.

3.3.3 Electrochemical Characterization of $AgBiS_2$ QDs

We examined the charge-storage effect of ions in the QD-liquid heterojunction. We tested the photoresponse in artificial cerebrospinal fluid (aCSF) to mimic a standard biological environment used in many bioelectronic studies [Castagnola et al., 2015, Balamur et al., 2024a, Sang et al., 2022].

Each salt constituting aCSF such as $CaCl_2$, KCl, and $MgCl_2$ was separately prepared, and their cyclic voltammogram (CV) performances were evaluated to elucidate the main charge compensation species (Figure 3.12). The CV analyses were employed in various aqueous electrolytes at a voltage range from -0.3 to 0.3 V versus Ag/AgCl (3.5 m KCl). Overlapping CV curves for the 10 cycles in aCSF indicate a highly reversible process (Figure 3.12a). The CV measurements of an $AgBiS_2$ electrode in 140 mm NaCl, 2 mm $CaCl_2$, 3 mm KCl, and 1 mm $MgCl_2$ at a scan rate of 10 mV s^{-1} were depicted in Figure 3.12b.

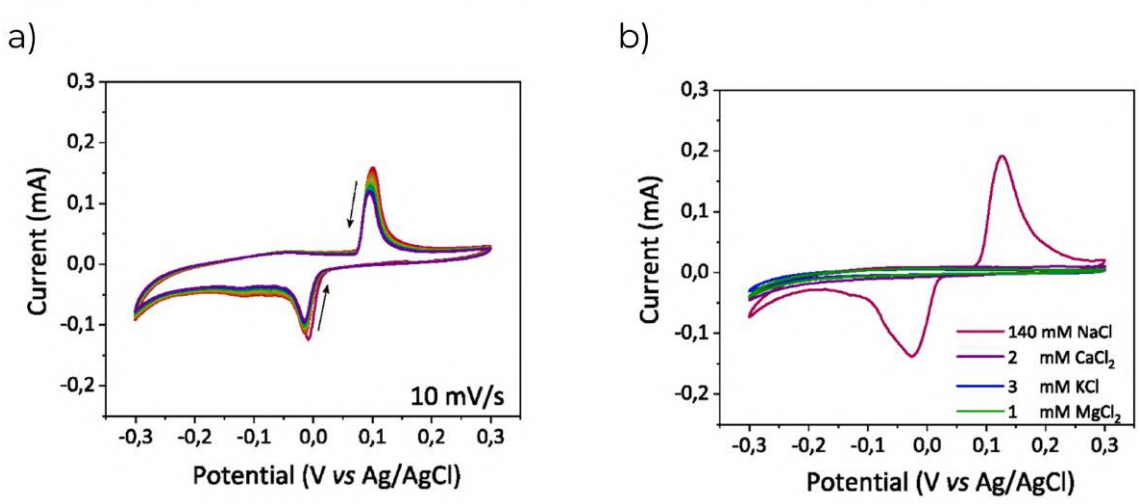

Figure 3.12: **Charge-storage effect of ions s in the QD-liquid heterojunction.** a) CV curves of $AgBiS_2$ electrode in aCSF at scan rate of 10 mV/s. b) CV curves of $AgBiS_2$ electrode in 140 mM NaCl, 2 mM $CaCl_2$, 3 mM KCl and 1 mM $MgCl_2$ electrolyte solutions at scan rate of 10 mV/s.

When the redox behavior of the $AgBiS_2$ electrode is investigated, the dominant reduction peak at -0.03 V and oxidation peak in the vicinity of 0.13 V are observed, especially in the NaCl electrolyte, implying that faradic effects contribute to the electrochemical process. The presence of a faradaic process for the $AgBiS_2$ electrode in a 2 m KOH aqueous electrolyte has been reported [Aman et al., 2023]. Considering the CV performances of other electrolyte salts such as $CaCl_2$, KCl, and $MgCl_2$ (Figure 3.13), it appears that the capacitive behavior of NaCl in aCSF plays a prominent role in the electrochemical performance of $AgBiS_2$.

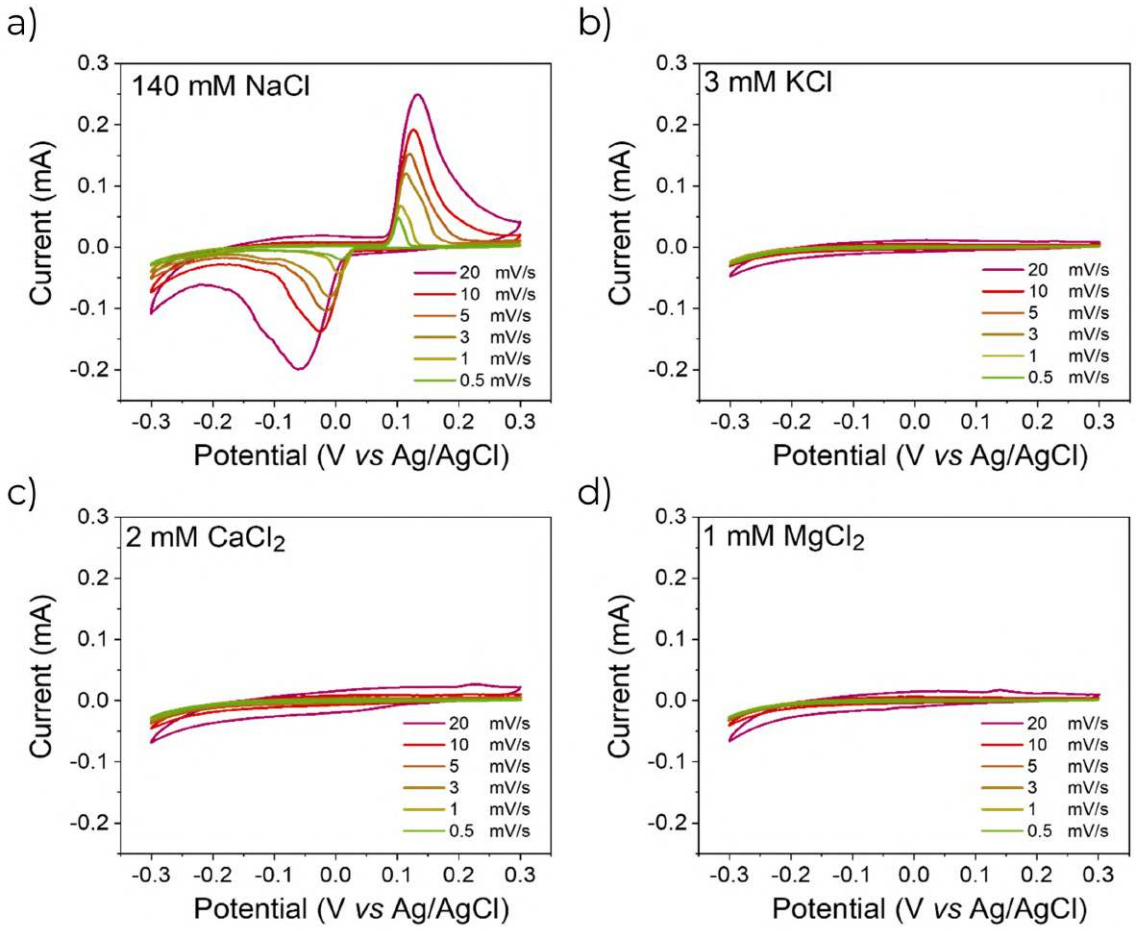

Figure 3.13: **Redox behavior of the $AgBiS_2$ electrode.** CV curves of $AgBiS_2$ at different scan rates in (a) 140 mM NaCl electrolyte. (b) 3 mM KCl (c) 2 mM $CaCl_2$. (d) 1 mM $MgCl_2$.

The CV curves of the $AgBiS_2$ electrode in aCSF obtained at different scan rates from 20 to 0.5 mV s^{-1} are shown in Figure 3a, indicating a reversible redox reaction. In addition, CV curves (Figure 3.13) were obtained at the same scan rates in the other three electrolytes (3 mm KCl, 2 mm $CaCl_2$, and 1 mm $MgCl_2$) (Figure 3.13b-d), clearly showing that there are no significant reduction and oxidation peaks compared to the NaCl electrolyte (Figure 3.13a). As the scan rate increases, the oxidation peak shifts to a more positive potential while the reduction peak shifts to a more negative potential, which stems from the pseudocapacitive nature of the active material (Figure 3.14a).

The existence of such a non-Faradaic process resulting from the formation of a double layer at the electrode–electrolyte interface has also been observed in other studies containing chalcogenide samples [Khan et al., 2019, Ramasamy et al., 2015]. Additionally, an in-depth analysis of the charge storage mechanism of $AgBiS_2$ employed as an anode material for potassium ion batteries has revealed that displacement ($AgBiS_2 + K^+ + e^- \rightarrow KBiS_2 + Ag$), conversion ($KBiS_2 + K^+ + e^- \rightarrow K_2S + Bi$) and alloying ($Bi + K^+ + e^- \rightarrow KBi_2 \rightarrow K_3Bi_2 \rightarrow K_3Bi$) reactions take place [Ren et al., 2020].

To further scrutinize the contribution of diffusion-controlled and surface-controlled processes in the charge transfer mechanism in the aCSF, the CV curves of $AgBiS_2$ electrode at different scan rates ranging from 20 to 0.5 mV s^{-1} were analyzed (Figure 3.14a). According to the CV analysis, the relationship between peak current (i) and scan rate (ν) can be expressed by the following equation [Chang et al., 2022]:

$$i = a\nu^b \tag{1}$$

Herein, the a and b values are adjustable coefficients, and the b value is determined from the slope of the log(i) versus log(ν) plot. Hence, the b value of 0.5 implies that the solid-state diffusion-limiting mode is dominant, while a value of b close to 1 specifies that the surface-controlled process associated with the electric double-layer capacitive response is prominent [Wang et al., 2007]. As seen in Figure 3.14b, the b-values were found as 0.68 for the anodic peak and 0.79 for the cathodic peak, suggesting the contribution of both diffusion-controlled process and capacitive behavior to the charge storage mechanism of $AgBiS_2$. Then, the contribution ratios of both processes were determined with the help of the following expression [Wang et al., 2007]:

$$i = k_1\nu + k_2\nu^{1/2} \tag{2}$$

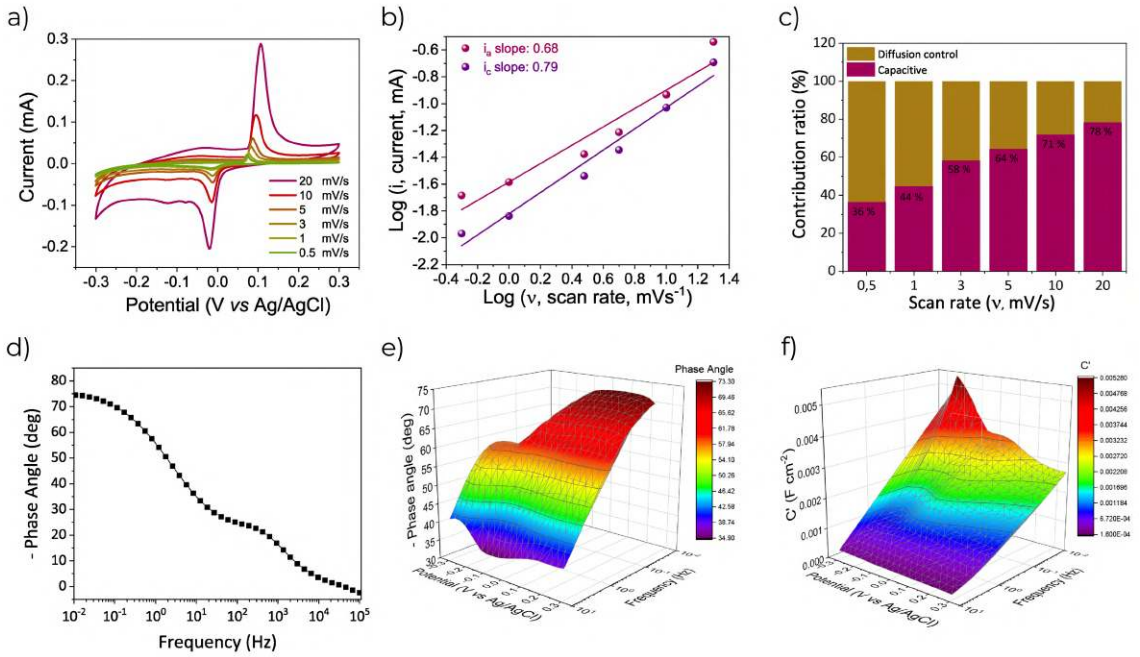

Figure 3.14: **Electrochemical Characterization of $AgBiS_2$ QDs.** a) CV curves of $AgBiS_2$ in aCSF electrolyte at different scan rates. b) Linearized log(i) versus log(ν). c) The contribution of capacitive and diffusion-controlled effects. d) 2D Bode plot, e) 3D Bode plot (phase angle, potential, frequency), f) 3D Bode plot (capacitance, potential, frequency).

In this equation, the first term ($k_1\nu$) is related to surface-controlled capacitive behavior, while the latter term ($k_2\nu^{1/2}$) is concerned with diffusion-controlled impact. As demonstrated in Figure 3.14c, when the sweep rate increases from 0.5 to 20 mV s^{-1}, the contribution of the capacitive process of the $AgBiS_2$ electrode rises from 36% to 78%. In addition, the contribution of the capacitive effect of 64% at a scan rate of 5 mV s^{-1} is shown in the purple shaded area on the CV graph (Figure 3.15). Likewise, analogous CV curves (Figure 3.16a) were obtained for $AgBiS_2$ electrodes in 140 mm NaCl electrolyte.

As seen in Figure 3.16b, the anodic and cathodic b values were obtained as 0.45 and 0.59, respectively. The capacitive ratio increased from 47% to 85% as the scan rate increased (Figure 3.16c). However, a higher capacitive contribution ratio of 73% was found at the same scan rate of 5 mV s^{-1} (Figure 3.16d).

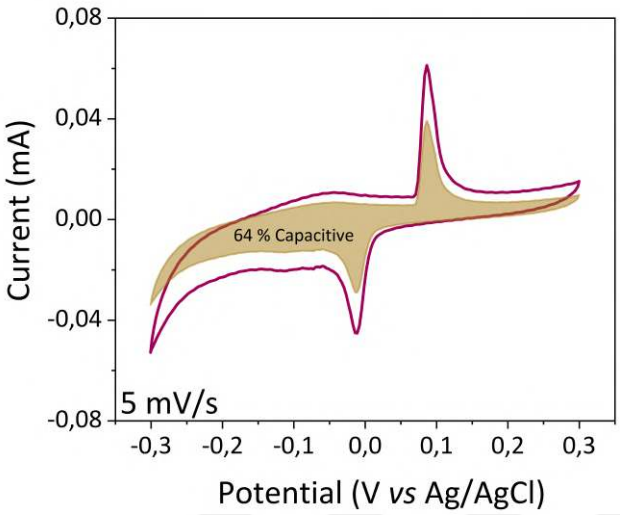

Figure 3.15: **The contribution of the capacitive effect.** CV graph of $AgBiS_2$ at a scan rate of 5 mV/s in aCSF electrolyte.

To further investigate exhaustive charge storage dynamics of $AgBiS_2$ in aCSF electrolyte, 3D Bode plots derived from the increasingly favored SPEIS method were utilized, which provides more comprehensive information about the insight into the storage mechanism than conventional CV analysis [Ko et al., 2018, Patil and Patil, 2023, Sahoo et al., 2023, Tomar et al., 2022]. According to the model suggested by Taberna, Simon, and Fauvarque, the impedance response of carbon-based electrodes includes a simple equivalent circuit composed of a resistor and a capacitor depending on the frequency (10 mHz to 10 Hz) under certain conditions [Taberna et al., 2003]. Based on this model, the real capacitance C' and phase angle (ϕ) can be calculated using the following equations [Taberna et al., 2003].

$$C' = \frac{-Z''}{2\pi f |Z|^2} \tag{3}$$

$$\phi = -\tan^{-1}\left(\frac{Z'(\omega)}{Z''(\omega)}\right) \tag{4}$$

here, Z'', $|Z|$, and Z' represent the impedance of the imaginary component, of the absolute value, of the real part, respectively, and f expresses the angular frequency.

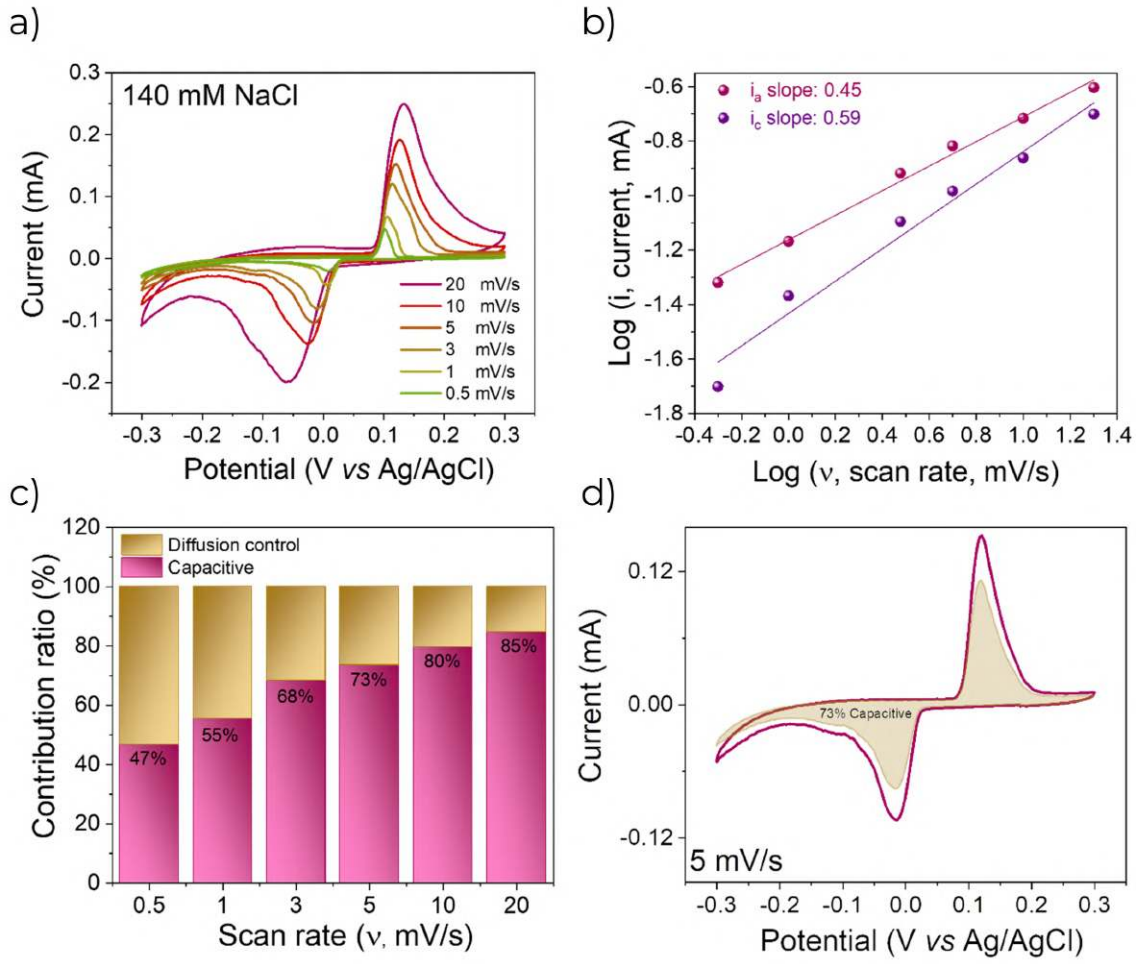

Figure 3.16: **The capacitive contribution of NaCl electrolyte.** (a) CV curves of $AgBiS_2$ in 140 mM NaCl electrolyte at different scan rates. (b) Linearized log(i) vs log(ν). (c) The contribution of capacitive and diffusion-controlled effect. (d) CV graph at a scan rate of 5 mV/s in 140 mM NaCl electrolyte.

Primarily, ϕ versus frequency graph, the traditional 2D Bode plot, was scrutinized at the half-wave potential ($E_{1/2}$) (Figure 3.14d). This term is determined by averaging the anodic and cathodic peak potentials obtained from CV, which was found to be 0.044 V (considering the scan rate of 20 mV s^{-1} in Figure 3.14a). Observing changes in ϕ as a function of frequency provides insights into the rate-limiting kinetics of the electrochemical process of $AgBiS_2$ [Taberna et al., 2003, Ko et al., 2020, Kurra et al., 2021]. When the phase angle equals 0°, the electrochemical process is primarily resistive. On the other hand, if ϕ is 45°, it implies that the rate-limiting step is involved in the electrochemical process.

Ultimately, a phase angle of 90° suggests the domination of capacitive behavior. Considering this information, the $AgBiS_2$ electrode illustrates a phase angle response of −74.4° at a low frequency of 10 mHz, as seen in Figure 3.14d. This phenomenon is attributed to the prevalence of dominant redox processes at low frequencies in aCSF electrolyte, resulting in a comparatively lower phase angle. Moreover, the frequency equivalent to a phase angle of −45° acts as the cross-over point between capacitive and resistive performances. The cross-over frequency is 2.6 Hz, indicating that the resistive component takes precedence after this frequency. Evaluation of impedance data through 3D Bode plots enables a more detailed mapping of the charge-storage dynamics in $AgBiS_2$. In these plots, C' and ϕ are the dependent variables, while the independent variables contain frequency (f) and the cell voltage. As illustrated in Figure 3.14e, there is a noticeable decrease in the phase angle (ϕ) at lower frequencies, mainly associated with surface-confined charge-transfer processes [Ko et al., 2020]. As depicted in Figure 3.14f, $AgBiS_2$ achieved a high areal capacitance (C') within a regime constrained by kinetic limitations, and a capacitance of 3.3 mF cm^{-2} was obtained at $E_{1/2}$ (0.044 V vs Ag/AgCl) [Ko et al., 2020]. From the 3D Bode plots of phase angle and capacitance, it is revealed that $AgBiS_2$ electrode in aCSF electrolyte exhibits the pseudocapacitive behavior.

3.3.4 Biocompatibility and Ca Imaging

Biocompatibility is a critical requirement to interface with biological systems. To assess the safety and compatibility of NW-QD, we conducted biocompatibility tests using primary hippocampal neurons isolated from embryonic rats at days 16–18. Primary neurons were cultured on both the indium tin oxide (ITO) substrate, serving as a control, and on the bioelectronic device (Figure 3.17). Live and dead cell staining assays were performed to evaluate cytotoxic effects under the experimental conditions, revealing similar cell viability between the device and the control group, indicating minimal cytotoxicity, and confirming its biocompatibility.

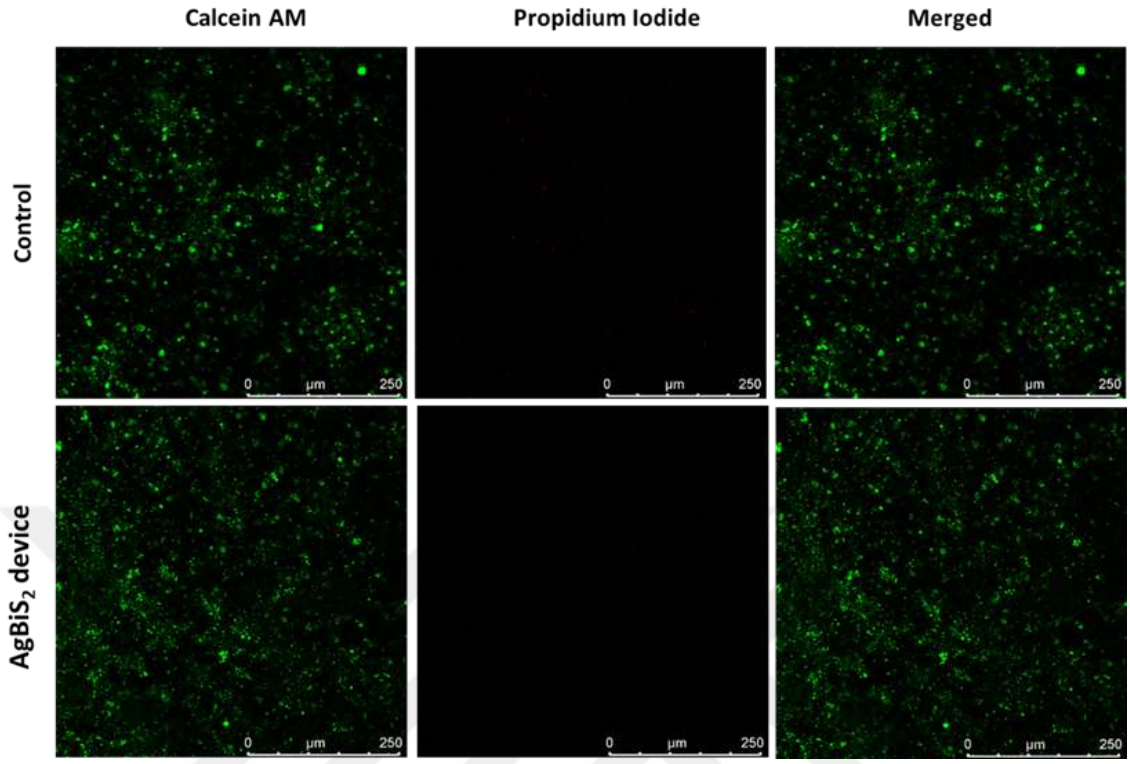

Figure 3.17: **The viability of primary hippocampal neurons cultured on control and $AgBiS_2$ QD based nanowire device.** The cells viability was visualized through live/dead calcein AM/PI double staining assay. Calcein AM in green shows alive cells, while propidium iodide (PI) in red indicates dead cells (Scale bar, 250 µm).

To further explore the safety of the biointerface, we investigated the production of reactive oxygen species (ROS), which is a marker of oxidative stress and can indicate potential cytotoxic effects. Fluorescence intensity of H_2DCFDA, a ROS indicator, was measured before and after light exposure. Neurons grown on ITO served as the negative control, while those exposed to 100 µm H_2O_2 served as the positive control. The results indicated no statistically significant difference in ROS levels between neurons cultured on the bioelectronic device and the control for both before and after illumination (Figure 3,18a, b), confirming that light-stimulated activity on the biointerface does not induce harmful oxidative stress. Another indicator of cellular stress is the changes in mitochondrial membrane potential. Since mitochondria play a dynamic role in cellular homeostasis and enhance axonal networking in neurons by supplying energy to axonal and dendritic ends, maintaining mitochon-

drial membrane potential is crucial for sustaining cellular metabolism. Here, JC-1, a fluorescent indicator of mitochondrial membrane potential, was used to visualize healthy and disrupted organelles after light illumination (Figure 3.18c–e). The ratio of aggregate to monomer signals before and after light illumination indicates the preservation of mitochondrial membrane potential and overall mitochondrial health. This further supports the device's suitability for biointerfacing.

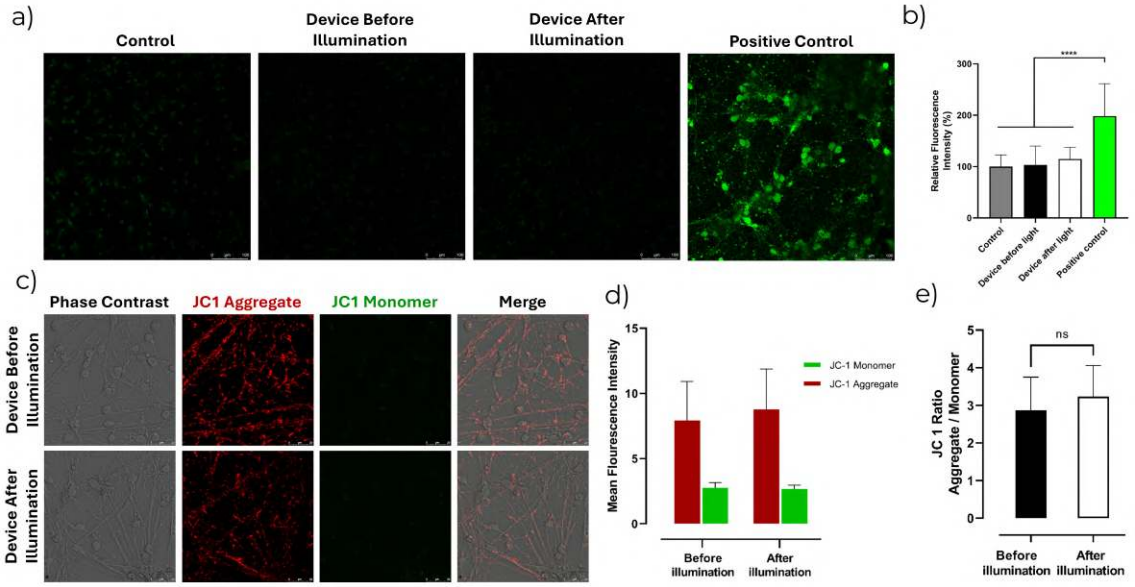

Figure 3.18: **Intracellular oxidative stress assessment.** a) Intracellular fluorescent ROS level of primary neurons cultured on NW-QD device. Cells were illuminated with 780 nm LED with 10 000 cycles, illumination: 5 Hz stimulus frequency, 20 ms pulse-width, 1.5 mW mm^{-2} optical power density. ITO is negative control and ITO with H_2O_2 is positive control (scale bar: 100 µm). b) Measured relative intracellular fluorescence intensities. The fluorescence intensity of negative control is normalized to 100%. Ordinary one-way ANOVA was used to determine the statistical significance of the differences among multiple groups, and *p $<$ 0.05 was evaluated as statistically significant. c) Mitochondrial membrane potential (MMP) assay, JC-1 aggregates (red) refer to healthy mitochondria while JC-1 monomers (green) show disrupted mitochondria. Cells were illuminated with 780 nm LED with 10 000 cycles, illumination: 5 Hz stimulus frequency, 20 ms pulse-width, 1.5 mW mm^{-2} optical power density. d) Mean fluorescence intensity of red and green signals in the device before and after light illumination. e) Ratio of JC-1 aggregates to JC-1 monomer in the device before and after light illumination. The level of significance was calculated using an unpaired, two-tailed t-test; *p $<$ 0.05 was considered statistically significant, and no significant differences were presented as "ns."

To validate photostimulation of neurons, we assessed the light-dependent activation of neuronal cells cultured on the biointerface by performing an intracellular calcium release test. Calcium is a crucial agent in neurons, playing a significant role in action potentials and synaptic transmission by triggering the release of neurotransmitters for signal transduction. When calcium levels rise in the synaptic cleft, it facilitates the release of neurotransmitters from vesicles, enabling synaptic transmission.

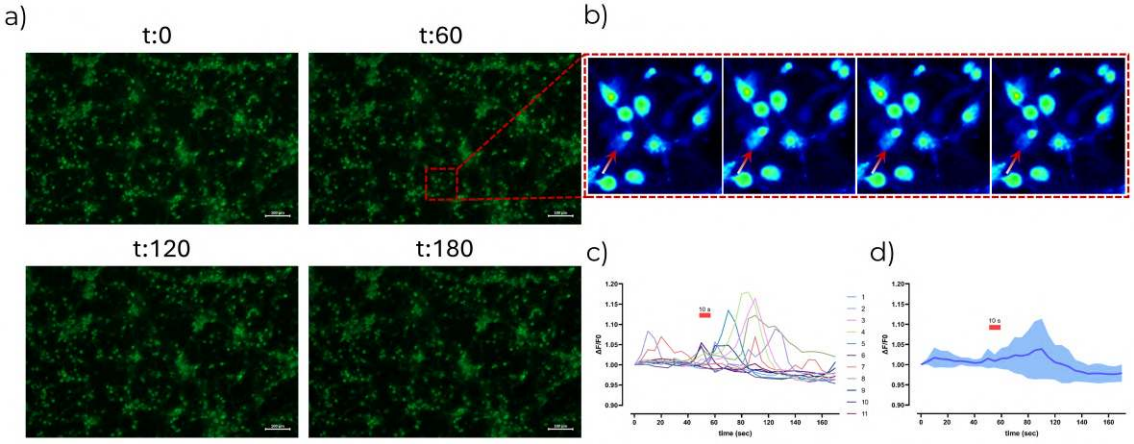

Figure 3.19: **Intracellular Calcium influx.** a) Changes in calcium fluorescence signals before, during, and after light illumination. b) Rainbow representation of calcium release of a single neuron (red arrow) cultured on the device after 780 nm light stimulation with stimulus frequency, 5 Hz; 20 ms pulse-width; light duration, 10 s. The selected area in a, which was shown in the square with dashed red line, was magnified. c) Florescence intensity changes before and after illumination on single neurons. Light stimulation was performed at 60-s for 10 s. d) Mean of relative florescence intensity changes of eleven different neurons on the biointerface.

To observe this release, cells were stained with a calcium indicator of Fluo-4 AM, and calcium levels were recorded for 180 s (Figure 3.19a, b). The light illumination with a stimulus frequency of 5 Hz, a pulse width of 20 ms, a light duration of 10 s, and an intensity of 1.5 mW mm^{-2} were applied during recording. Changes in fluorescence levels were calculated by dividing the fluorescence intensity of each selected cell at a specific time point (ΔF) by the initial fluorescence intensity of cells (F_0). The fluorescence intensities of neurons on the device increased upon light exposure as shown in Figure 3.19c, d. Analysis of eleven randomly selected cells showed an average increase of 5% in calcium fluorescence traces showing photostimulation of neurons (Figure 3.19d).

3.4 Discussion

To enhance the photogenerated ionic charges, a wide variety of photovoltaic devices were integrated with the supercapacitor materials such as RuO_2 [Karatum et al., 2022b], TiN [Vagni et al., 2022], and PEDOT [Han et al., 2020], where the photovoltaic conversion and interfacial charge storage are done by separate materials. Instead, the bioelectronic device presented in this study achieves comparable ionic charge levels without a distinct supercapacitor material. Such simplified devices combined with organic and inorganic microscale LEDs can have high potential for seamless integration into the targeted nerve tissues [Taal et al., 2023, Kim et al., 2013]. Moreover, the photoabsorption spectrum of QDs covers a wide spectral range up to NIR, where the light penetration depth is significantly enhanced due to lower tissue absorption and scattering [Cui et al., 2023]. The demonstration of light-triggered reversible reactions adds an exciting feature to the bioelectronic devices. Hence, the exploration of diverse optoelectronic materials continues to expand the possibilities for unconventional and enhanced bioelectronic applications.

In the 1970s, the pioneering study by Fujishima and Honda demonstrated the potential of TiO_2 semiconductor electrodes to produce H_2 and O_2 through water splitting, which led to the development of the field of photocatalysis [Fujishima and Honda, 1972]. Their work was further extended to applications such as CO_2 reduction, pollutant degradation, NOx conversion, and antibacterial activity [Sun et al., 2023, Nikoloudakis et al., 2022, Mei et al., 2022, Balci Leinen et al., 2018, Courtney et al., 2016]. In typical photocatalytic processes, photogenerated electrons engage in reduction and oxidation reactions, which are generally irreversible. For water photolysis, a wide variety of heavy-metal-free QDs such as InP, $CuInS_2$, $AgInSe_2$, and many others have been used [Jin et al., 2024]. To the best of our knowledge, this study is the first to demonstrate the use of QDs, notably composed of toxic heavy-metal elements, for light-induced reversible Faradaic reactions.

3.5 Conclusion

In conclusion, the integration of toxic-heavy-metal-free $AgBiS_2$ QDs as a biojunction in a photovoltaic device has unveiled a promising avenue for advanced bioelectronic applications. The study shows that the reversible reactions are enabled by diffusion-controlled processes and capacitive behavior in aqueous environments. The ability to produce high charge levels, combined with a broad photoabsorption spectrum from visible to near-infrared, makes these devices highly suitable for neural stimulation and deep tissue applications where light penetration is critical (Table 3.2).

Table 3.2: Photocurrent, charge density, and operational wavelengths from previous studies compared to this study.

References	**Max. reported photocurrent**	**Max. reported charge density**	**Wavelength (nm)**
This Study	2.2 $mA.cm^{-2}$	31.3 $\mu C.cm^{-2}$	780
[Balamur et al., 2024b]	2.3 $mA.cm^{-2}$	11.7 $\mu C.cm^{-2}$	780
[Karatum et al., 2022a]	0.5 $mA.cm^{-2}$	6 $\mu C.cm^{-2}$	780
[Karatum et al., 2022b]	6 $mA.cm^{-2}$	20 $\mu C.cm^{-2}$	450
[Han et al., 2020]	3 $mA.cm^{-2}$	1 $\mu C.cm^{-2}$	445
[Han et al., 2021]	0.6 $mA.cm^{-2}$	0.18 $\mu C.cm^{-2}$	445
[Karatum et al., 2021]	125 $\mu A.cm^{-2}$	1.29 $\mu C.cm^{-2}$	445

Notably, the elimination of the separate transition metal oxides simplifies the device structure, providing a more effective and practical solution for reversible Faradaic reactions. Overall, this work highlights the potential of QDs in advancing the field of bioelectronics, particularly for applications that require safe, efficient, and reversible control over biological processes.

Chapter 4

PHOTOVOLTAIC NANOASSEMBLY OF NANOWIRE ARRAYS SENSITIZED WITH QUANTUM DOTS FOR NEAR-INFRARED RETINA PHOTOSTIMULATION

4.1 Introduction

Nanowires have emerged as a versatile nanomaterial platform for electrophysiology, enabling single-cell recordings [Patolsky et al., 2006], three-dimensional tissue mapping [Liu et al., 2015], and in vivo brain activity monitoring [Fu et al., 2016]. Their unique potential extends to photovoltaic neural stimulation, where they convert light energy into bioelectrical signals to modulate neuronal activity [Shi et al., 2022, Zhang et al., 2021]. This capability stems from their high surface-area-to-volume ratio, which enhances charge separation and collection, while their nanoscale geometry promotes exceptional light-trapping and absorption [Deng et al., 2019]. Such properties enable ultra-efficient photovoltaic operation, even at the single-nanowire level [Krogstrup et al., 2013].

Current silicon nanowires (single or arrays) [Parameswaran et al., 2018, Parameswaran et al., 2019] and TiO_2 nanowire arrays [Ronzani et al., 2018] have demonstrated the ability to mediate photostimulation across biological scales from single cells to whole organs. Although these systems mainly operate through photoelectrochemical mechanisms, capacitive stimulation driven by electrode-electrolyte charging dynamics and regarded as the clinical gold standard for neural interfaces provides superior control and biocompatibility [Merrill et al., 2005, Karatum et al., 2023, Cogan, 2008]. Emerging strategies, including gold nanoparticle functionalization of TiO_2 nanowires [Tang et al., 2018] and controlled oxygen vacancy engineering during growth [Yang et al., 2024] have shifted the photostimulation toward capacitive-dominated pho-

tocurrents. However, current strategies predominantly rely on visible light, even though infrared stimulation offers significant benefits, including greater tissue penetration and higher safety thresholds for light exposure [Cui et al., 2023, Delori et al., 2007].

Here, we demonstrate a photovoltaic nanoassembly composed of a ZnO nanowire array sensitized with $AgBiS_2$ nanocrystals (NCs) for near-infrared (NIR) photostimulation. The nanoassembly was optimized to maximize capacitive charge injection by tuning the nanowire length and interdigitating NC layer, which enables high-performance photoresponse (tens of µC cm^{-2}) at low NIR intensities (< 1 mW mm^{-2}). The nanoassembly enabled healthy and functional in vitro neuronal cultures without inducing intracellular stress, demonstrating its potential as a biocompatible optoelectronic interface for neural applications. The nanoassembly achieved reliable functional activation of the blind rat retina while operating below ocular safety limits. These findings highlight the potential of this nanoassembly as a safe and efficient interface for next-generation retinal prosthetics and infrared neuromodulation.

4.2 Methods

4.2.1 Synthesis of $AgBiS_2$ Nanocrystals

$AgBiS_2$ nanocrystals (NCs) were synthesized using a Schlenk line with a hot injection technique. Briefly, 1544 mg (4 mmol) of bismuth (III) acetate ($Bi(OAc)_3$) and 536 mg (3.2 mmol) of silver (I) acetate (Ag(OAc)) were weighed in a glovebox and added to a 100 mL three-neck round-bottom flask containing 24 mL of oleic acid (OA) and 15 mL of 1-octadecene (ODE). The flask was then sealed with a PTFE/silicone septum to prevent leakage. Subsequently, the reaction solution was increased to 100 °C under a vacuum environment and pumped for 2 hours to form Bi and Ag oleates while removing oxygen and moisture. Then, the reaction atmosphere was switched to Ar, and 4 mmol hexamethyldisilathiane (HMS) solution dissolved in 5 mL of ODE was swiftly injected into the reaction mixture. An immediate color change to dark brown was observed upon the injection into the reaction mixture, suggesting

the successful formation of $AgBiS_2$ NCs. Afterward, the heating mantle was discontinued, and the reaction mixture was allowed to cool rapidly in a water bath for approximately 5 minutes. Subsequently, the crude solution was stirred for 1 hour at room temperature. Light exposure to the reaction flasks was minimized throughout the process. $AgBiS_2$ nanocrystals (NCs) were purified via sequential precipitation. The crude solution was isolated after adding ethanol and centrifugation at 9600 rpm for 6 minutes. The precipitate was then redispersed and reprecipitated twice using toluene and ethanol. The purified $AgBiS_2$ NCs were finally dispersed in toluene at a concentration of 20 mg/mL for the fabrication of bioelectronic interfaces.

4.2.2 Synthesis of ZnO Nanowires

ZnO NWs were synthesized using the chemical bath deposition technique on an ITO/ZnO seed layer (Ossila, S111) by immersing half of the substrate in a solution (ZnO NW solution) of deionized water containing hexamethylenetetramine (0.025 mol/L), NH_3-H_2O (0.70 mol/L), polyethyleneimine (0.06 mol/L), and zinc nitrate hexahydrate (0.05 mol/L). During the process, the ZnO NWs were grown and developed on the seed layer through the reaction occurring in the solution. Following the formation of ZnO NWs on the ZnO seed layer, which was carried out at a temperature of 90 °C for varying growth durations, an annealing process was conducted at a temperature of 180 °C.

4.2.3 Characterization of $AgBiS_2$ Nanocrystals

UV-visible (UV-Vis) absorption characterization of the synthesized $AgBiS_2$ NCs was performed using a Shimadzu UV-3600 UV-Vis-NIR spectrophotometer in solution. Standard quartz cuvettes with a 1 mm optical path were employed for the absorbance measurements.

Transmission electron microscopy (TEM) and high-resolution TEM (HRTEM) analyses were conducted using a Hitachi HT7800 operating at 100 kV and a FEI TALOS F200S TEM with an accelerating voltage of 200 kV, respectively. For TEM anal-

ysis, sample preparation was performed by depositing a diluted (10 µL of a 1 mM $AgBiS_2$ NC) toluene solution onto a copper support grid. The average crystallite size of the $AgBiS_2$ NCs was determined by measuring the diameters of at least 100 nanocrystals from non-aggregated regions of the sample.

X-ray diffraction (XRD) analysis was performed on $AgBiS_2$ (NCs) at room temperature using a Rigaku Miniflex XRD with Cu K radiation ($\lambda = 0.154$ nm) and a scan rate of 5° min^{-1}. The samples were prepared by drop-casting QDs dissolved in toluene onto 1 cm x 1 cm silicon wafers. The wafers were subsequently heated to 100 °C for 1 hour to evaporate the solvent. Analysis of the XRD pattern using the Scherrer equation revealed an average crystallite size for the $AgBiS_2$ NCs.

X-ray photoelectron spectroscopy (XPS) analysis was employed to characterize the surface composition of $AgBiS_2$ NCs prior to and following ligand exchange. Measurements were conducted under ultrahigh-vacuum conditions (base pressure: 1 x 10^{-10} mbar) using a Thermo Scientific K-Alpha surface analysis instrument equipped with Al K monochromatic radiation (1486.7 eV). Binding energies were referenced to the C-C peak in the C 1s spectrum (284.6 eV) for accurate XPS data analysis. Sample preparation for XPS involved spin-coating a toluene solution containing $AgBiS_2$ NCs (20 g/L) onto pre-heated ITO substrates (20 x 15 mm^2). The substrates were heated to 110 °C and maintained at this temperature for 10 minutes to facilitate solvent evaporation under ambient conditions. A double spin-coating process was implemented, ensuring a layered film structure.

Fourier transform infrared (FTIR) analysis was performed on $AgBiS_2$ NC films before and after ligand exchange using a Thermo Scientific iS50 FTIR Spectrophotometer. FTIR samples were prepared using the same technique as XPS sample preparation.

4.2.4 Biointerface Fabrication

Photovoltaic nanoassembly was fabricated on glass or PET substrates coated with indium tin oxide (ITO). The glass/ITO (Ossila, S111) or PET/ITO (Sigma Aldrich, 639 303) substrates underwent a thorough cleaning process. The cleaning procedure was performed in an ultrasonic cleaner system set at 50 °C by immersing the substrates consecutively in the tension-active agent (HELLMANEX III):deionized water (3%, 97% by volume) for 15 min, deionized water for 15 min, acetone for 15 min, and isopropanol for 15 min. Following this cleaning process, the substrates were dried in an oven at 60 °C for 40 minutes and then treated with UV ozone for 20 minutes to eliminate any remaining residues on the ITO surface. The ZnO precursor solgel solution was prepared comprising of 219 mg of zinc acetate dehydrate ($Zn(CH_3CO_2)_22{\cdot}2H_2O$), 2 mL of 2-methoxyethanol ($C_3H_5O_2$), and 80 mg of ethanolamine ($HOCH_2CH_2NH_2$). After stirring the mixture for 5 min, the ZnO solution was sonicated for 30 min at 50 °C and filtered through a 0.22 µm PVDF filter. The P3HT (Poly(3-hexylthiophene-2,5-diyl)) with regioregularity of 95.7% and a molecular weight of 57467 g mol^{-1} (Ossila) was prepared in 1,2-dichlorobenzene solution with optimized concentrations of 20 g/L and stirred at 50 °C overnight. Ruthenium (III) chloride hydrate ($RuCl_3.H_2O$) with a molecular weight of 207.43 g mol^{-1} was purchased from Sigma–Aldrich. An aqueous solution with a concentration of 0.01 M of $RuCl_3.H_2O$ was prepared to facilitate the electrochemical deposition of ruthenium oxide (RuO_2).

For the fabrication of RuO_2-integrated ZnO NW/$AgBiS_2$ NC-based biointerface, the process began with spin coating the ZnO precursor sol-gel solution onto ITO substrates at a speed of 2000 rpm for 60 seconds. During this step, one-half of the substrate was carefully cleaned by softly wiping it with cotton swabs soaked in ethanol. Subsequently, the substrates were subjected to annealing, with glass/ITO substrates being exposed to a temperature of 275 °C for 15 minutes, while PET/ITO substrates were annealed at 200 °C for a duration of 30 minutes. ZnO NWs were synthesized via chemical bath deposition on an ITO/ZnO seed layer by dipping half

of the substrate in ZnO NW. Following the formation of ZnO NWs on the ZnO seed layer, an annealing process was performed at a temperature of 200 °C for 20 minutes. To precisely control the thickness of the interdigitated photoactive layers, the layer-by-layer deposition technique was employed on half of the substrate during the fabrication process. This technique utilized a dip coating machine, enabling the accurate application of each layer to attain the desired thickness. Consequently, the dip coating method was employed to infiltrate the ZnO NWs with a toluene solution containing $AgBiS_2$ NCs at a concentration of 20 g/L. Following the infiltration of the $AgBiS_2$ NC photoactive layer, the introduction of tetra-methyl-ammonium iodide (TMAI)-methanol (1 g/l) was carried out to enhance the electronic coupling among the NCs by substituting the insulating oleate ligands with iodide ions. Subsequently, a methanol solution was employed to rinse the substrates, aiming to remove excess oleic acid and tetramethylammonium iodide (TMAI) ligands. This was succeeded by an annealing process at 110 °C for a duration of 10 minutes. Afterward, the photoactive layer was formed by spin-coating the P3HT solution onto the ZnO NW/$AgBiS_2$ NC interdigitated layer at 1500 rpm for 60 seconds. Then, half of the substrate was cleaned by gently wiping it with cotton swabs soaked in toluene. Following these procedures, the photoactive segment of the neural interface is established on one half of the device, while the other half retained unmodified ITO. For the formation of the RuO_2 return anode electrode on the unaffected ITO section, the RuO_2 layer was electrodeposited via cyclic voltametric deposition by immersing the ITO return electrode region into 0.01 m aqueous solution of $RuCl_3.H_2O$ at room temperature and applying CV measurement for 40 cycles with 50 mV s^{-1} scan rate from -0.2 to 1.2 V with respect to Ag/AgCl bath electrode. Later, the devices underwent a rinse in distilled water and were then annealed at 50 °C for 15 minutes.

4.2.5 Characterization of Biointerface

High-resolution imaging of the nanowire array-based biointerface was performed using a Zeiss Ultra Plus field emission scanning electron microscope (SEM). Cross-sectional micrographs of the samples, both before and after layer-by-layer deposition,

were obtained to characterize the surface morphology of the ZnO NWs, $AgBiS_2$ NC films, and interdigitated active layers. All samples were examined under an accelerating voltage of 10 kV and a working distance of 3.8–4.1 mm. A thin gold layer (a few nanometers thick) was sputter-coated onto the device surface to mitigate sample charging during SEM analysis.

4.2.6 Chronoamperometry and Chronopotentiometry Measurements

For the photoelectrochemical measurements, including chronopotentiometry, chronoamperometry, electrochemical impedance spectroscopy, and cyclic voltammetry, an Autolab Potentiostat Galvanostat PGSTAT system (Metrohm, Netherlands) was employed. A three-electrode system was employed, comprising a platinum rod counter electrode, an Ag/AgCl reference electrode, and the ITO layer of the biointerface as the working electrode. Precisely 1 cm^2 substrate area, and the other two electrodes were immersed in an extracellular artificial cerebrospinal fluid (aCSF) as the electrolyte medium at room temperature to simulate the in vivo environment. A red LED was utilized as a light source. Data acquisition and analysis were conducted using NOVA software. The optical power density of the applied light illumination on the biointerface was measured with an optical power meter (Newport 843-R).

4.2.7 Finite-Difference Time-Domain (FDTD) Simulations

To elucidate the physical origin behind the absorption enhancement via the use of ZnO nanowires, we performed finite-difference time-domain (FDTD) simulations and compared the results with experimental outcomes. In the FDTD simulations, we used a simulation cell containing a single ZnO nanowire, where periodic boundary conditions were applied along the xy-plane to model the array behavior, and a perfectly matched layer (PML) boundary condition was used along the direction of the illumination light source (z-axis). Figure S12 shows the refractive index properties of the materials used in the FDTD simulation [Cheng et al., 2018, Wang et al., 2022]. Figure S11 shows the experimental and calculated absorption spectra for different dip coating cycles in the presence (dashed curves) and absence (solid

curves) of ZnO nanowires, demonstrating their excellent correlation.

4.2.8 Photocurrent Measurements

Measurements were conducted using an Olympus T2 upright microscope and EPC-800 patch clamp amplifiers (HEKA Elektronik GmbH, Pfalz, Germany). The aCSF medium was prepared by mixing 10 mm of 4-(2 hydroxyethyl)-1-piperazineethanesulfonic acid (HEPES), 10 mm glucose, 2 mm $CaCl_2$, 140 mm of NaCl, 1 mm of $MgCl_2$, and 3 mm of KCl, and distilled water. The pH of the aCSF medium was adjusted to 7.4 using a stoichiometric amount of NaOH solution. A red LED (M780LP1, Thorlabs) was employed as the light source, driven by a pulse-modulated LED driver (DC2200-High-Power 1-Channel, Thorlabs) to generate 20 ms light pulses. The electrolyte solution was grounded to simulate a biological environment, while the ITO layer remained ungrounded. Photocurrent measurements were then conducted.

4.2.9 Primary Neuron Isolation

All experimental procedures have been approved by the Institutional Animal Care and Use Committees of Koç University (Approval No: 2022.HADYEK.048) according to Directive 2010/63/EU of the European Parliament and of the Council on the Protection of Animals Used for Scientific Purposes.

The hippocampi tissue was isolated from the brains of embryos of Wistar Albino rats on days E16-E18. The tissue was put directly into ice-cold Hank's Balanced Salt Solution (HBSS) including falcon tube. After taking the falcon to the sterilized cell culture hood, the tissue was washed with sterile ice-cold HBSS two times. Then, 0.25% Trypsin-EDTA solution with 2% DNase-I supplement was added to the tissue for a 20-minute incubation in a 37 °C water bath for enzymatic digestion. During this time, the tube was made upside down for better digestion. Afterward, Dulbecco's Modified Eagle Medium / Nutrient Mixture F-12 (DMEM / F12) supplemented with 10% fetal bovine serum (FBS) and 1% penicillin/streptomycin was added and centrifuged at 300 g for 3 minutes. After the centrifugation, DMEM/F12

was carefully discarded, and the tissue was washed with DMEM/F12 two times. After discarding the DMEM/F12, Neurobasal Plus medium supplemented with B27, L-glutamine, B-mercaptoethanol, glutamate, 1% penicillin/streptomycin was added to the cell pellet and triturated with plastic Pasteur Pipette for homogenizing the cells. The mixed solution was dissociated through a 70 µm cell strainer.

Then, 500 000 cells per well were seeded to each substrate. The well-plate was put in the 37 °C cell culture incubator with 5% CO_2 and incubated for 3 days unmoved. On the third day, half of the medium of the cells were changed with the NBM-supplemented cytosine arabinoside to inhibit the overgrowth of glial cells and then, incubated for 24h in a cell culture incubator. Next day, the entire medium was replaced with Neurobasal Medium (NBM) supplemented with B27, L-glutamine, and 1% penicillin/streptomycin. Until use in the experiments, half of the culture medium was replaced with fresh NBM every 3-4 days.

4.2.10 Cell-Titer-Glo Luminescent Cell Viability Assay

Cell-Titer-Glo Luminescent Cell Viability Assay (CTG, Promega, Mannheim, Germany) was used to examine the viability of primary hippocampal neurons on the surface of ITO and fabricated devices. On day 0, the well plate was taken from the incubator and left at room temperature for 30 minutes. Then, Cell-Titer-Glo® Reagent was added to each well and the plate was put on the orbital shaker for 5 minutes and incubated in RT for 10 minutes for stabilization of luminescence signals. Then, each solution inside the wells was transferred to a 96-well opaque plate. Synergy H1 Microplate Reader (Bio-Tek Instruments) was used to measure the luminescence signals. The relative cell viability of samples of each substrate was calculated from comparing luminescence signals (RLUs)'s of fabricated devices with the ones of ITO control.

4.2.11 MTT Cytotoxicity Assay

MTT cytotoxicity assay was used to analyze cell viability based on the reduction of a yellow tetrazolium salt (3-(4,5-dimethylthiazol-2-yl)-2,5-diphenyltetrazolium bromide MTT) to purple formazan crystals by metabolically active cells. At day 0, Neurobasal Plus medium supplemented with B27, L-glutamine, and 1% penicillin/streptomycin in the wells was replaced with Neurobasal Plus medium including 5 mg/ml MTT solution (Thermo Fisher Scientific, MA, USA). The culture plate was incubated at 37 °C, 5% CO_2 in a cell culture incubator for 4h. After the incubation, all substrates were taken to a new 6-well plate and a 1:1 mixture of DMSO and ethanol was added to the samples for solubilizing the formazan salts and incubated at 37 °C for 10 minute. Then, the solution in each well was transferred to a 96-well plate. Synergy H1 Microplate Reader (Bio-Tek Instruments) was used to measure the absorbance at 570 nm wavelength. The relative cell viability of each substrate was calculated normalizing the control ITO as follows: Viability = (ODsample/ODcontrol) × 100. The optical density (OD) of the sample was obtained from the cells grown on fabricated device, and the OD of control was obtained from the cells grown on the ITO.

4.2.12 Lactate-dehydrogenase Release Assay

For Lactate-dehydrogenase Release Assay, CytoSelectTM LDH Cytotoxicity Assay Kit (CBA-241, Cell Biolabs) was used to examine the cell membrane stability of primary neuronal cells cultured on the samples. As a positive control of the experiment, the cells on the ITO substrates were incubated with culture medium containing 1% Triton-X-100 for 10 minutes at 37 °C in a 5% CO_2 cell culture incubator to induce LDH leakage. All experimental and control groups were incubated with the medium including 1% water for 10 minutes then 90 µL of culture medium was taken from each sample and added to transparent 96-well cell culture plates. Thereafter, 10 µL of LDH cytotoxicity assay reagent was added to each well, and the plates were incubated at 37 °C in a 5% CO_2 incubator for 30 minutes to allow to the reaction to occur. The Synergy H1 Microplate Reader (BioTek) device was used to measure the

amount of LDH leaked into the culture medium at 450 nm optical density.

4.2.13 Immunofluorescence Staining and Imaging

On day 0, the samples of substrates were fixed with 4% paraformaldehyde for 20 minutes in a fume hood and washed with PBS-T (Phosphate Buffered Saline, 0.1% Tween-20) three times. Then, 0.1% Triton X-100 was added to the samples and incubated for 8 minutes for permeabilization following washing with PBS-T. Super-block was used to perform blocking for 10 minutes at room temperature. The samples were incubated at 4 °C overnight with rabbit anti-NeuN antibody (ab177487, Abcam, Cambridge, UK) and anti-b-III Tubulin antibody (ab18207, Abcam, Cambridge, UK), all prepared in the superblock. After incubation, the samples were washed with PBS-T three times. For anti-NeuN and anti-b-III Tubulin labeling, the samples were incubated with goat anti-rabbit IgG HL Alexa Fluor 488 (Cell Signaling Technology, MA, USA) for 90 minutes at 37 °C. After the incubation, all samples were washed three times using PBS-T and mounted with a DAPI-supplemented mounting medium (50001, Ibidi GmbH, Germany). All immunofluorescence images were taken by inverted fluorescence light microscope (Axio Observer Z1, ZEISS, Oberkochen, Germany). For day 14 experiments, the same procedure was established on the 14th day of culture.

4.2.14 Intracellular Oxidative Stress Measurement

The intracellular oxidative stress level was measured by cellular ROS assay kit 2′, 7′-dichlorodihydrofluorescein diacetate (H_2DFCDA) (ab113851, Abcam). Primary hippocampal neurons were seeded on control and device as 500000 cell/well and cultured until DIV14. Experimental groups included ITO control, device before illumination and after illumination and positive control with neurons grown on the control substrate treated with 100 µM H_2O_2 for 30 min. For the experiment, cells were washed once with PBS then incubated with 20 µM H_2DFCDA in live cell solution for 45 min before imaging at 37 °C, 5% CO_2. Hoechst (0.6 mg/ml) was used to stain the nucleus prior to imaging for 15 min. After incubation, cells were washed

twice with PBS and then incubated with a live cell solution for 10 min at room temperature to stabilize the signals. All immunofluorescence images taken in same light intensity, exposure, time point, and magnification with live-cell fluorescence microscope (Axio Observer Z1, ZEISS, Oberkochen, Germany) and average fluorescence intensity was measured by Zen Blue 3.5 software. Light stimulation group was prepared with exposure of 780 nm light with 10 000 cycles, illumination: 5 Hz stimulus frequency, 20 ms pulse-width, 1.5 $mW.mm^{-2}$ optical power density. Florescence intensity of ITO control accepted as 100% in relative fluorescence intensity comparison.

4.2.15 Mitochondrial Membrane Potential (MMP) Assay

MMP was analyzed using JC-1 Assay (T3168, Invitrogen), in accordance with the manufacturer's protocol. Briefly, primary hippocampal neurons were seeded onto control and device as 500 000 cell/well and cultured for 5-7 days. The cells were stained with 1 µM JC-1 prepared in live cell solution (Invitrogen Cat no A59688DJ) at 37 °C and incubated for 30 min in the dark. They were then washed twice with PBS to remove excess dye, and JC-1 fluorescence was observed via confocal laser scanning microscope (DMI8 SP8, Leica, Wetzlar, Germany). Cells were subjected to 780 nm light for 20 sec with 5 Hz stimulus frequency, 20 ms pulse-width, 1.5 $mW.mm^{-2}$ optical power density. Mean florescence intensity of JC-1 red aggregate and JC-1 green monomer was quantified and processed using LASX software (Leica, Germany).

4.2.16 Rat Retina Preparation, Electrophysiological Recording and NIR Stimulation

Experiments were conducted in accordance with the National Institutes of Health Guide for the Care and Use of Laboratory Animals. Studies were approved by the Local Animal Ethics Committee and conducted in agreement with Directive 2010/63/EU of the European Parliament. P23H male transgenic rats (> 9 months) were raised locally.

Using a custom 3D-printed descender, an implant (photovoltaic device of 2 x 2 mm^2) was positioned on the center of a filter membrane (Whatman, GE Healthcare Life Sciences). Retinal pieces were then flattened on the membrane, entirely covering the implant and then gently pressed against an MEA (electrode diameter, 30 µm; spacing, 100 µm; MEA256 100/30 iR-ITO, MultiChannel Systems) with the RGCs facing the electrodes. The retinal tissue was continuously perfused with Ames' medium (Sigma–Aldrich) bubbled with 95% Otextsubscript2 and 5% COtextsubscript2 at 35 °C at a rate of 3 ml min^{-1}. RGC recordings were obtained with a 252 channel preamplifier and MC_Rack v. 4.6.2 software (MultiChannel Systems).

We observed that the tighter the contact between the implant and the retina was, the more current generated by the implant was transmitted to the retina (visible in MEA recordings in the form of larger artifacts, with a positive saturating amplitude $>$ 2 mV). But on the other hand, the stronger the contact, the greater the risk of hypoxia for the retina, causing a potential rapid loss (in the minute range) of spiking spontaneous activity and light responses. We used for all experiments an output light power density of 2.27 $mW.mm^{-2}$, to maximize the effect of the implant without having to press too much the implant on the retina.

Raw extracellular recordings were acquired from a 256-channel microelectrode array (MEA), .MCD raw data files were exported to .HDF5 file format and processed using a Butterworth bandpass filter (300–2000 Hz) to isolate neuronal spiking activity. Electrical artefacts were detected and averaged across occurrences to compute an artefact template, which was subtracted from the raw signal to significantly remove NIR stimulation-induced distortions. Spikes were detected using the first derivative of the artefact-cleaned signal, selecting negative peaks exceeding an adaptive threshold (-4.5×SD). Events occurring within saturating laser artefact windows were excluded, with a margin of 1 ms before and after the artefact to ensure robust detection. No spike-sorting was performed since recordings were generally not stable enough or too short, therefore the activity of individual MEA units may reflect the combined activity of multiple RGCs.

MEA units were classified as active if their mean firing rate exceeded a predefined threshold (e.g., 0.5 Hz) during a control period of spontaneous activity. Responsive units were detected based on calculation of Spike Density Function (SDF) using Gaussian smoothing and determination of the peak response within a predefined time window following the stimulation onset. A unit was classified as responsive if the peak SDF or 'peak firing rate' exceeded 4.5×SD of baseline activity. Latencies were calculated as the time between stimulus onset and the time of the SDF peak. Spatial heatmaps and smoothed temporal heatmaps were generated to illustrate network-wide activation patterns. For spatial heatmap representation (normalized firing rates), only active units were color-coded between 0 and 1, dark blue (value 0) corresponding to active but non-responsive units and pure yellow (value 1) corresponding to the unit presenting the maximum response. Data were filtered, cleaned and analyzed with custom scripts written in MATLAB (MathWorks 2023a).

Light stimuli were delivered with a single-mode NIR laser source (880 nm, 2.5 W, Laser 2000) coupled to a digital micromirror device (Vialux; resolution, 1,024 × 768) and a 4x objective using an inverted microscope. The implant was stimulated through the MEA and the retina. Recording sessions consisted of 100 repetitions at 5 Hz of short NIR laser stimulations (period of 200 ms). Different stimulation pulse widths were tested: 5, 10, 20 and 50 ms. Output power density was measured with a power meter sensor (sensor S121C, Thorlabs) positioned at the level of the retinal explant.

4.2.17 Optical Safety Considerations

The maximum permissible radiant power (MP) for chronic retinal exposure is determined in accordance with established eye safety standards [Delori et al., 2007]. In the Near-Infrared (NIR) region, the photochemical damage limit is not applicable. For photothermal and photoacoustic limits, the MP is calculated using the equation: $MP = 6.93 \times 10^{-5} C_{\mathrm{T}} C_{\mathrm{E}} \mathrm{P}^{-1}$. $C_{\mathrm{T}} = 10^{0.002(\lambda\text{-}700)}$. Here, the pupil factor (P) equals one between 700 and 1400 nm wavelengths of light. Considering a retinal spot size

larger than 1.7 mm, based on a previous study [Mathieson et al., 2012], is taken as 29.3 W mm^{-2}. For single-pulse exposures with durations ranging from 0.05 to 70 ms, the limit is given by $MP_{\text{single}} = 6.93 \times 10^{-4} C_{\text{T}} C_{\text{E}} t^{-0.25}$.While these equations provide average irradiance limits, the peak irradiance limits (MP_{peak}) can be derived using the formula: $MP_{\text{avg}/(txf)}$, where t is the pulse duration and f is the pulse frequency.

4.3 Results

4.3.1 Device Fabrication and Operation

The device has a photovoltaic nanoassembly composed of ZnO NWs and $AgBiS_2$ NCs as the stimulation electrode and a pseudocapacitive layer of RuO_2 as the return electrode. For the nanoassembly fabrication, we followed a multi-step process that mainly included the vertical growth of the ZnO nanowire array and interpenetration of nanocrystals (Figure 4.1).

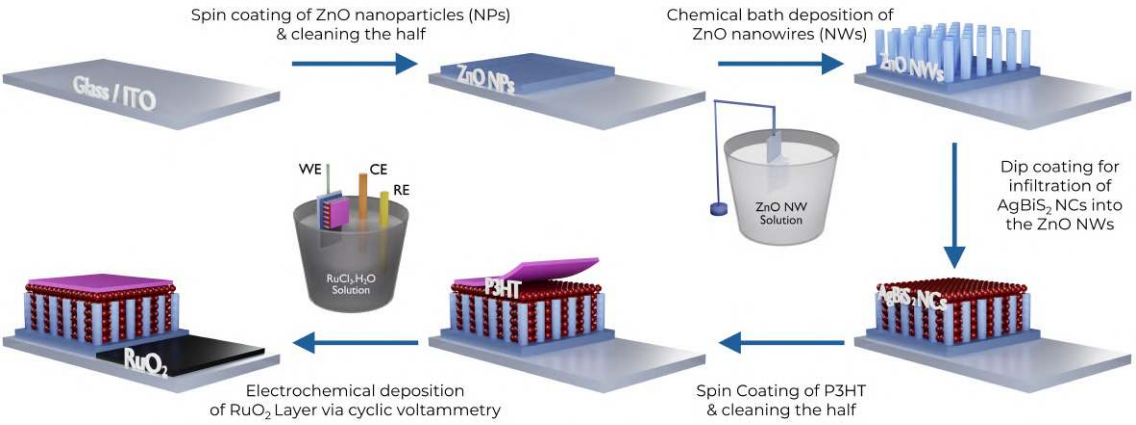

Figure 4.1: **Device fabrication.** The fabrication flow schematic of the photovoltaic nanoassembly. (Not drawn in scale).

We started the fabrication of the solution-processed photovoltaic nanoassembly by forming a 30-nm ZnO seed layer onto indium tin oxide (ITO) and we grow the ZnO NW arrays via chemical bath deposition (CBD), which can be controlled within the range of 90 nm to 350 nm by adjusting the duration of the CBD (Figure 4.2). We selected to grow ZnO NWs with a mean length of 240 nm on the seed layer and an average interspacing of 30 nm (Figure 4.3a, b).

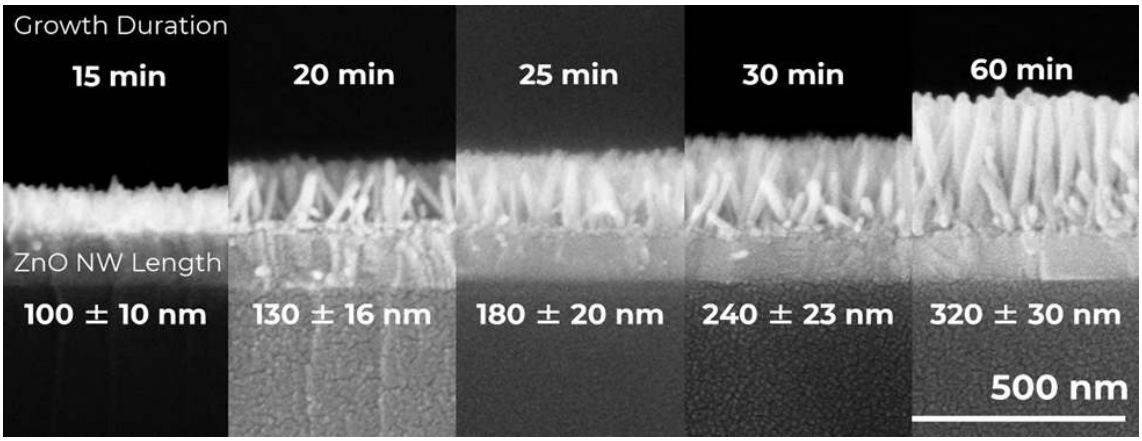

Figure 4.2: **Nanowire growth.** SEM images of ZnO nanowires with different growth duration.

As the photoabsorption layer, we selected $AgBiS_2$ nanocrystals due to its exceptional absorption coefficient reaching over 105 cm^{-1}, high photostability and being free from toxic-heavy-metals such as cadmium and lead (Figure S2). ZnO and $AgBiS_2$ form a proper Type-II heterojunction for dissociation of the photogenerated charges for photovoltaic process.

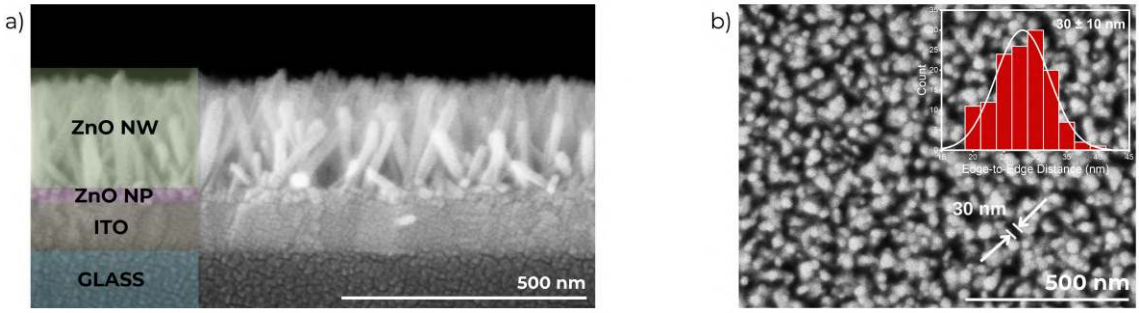

Figure 4.3: **Nanowire optimization.** Cross-sectional a) SEM image of ZnO NWs. b) SEM image of the top view of ZnO NWs (the inset is the edge-to-edge distance of the ZnO NW distribution histogram and the calculated average distance).

The synthesis of colloidal $AgBiS_2$ nanocrystals was done by using a hot injection method (Figure 4.5) based on the reaction of silver (I) acetate (Ag(OAc)), bismuth (III) acetate ($Bi(OAc)_3$), and hexamethyldisilathiane (HMS) solution dissolved in 1-octadecene (ODE) as the sulfur source that yielded a mean NC size of 4.3 ± 1.4 nm (Figure 4.6a).

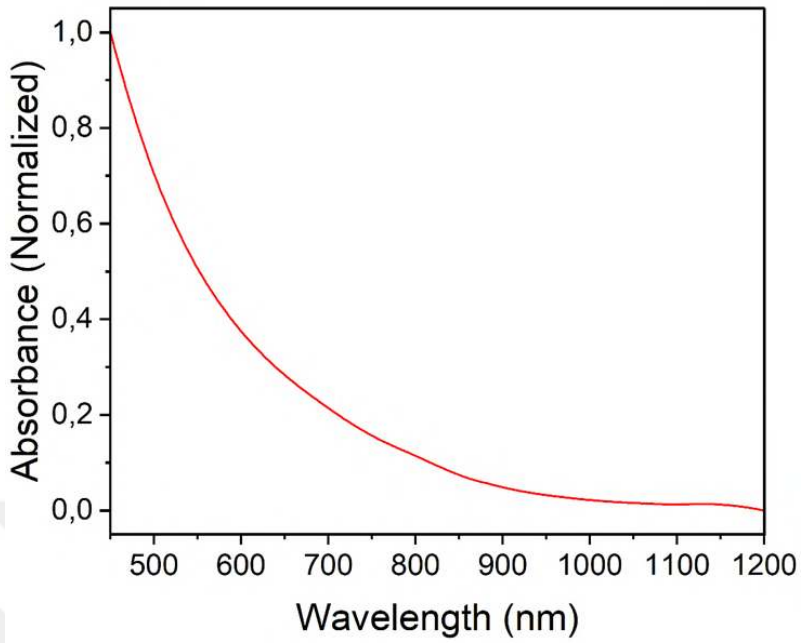

Figure 4.4: **Quantum dot absorbance.** Absorbance spectrum of $AgBiS_2$ QDs dispersed in toluene (20 g/L).

The X-ray diffraction (XRD) pattern of the $AgBiS_2$ NCs revealed a rock salt crystal structure (Figure 4.6b) and the average size estimation using the Scherrer equation (ca. 4.2 nm) was also in close agreement with the transmission electron microscopy (TEM). Subsequently, nanocrystals were introduced into the ZnO NWs by using a layer-by-layer deposition technique, which allows for precise control of the thickness of the interdigitated nanocrystal layer (Figure 4.6c).

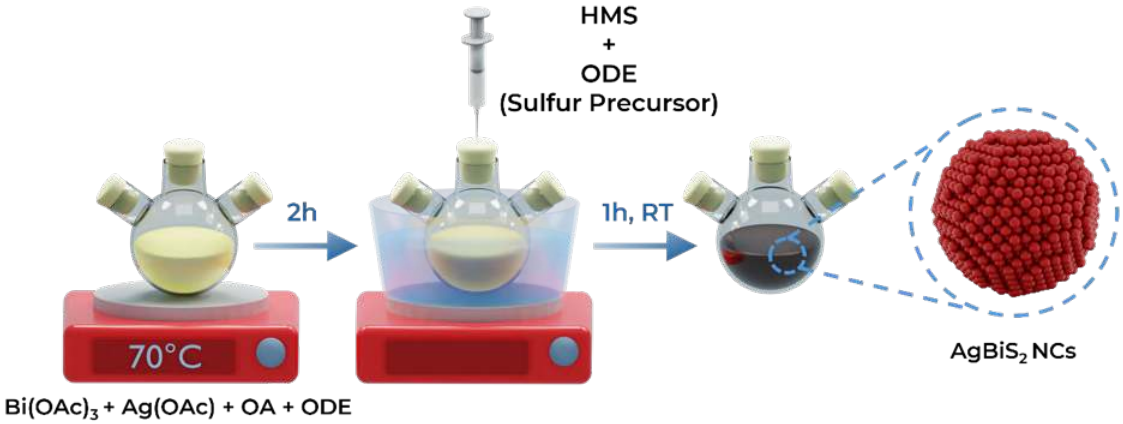

Figure 4.5: **Quantum dot synthesis.** Schemaic of $AgBiS_2$ QDs synthesis.

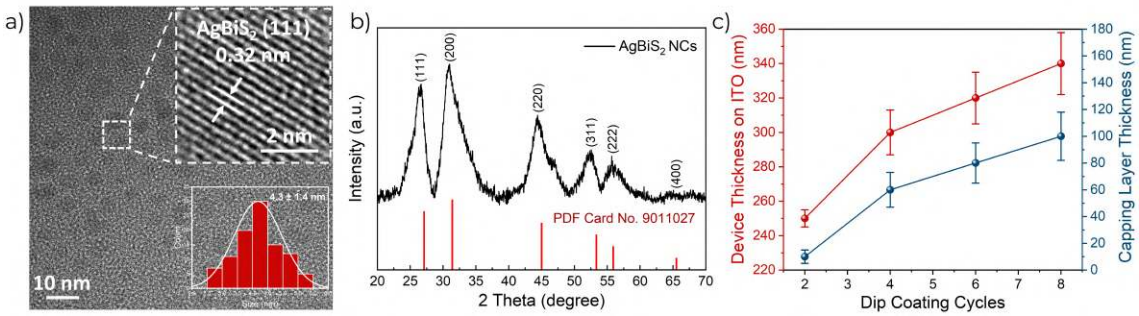

Figure 4.6: **Quantum dot characterization.** a) TEM image of $AgBiS_2$ NCs. Inset shows the NC size distribution histogram and the calculated average size 4.3 ± 1.4 nm). b) XRD pattern of $AgBiS_2$ NCs. c) $AgBiS_2$ layer thickness vs implemented dip coating cycles.

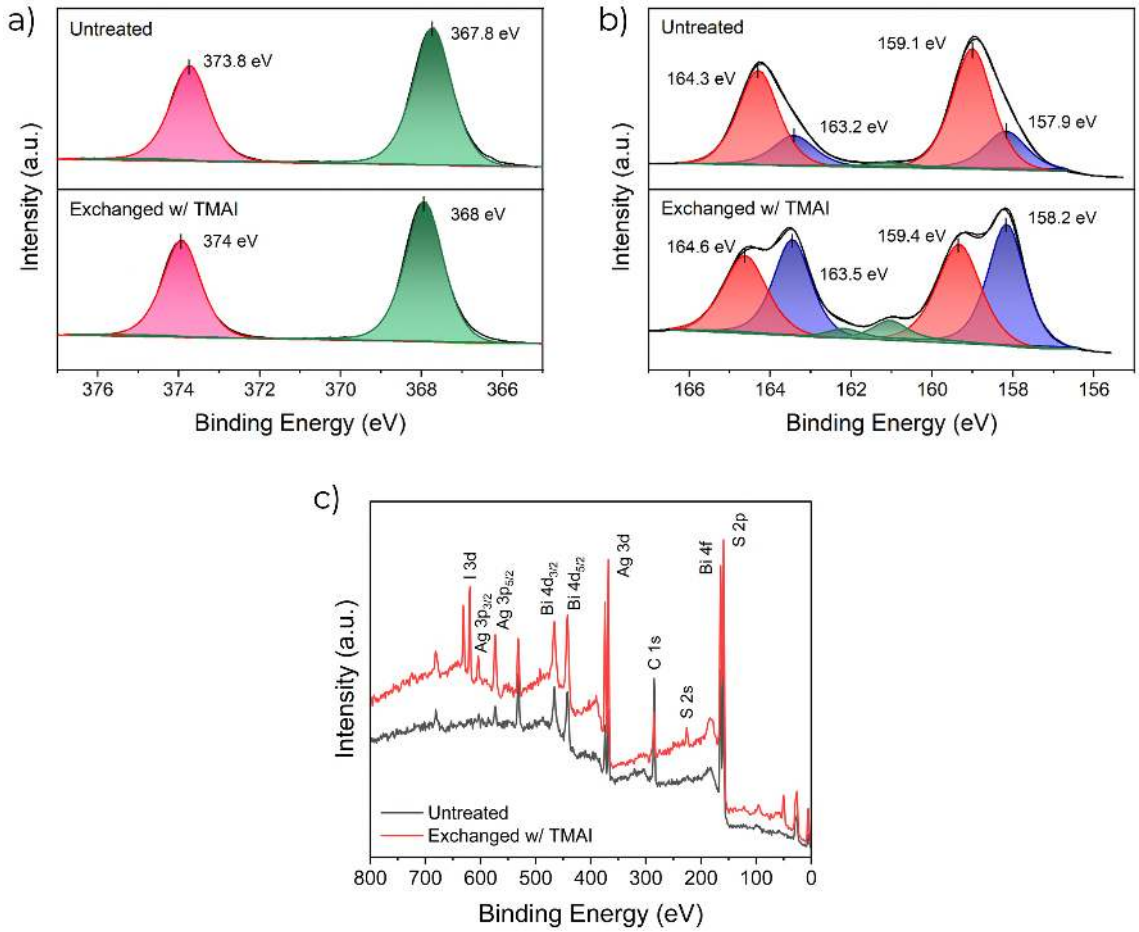

Figure 4.7: **Characterization of QDs after the ligand exchange process by performing XPS measurement.** XPS spectra of (a) Ag 3d, (b) Bi 4f and (c) XPS survey spectrum of $AgBiS_2$ for the ZnO NW/$AgBiS_2$ devices before and after ligand exchange.

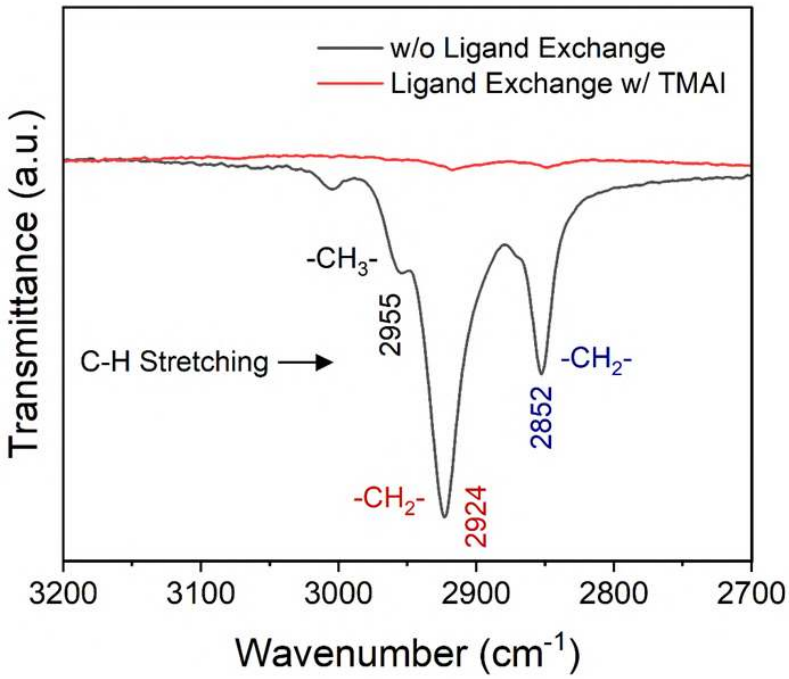

Figure 4.8: **Characterization of QDs after the ligand exchange process by performing FTIR measurement.** FTIR spectrum of ZnO NW/ $AgBiS_2$ device before and after ligand exchange process.

Since the electron diffusion length in $AgBiS_2$ is limited around 60 nm, which is much shorter than the hole diffusion length (150 nm) [Diedenhofen et al., 2019], ZnO NWs facilitate effective charge dissociation via interpenetration within the $AgBiS_2$ NCs [Xiao et al., 2021].

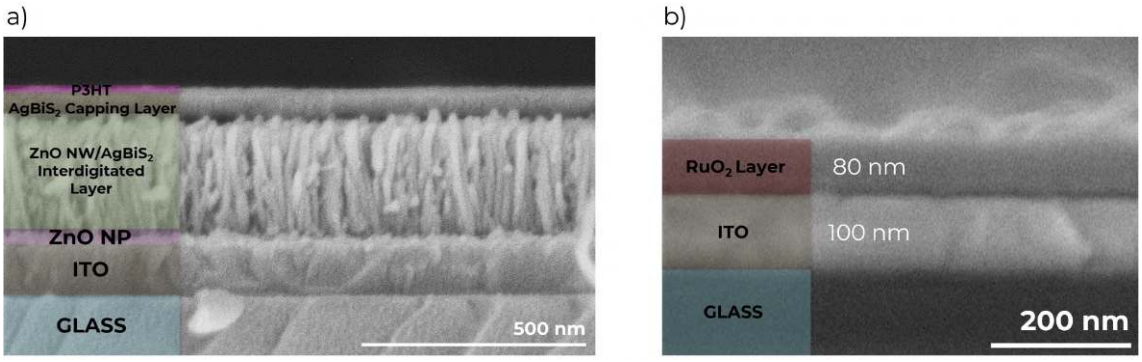

Figure 4.9: **SEM image of the optimized photovoltaic nanoassembly architecture.** a) Cross-sectional SEM image of the nanoassembly. b) Cross-sectional SEM image of 40-cycle deposited RuO_2 layer.

Then tetra-methyl-ammonium iodide (TMAI) was applied to exchange long-chain insulating oleate ligands with small-chain iodide ions to enhance the electronic coupling between the NCs. X-ray photoelectron spectroscopy (XPS) showed the removal of oleates by a shift towards higher binding energies originating from Ag 3d (367.8 and 373.8 eV) and Bi 4f (157.9 and 163.2 eV) (Figure 4.7). The successful ligand exchange was further confirmed by Fourier transform infrared spectroscopy (FTIR) by the disappearance of oleate absorption bands characteristic of -CH2- and -CH3- functional groups (2850-2960 cm^{-1}) (Figure 4.8).

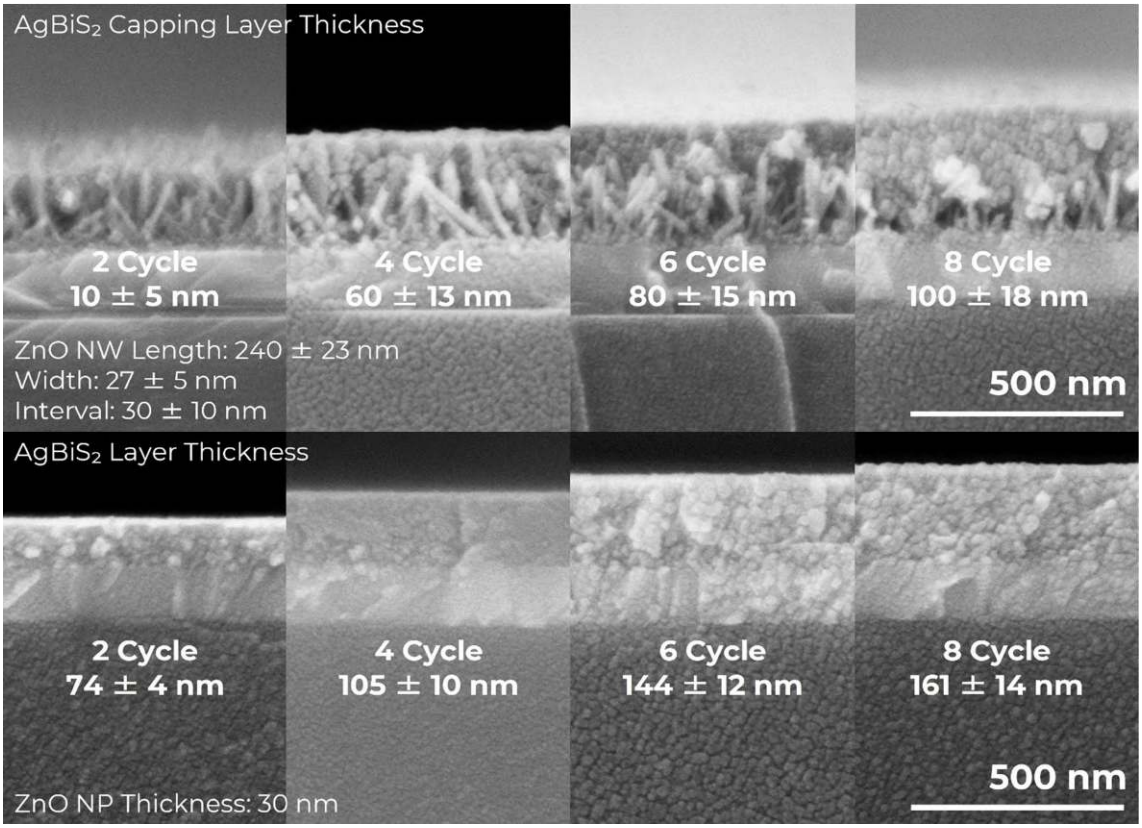

Figure 4.10: **Quantum dot layer thickness optimization.** Cross-sectional SEM images of ZnO Nanowire/$AgBiS_2$ devices with different dip coating cycles of $AgBiS_2$ QDs over ZnO nanowire (above), and ZnO nanoparticle (bottom).

The thickness of the capping layer (NC thickness above the nanowire array) is adjusted to 80 nm (Figure 4.9a), which can be well controlled by changing the dip-coating cycle (Figure 4.10).

Afterward, a water-stable and biocompatible polymer of poly 3-hexylthiophene (P3HT) with a thickness of 30 nm was deposited as the hole transport layer (HTL) to complete the photoactive part of the photovoltaic nanoassembly. For the formation of the return electrode, 40-cycles of electrodeposition of ruthenium oxide (RuO_2) layer with a thickness of 72 ± 13 nm are done via cyclic voltammetry on the bare ITO side of the device to enhance the electrode-electrolyte capacitance (4.9b).

4.3.2 Photoelectrochemical Characterization

We did photoelectrochemical characterization in artificial cerebrospinal fluid (aCSF), which has the nanoassembly as the working electrode under light irradiation, Ag/AgCl serves as the reference electrode, and the platinum as the counter electrode (Figure 4.11a).

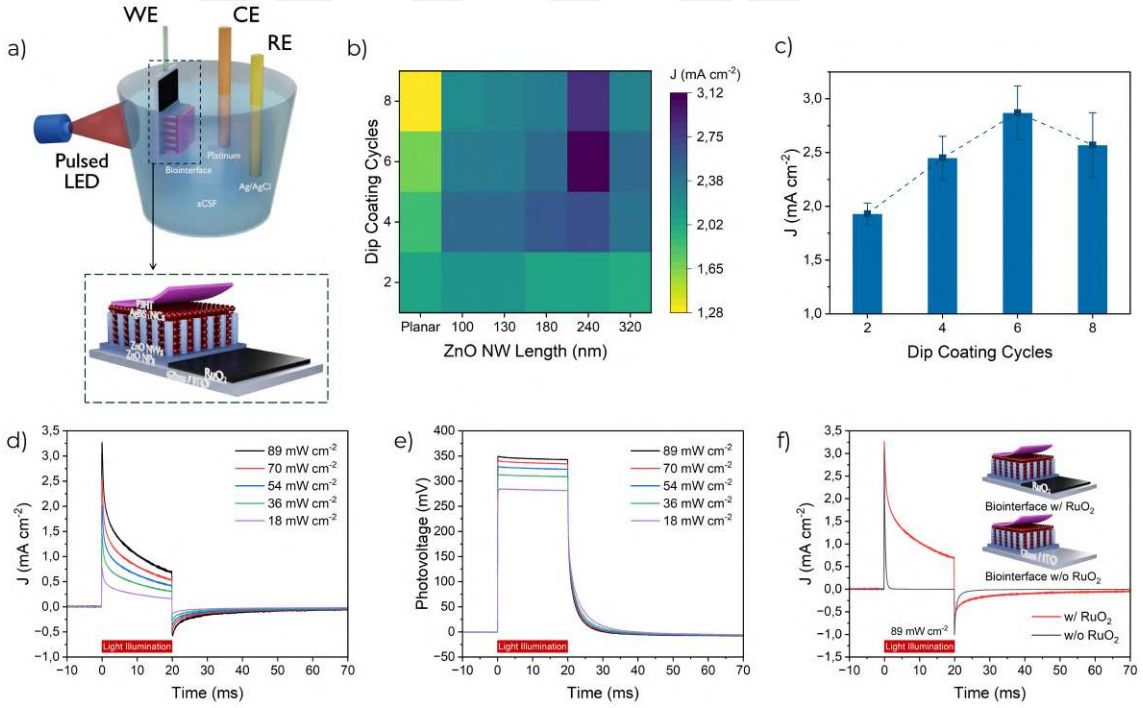

Figure 4.11: **Photoelectrochemical characterization.** a) Schematic illustration of the three-electrode potentiostat for photocurrent and photovoltage measurement. b) Photocurrent density of the nanoassemblies with different nanowire length and nanocrystal deposition combinations. c) Photocurrent density for different dip coating cycles under NIR light illumination. d) Photocurrent density, and e) photovoltage of biointerface after RuO_2 integration under different light intensity levels (λ = 780 nm). f) Photocurrent density of the nanoassembly with and without RuO_2 under the illumination of 89 mW.cm^{-2}. Inset illustrates the measured devices.

To understand the charge-injection characteristics of the photovoltaic nanoassembly, we fabricated a series of devices with varying nanowire lengths in combination with different cycles of NC deposition (Figure 4.11b). Photocurrent increases with nanowire length up to about 240 nm, after which the performance drops rapidly with further extension. Using 240 nm ZnO nanowires, the photovoltaic nanoassembly generated maximum photocurrent and photovoltage values of 3.27 mA cm^{-2} and 350 mV with an 80 nm capping layer (i.e., 6-cycles of dip-coating) (Figure 4.11c) under NIR illumination (λ = 780 nm, 89 mW·cm^{-2}), respectively, (Figure 4.11d, e). The charge injection density corresponded to 20.96 ± 2.2 µC cm^{-2} ($mean \pm SEM$, n = 10) (Figure 4.11f), which is sufficiently high to meet the needed thresholds for in-vivo stimulation [Cogan, 2008] and 20 times higher than the device without the RuO_2 layer.

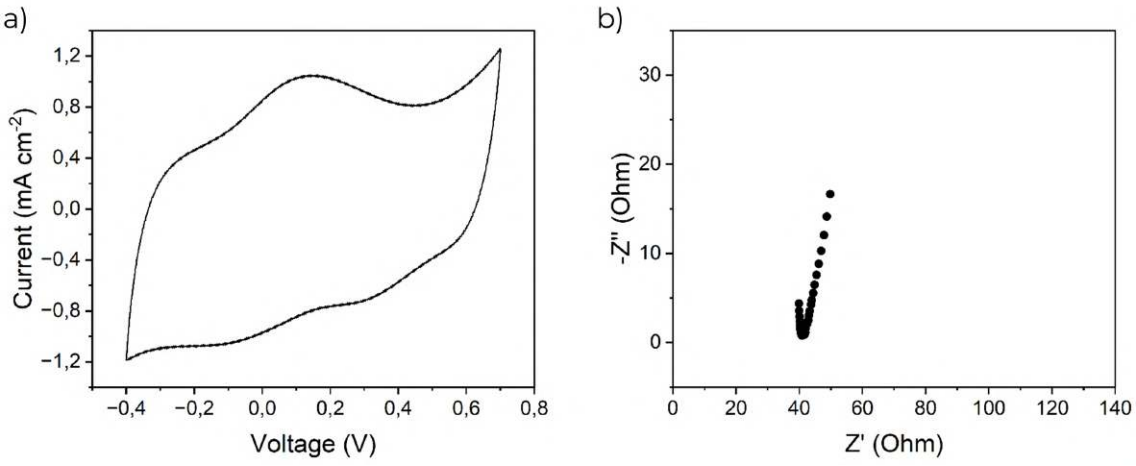

Figure 4.12: **Electrochemical characterization of RuO_2 layer.** a) Cyclic voltammogram of 40-cycle RuO_2 coating from -0.4 to 0.7 V range. Scan rate is 50 mV s^{-1}. b) Electrochemical impedance measurement of 40-cycle RuO_2 coating within the frequency range of 1–10 000 Hz.

The observed symmetric and quasi-rectangular shapes of the cyclic voltammograms of RuO_2 reveal the capacitive behavior of the films and the presence of reversible redox reactions, which is the preferred mechanism for safe neurostimulation (Figure 4.12a, b). The cathodic charge storage capacity (CSCc) of RuO_2 was 15.3 ± 2.1 mC cm^{-2} and the capacitance corresponded to 31.2 ± 1.2 mF cm^{-2} ($mean \pm SEM$).

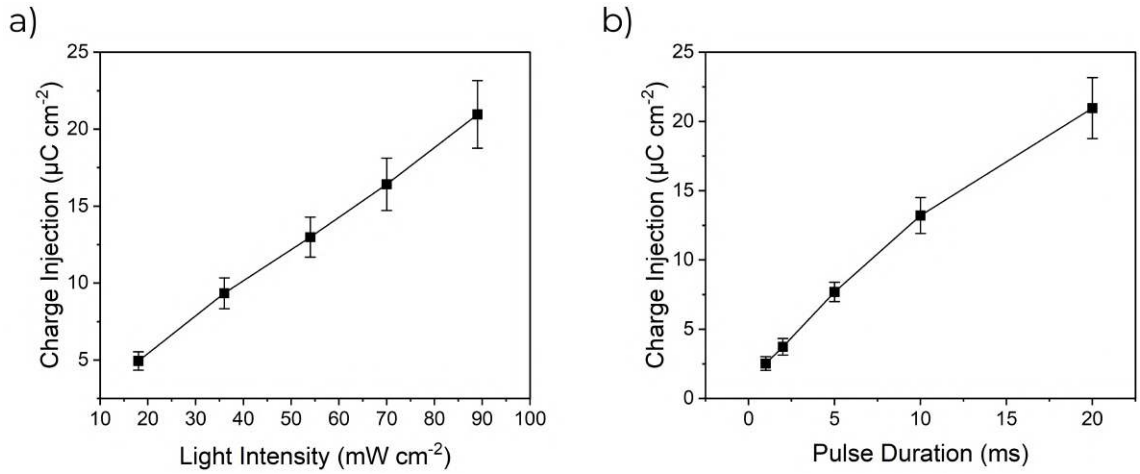

Figure 4.13: **Charge injection optimization.** a) Charge injection of the nanoassembly as a function of light intensity. b) Photogenerated charge injection of the nanoassembly for different pulse durations.

We also quantified the photoresponse of the nanoassembly under various illumination conditions. The charge injection by the nanoassembly can be modulated by light intensity (Figure 4.13a) and pulse duration (Figure 4.13b). For example, under a short pulse duration (1 ms, 89 mW·cm^{-2}), the photovoltaic nanoassembly delivers 2.52 ± 0.5 µC·cm^{-2} ($mean \pm SEM$, n = 10) (Figure 4.13b), which falls within the threshold range required to stimulate various neural tissues, such as the auditory brainstem and subthalamic nucleus [Cogan, 2008].

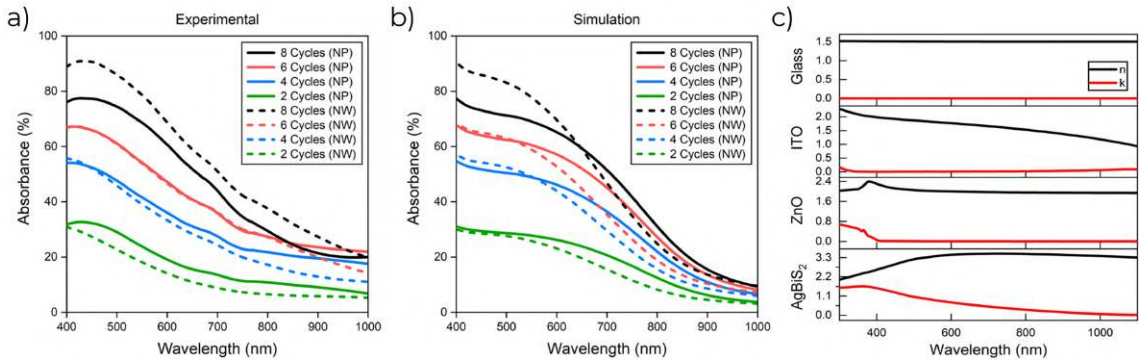

Figure 4.14: **Optical constants for FDTD simulations.** a) Experimental and b) calculated absorption spectra for different dip coating cycles in the presence (dashed curves) and absence (solid curves) of ZnO nanowires. c) Real (black curves) and imaginary (red curves) parts of the refractive index of the materials used in the FDTD simulations.

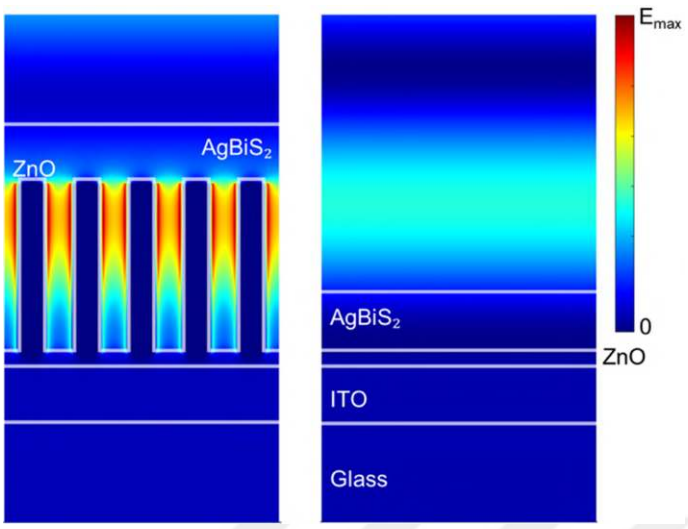

Figure 4.15: **FDTD simulations.** Nearfield intensity distribution of the nanoassembly (left) demonstrating strong electromagnetic field localization between nanowires compared to nanowire-absent case (right).

The experimental and simulated absorption spectra for different dip-coating cycle numbers, along with the real (n) and imaginary (k) parts of the refractive index of the materials, were employed as the optical constants for the FDTD simulations (Figure 4.14a, b).

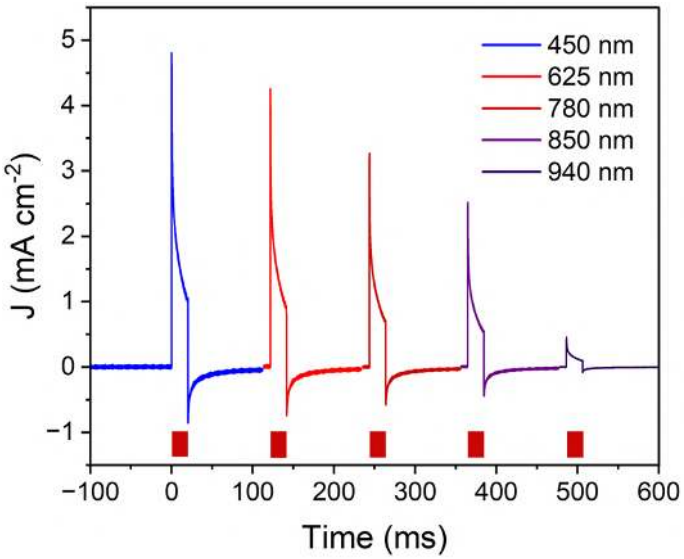

Figure 4.16: **Photocurrent at varying wavelengths.** Photocurrent response as a function of illumination wavelength.

FDTD simulations show that the localized electromagnetic fields with extensive intensity enhancements are finely confined along the ZnO nanowire interstices for effective photogeneration (Figure 4.15). Moreover, our analysis into the photoresponse at varying wavelengths (Figure 4.16) revealed a larger photocurrent for 450 and 625 nm light illumination than the NIR illumination, which can be attributed to the absorption of blue light by the P3HT layer and the enhanced oscillator strength of $AgBiS_2$ QDs at shorter wavelengths.

Finally, we assessed the photoelectrical properties of the nanoassembly in a free-standing and wireless retina implant condition. For that, the nanoassembly was diced into a 2 mm x 2 mm size (Figure 4.17).

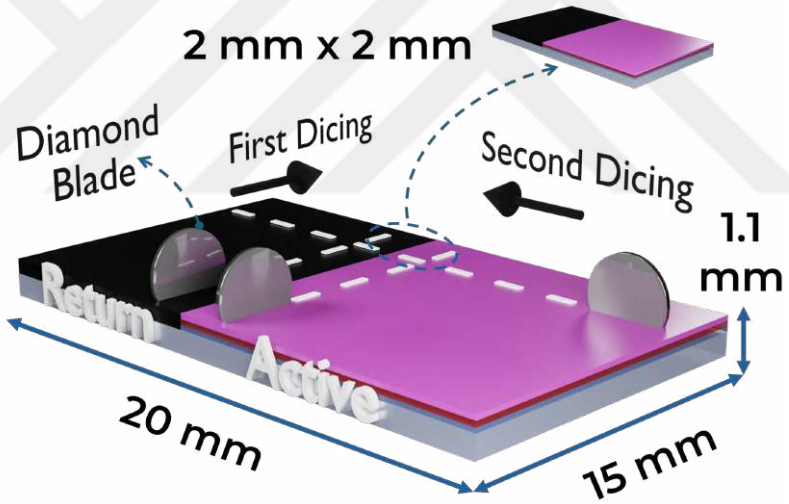

Figure 4.17: **Miniaturized nanoassembly.** Schematic illustration of the dicing process of the nanoassembly.

The nanoassembly was immersed in aCSF, and a glass capillary counter electrode and a remote Ag/AgCl reference electrode were employed in voltage-clamp mode using a patch pipette filled with intracellular solution positioned near the biointerface surface (Figure 4.18a). The nanoassembly exhibited a peak photocurrent of 2.7 ± 0.2 nA at the position indicated by the blue circle under NIR illumination (λ = 780 nm, 2 mW mm^{-2}).

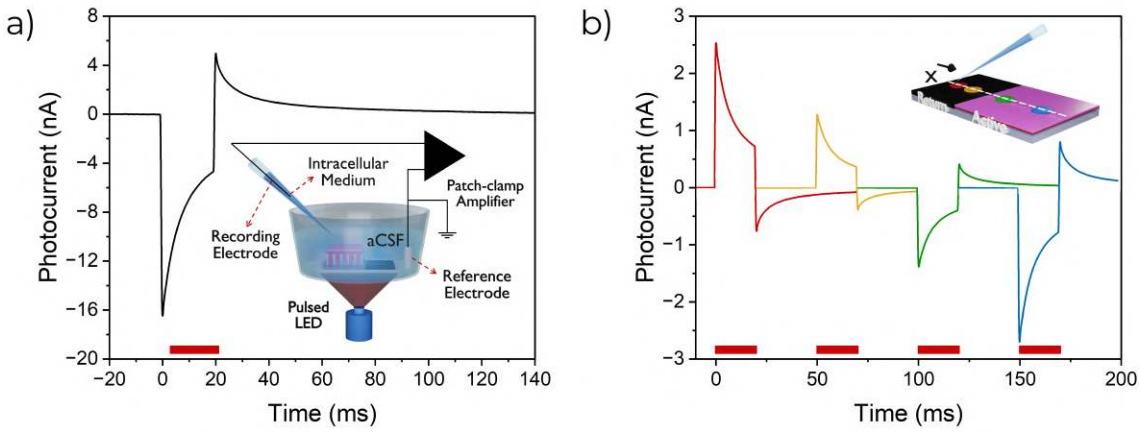

Figure 4.18: **Patch-clamp measurements.** a) Photocurrent of the nanoassembly characterized by using patch-clamp setup. Inset demonstrates the schematic of the setup. b) Photocurrent profile of the nanoassembly after dicing process as a function of the x axis. Inset shows the measurement system, where the circles designate as the patch pipette position.

Moreover, the photocurrent distribution was mapped by varying the position of a patch pipette from the stimulation electrode to the return electrode. A reversal of the photocurrent was observed, which was attributed to anodic current at the stimulation electrode caused by hole-triggered photocurrent flowing from the surface to the electrolyte and cathodic current at the return electrode. (Figure 4.18b).

4.3.3 Photoelectrical Stability and Biocompatibility

To evaluate the photoelectrical stability of the photovoltaic nanoassembly, we measured its photoresponse after subjecting the devices to accelerated reactive aging, low-temperature sterilization, and repeated photoexcitation. For accelerated aging, they were incubated at 87 °C in an H_2O_2-supplemented artificial cerebrospinal fluid (aCSF) environment. Charge injection performance was assessed at 48-hour intervals, corresponding to a simulated aging period of two months, and after a 24-month equivalent aging period, the biointerface retained $79 \pm 7\%$ of its initial charge injection performance (Figure 4.19a). Low-temperature sterilization—comprising ethanol rinsing, UV sterilization, overnight incubation in cell culture medium, and a second ethanol rinse—did not significantly alter photoelectrical properties, with $87 \pm 2\%$ of charge injection and $83 \pm 3\%$ of photovoltage preserved (Figure 4.19b).

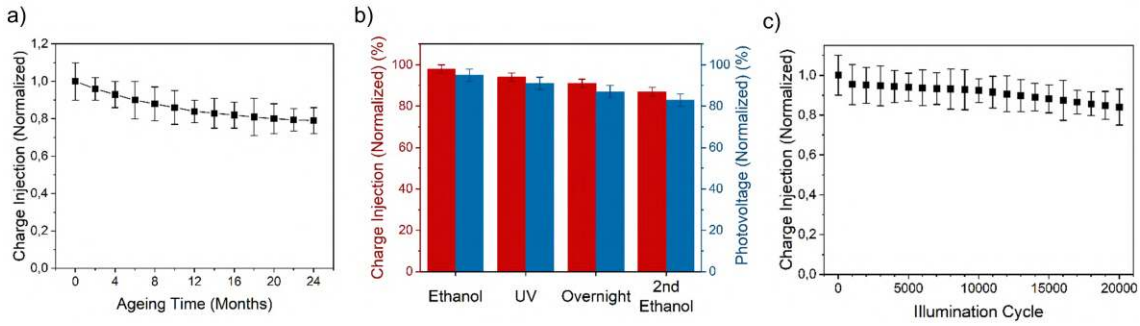

Figure 4.19: **Photoelectrical Stability.** a) Charge injection for different aging times. b) Normalized photovoltage and charge injection after the sterilization steps. c) The photocyclic stability of the interdigitated structure of the nanoassembly, assessed by monitoring the variation in charge injection over 20 000 photo-cycles.

Photostability under repeated excitation (20,000 illumination cycles) was also confirmed, with the biointerface maintaining $84 \pm 9\%$ of its initial charge injection (Figure 4.19c).

For biocompatibility assessment, primary hippocampal neurons cultured on the nanoassembly, or control ITO substrates (Figure 4.20a) were evaluated for viability and cytotoxicity using celltiter-glo (CTG), MTT, and lactate dehydrogenase (LDH) assays. The CTG assay, which measures ATP levels as an indicator of metabolic activity, revealed comparable viability between the device and control groups (Figure 4.20b). The MTT assay indicated higher metabolic activity in neurons cultured on the nanoassembly (Figure 4.20c), while LDH leakage confirmed no membrane integrity compromise or cytotoxicity (Figure 4.20d).

Immunofluorescence staining (NeuN for nuclei, β-III-Tubulin for cytoskeleton) at days 0 and 14 demonstrated sustained neuronal viability and characteristic morphology on the biointerface, with no significant differences in cell distribution compared to controls (Figure 4.20e). Total cell counts followed similar trends, confirming the nanoassembly's compatibility with long-term neuronal culture (Figure 4.21).

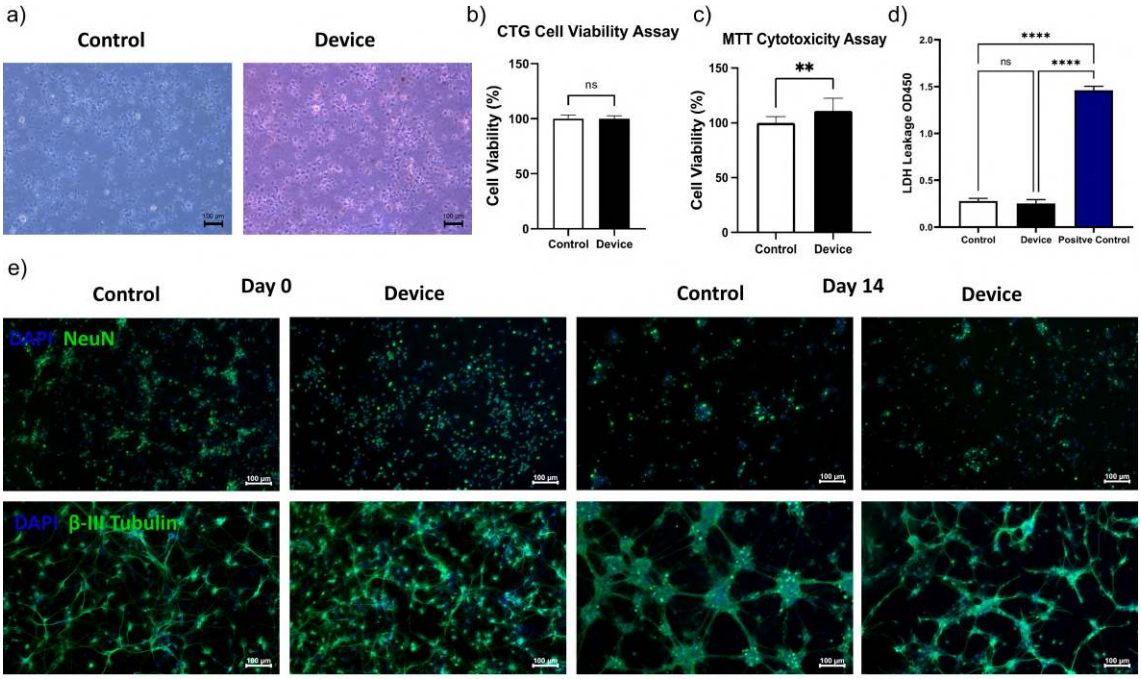

Figure 4.20: **Biocompatibility.** a) Bright field images of cells at DIV 3 (Scale bar, 100 µm). b) CTG assay for quantifying cell viability through cellular ATP level in primary hippocampal neurons cultured on the ITO control and the biointerface device ($mean \pm SD$ n = 4). ITO sample was used as a control. c) MTT assay for measuring cytotoxicity of primary hippocampal neurons cultured on the ITO control and the device ($mean \pm SD$ n = 4). d) LDH leakage assay for measuring cell membrane integrity of neurons on the substrates ($mean \pm SD$ for n = 4). The level of significance was calculated using ordinary one-way ANOVA; *p < 0.05 was evaluated as statistically significant (n.s. p > 0.05, ** p < 0.01, and **** p < 0.0001). e) Short and long-term neuron culture on the control and the device. Cells were co-stained with DAPI (blue) nuclear marker and Anti-NeuN (green) neuronal nuclear marker or Anti-β-III-Tubulin (green) neuronal structure marker (scale bar: 100 µm).

To assess oxidative stress and mitochondrial function, intracellular reactive oxygen species (ROS) were monitored using H_2DCFDA (2′, 7′-dichlorodihydrofluorescein diacetate), a cell-permeant fluorescent probe that is cleaved by ROS to generate emissive DCF (2′, 7′-dichlorofluorescein). Neurons exposed to 10,000 illumination cycles (780 nm, 5 Hz, 20 ms pulse width, 1.5 mW·mm^{-2}) showed no significant ROS increase compared to ITO controls, whereas H_2O_2-treated positive controls exhibited elevated fluorescence (Figure 4.22).

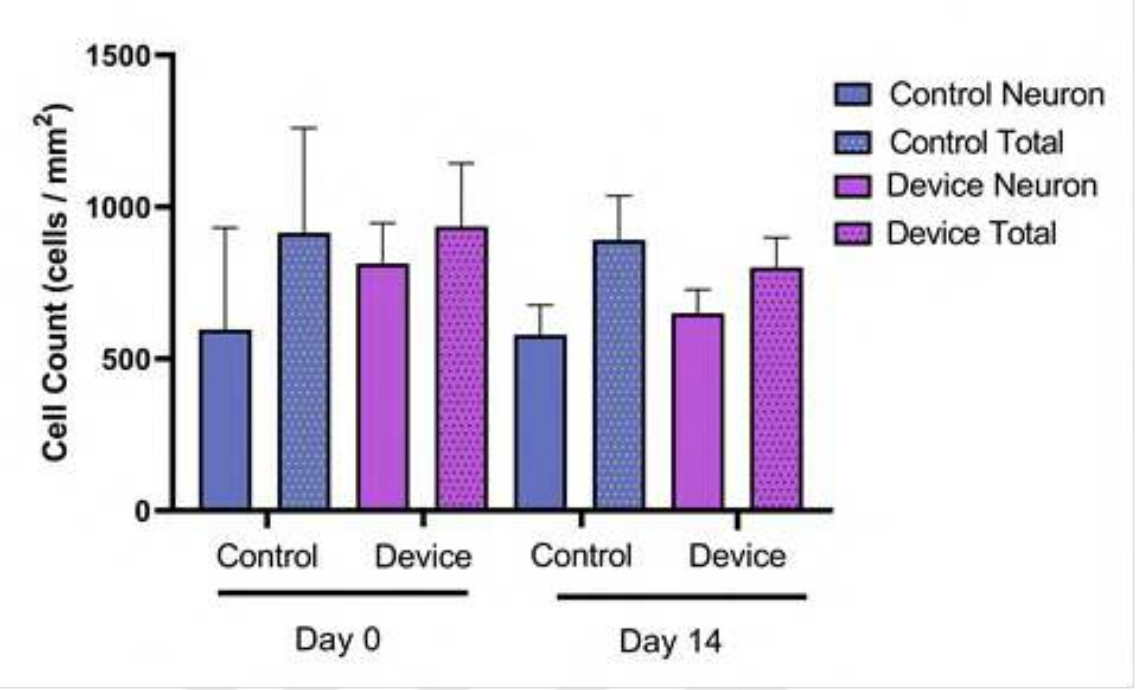

Figure 4.21: **Quantification of the cells.** Quantification of the number of NeuN positive cells and total number of cells per mm^2 for each culture period shown in immunofluorescence images ($mean \pm SD$ n = 8).

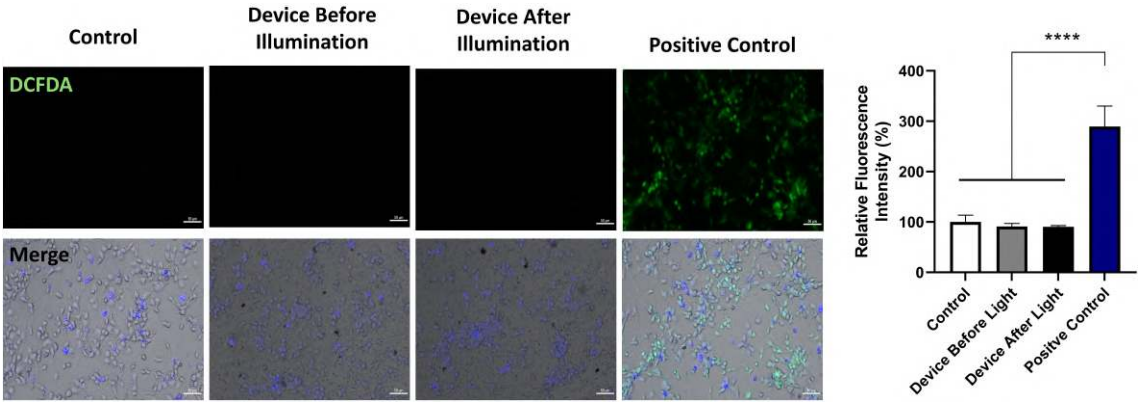

Figure 4.22: **Intracellular oxidative stress measurement.** Evaluation of intracellular oxidative stress with ROS assay after subjecting to 780 nm light with 10000 cycles, illumination: 5 Hz stimulus frequency, 20 ms pulse-width , 1.5 $mW.mm^{-2}$ optical power density. ITO is negative control and ITO with H_2O_2 is positive control (scale bar: 50 µm). The fluorescence intensity of negative control is normalized to 100%. Ordinary one-way ANOVA was used to determine the statistical significance of the differences among multiple groups, and *p < 0.05 was evaluated as statistically significant.

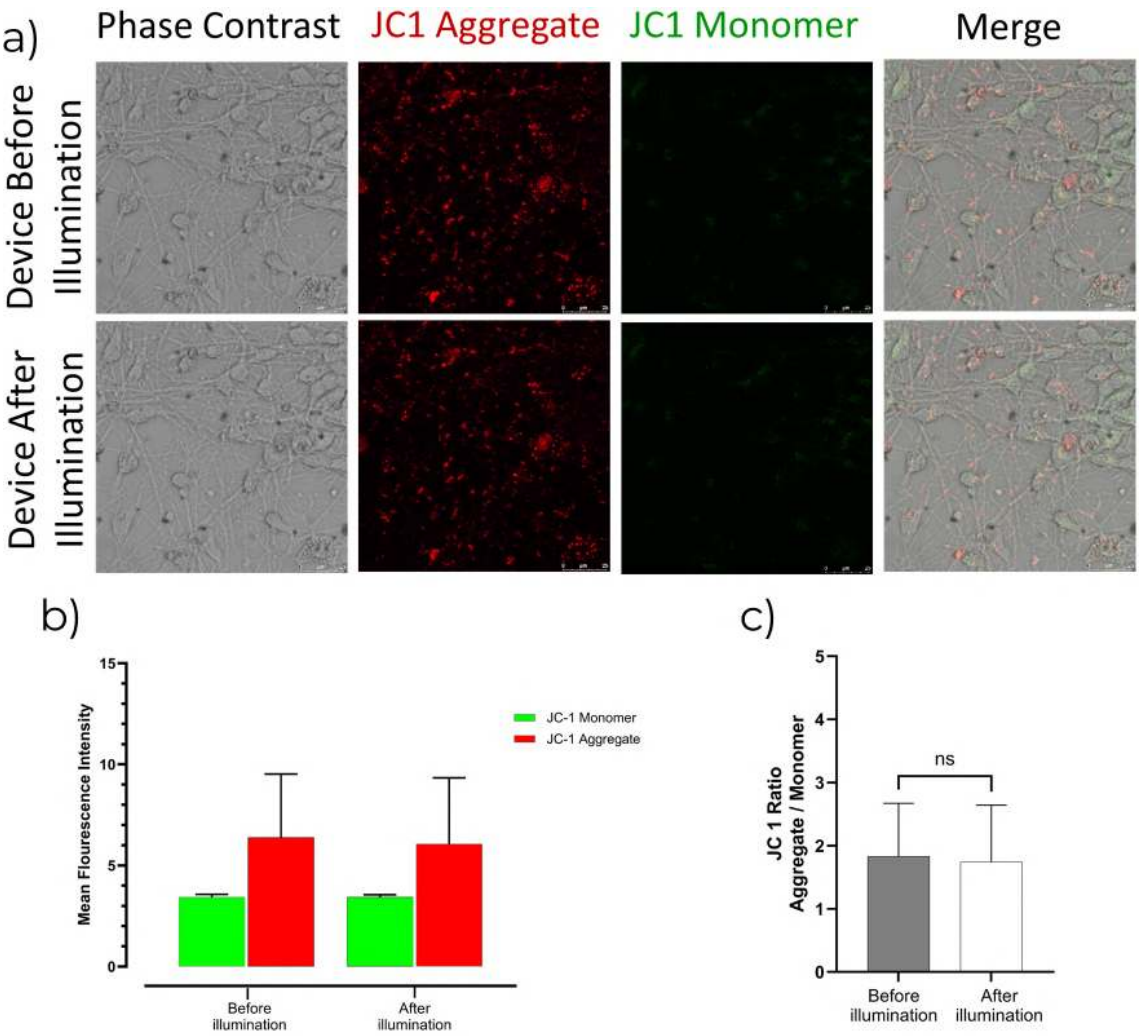

Figure 4.23: **Mitochondrial membrane potential (MMP) assay, JC-1 aggregates (red) refer to healthy mitochondria while JC-1 monomers (green) show disrupted mitochondria.** a) Bright field and fluorescence images of cells cultured on control and devices. Cells were subjected to 780 nm light for 20 sec with 5 Hz stimulus frequency, 20 ms pulse-width , 1.5 $mW.mm^{-2}$ optical power density and visualized under confocal microscopy (Scale bar, 25 µm). b) Mean fluorescence intensity of JC-1 aggregate (red) and monomer (green) in control and device over time. c) Ratio of JC-1 aggregates to JC-1 monomer in the nanoassembly before and after light illumination.

Mitochondrial membrane potential (MMP), a key indicator of mitochondrial health, was assessed using JC-1. Healthy mitochondria retain JC-1 as red aggregates, while depolarized mitochondria exhibit green monomers. After light stimulation (780 nm, 5 Hz, 20 ms pulse width, 1.5 $mW{\cdot}mm^{-2}$), no significant shift in the aggregate-to-monomer ratio was observed (Figure 4.23).

4.3.4 Near-infrared Photostimulation of P23H Blind Rat Retina

To demonstrate the potential of the photovoltaic nanoassembly for restoring visual function, we evaluated its ability to evoke neural activity in the degenerated retina of a blind rat model (P23H), a well-established model for inherited blindness characterized by early photoreceptor degeneration. The retinal explant was placed onto a microelectrode array (MEA) with the photovoltaic implant positioned on the opposite side of the retina, facing the inner nuclear layer (INL) (Figure 4.24). This is one of the standard experimental conditions used to test the PRIMA implants under pre-clinical trials [Prévot et al., 2020]. Full-field NIR light pulses were delivered using a 880 nm light source, a wavelength at which ocular transmittance is high (approximately 80%) and photoreceptor sensitivity is extremely low, which is about 10^{-7} relative to the normalized peak sensitivity at 555 nm [Huang et al., 2021]. The first step of the analysis involved removing stimulation artifacts from the filtered MEA recordings to ensure more accurate spike detection (Figure 4.24).

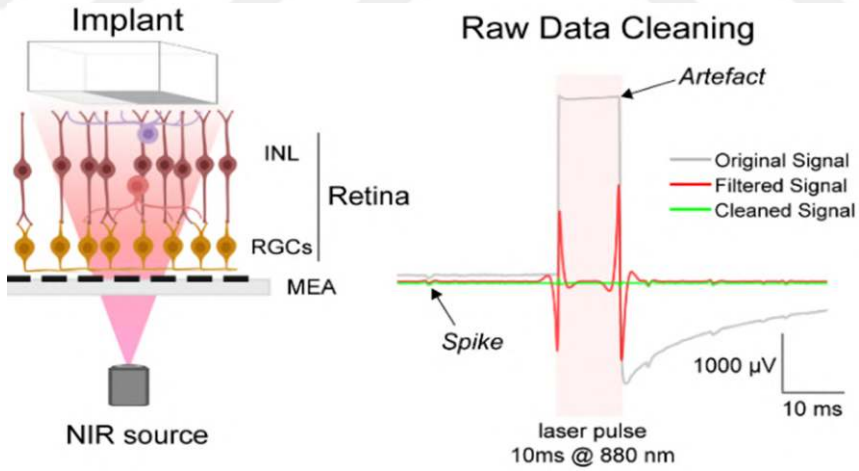

Figure 4.24: **Schematic representation of the experimental setup and raw data cleaning.** A near-infrared (NIR) light source (λ = 880 nm) stimulates the retinal explant through a photovoltaic implant placed on the retinal surface (left). The retinal ganglion cells (RGCs) are recorded using a 16x16 microelectrode array (MEA). The raw data undergoes cleaning (right) to remove artifacts caused by laser stimulation. The original signal is represented in gray, the filtered signal in red, and the cleaned signal in green.

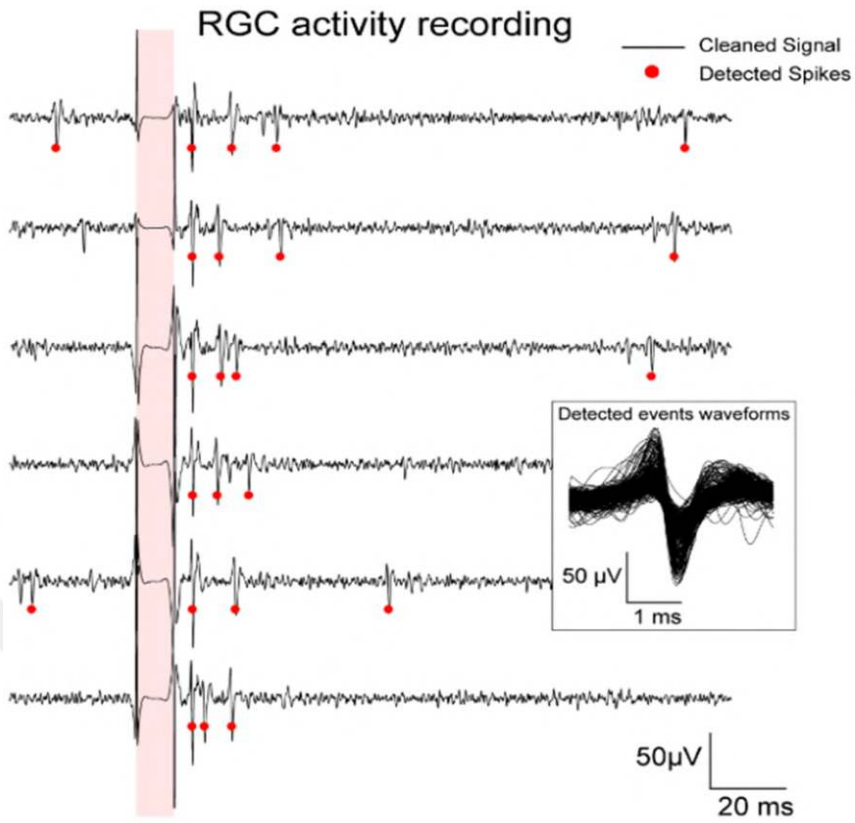

Figure 4.25: **Electrophysiological recordings from a blind rat retinal explant coupled with the photovoltaic device during NIR light stimulations.** Representative recording from NIR stimulation replicates (data from one MEA unit). Cleaned signals are shown with detected spikes marked by red dots. The inset displays the waveforms of all detected events (from 100 replicates). An increased spiking activity is clearly visible following laser pulses.

Of the 13 animals tested with the implants, 6 experiments were performed under conditions in which both the spontaneous retinal activity remained stable for a sufficient duration and the implant–retina contact was tight enough to elicit significant neuronal responses to NIR stimulation (along with positive-polarity saturating artifacts). We observed robust neural activation of RGCs following NIR stimulation (Figure 4.25a), and spatial mapping of RGC responses (Figure 4.25b) revealed localized activation, with higher response amplitudes observed in regions of the MEA in proximity to the photovoltaic nanoassembly part generating anodic photocurrents. Examples of mean firing responses from individual units (Figure 4.26) demonstrated time-locked spiking activity with high temporal precision following stimulation onset.

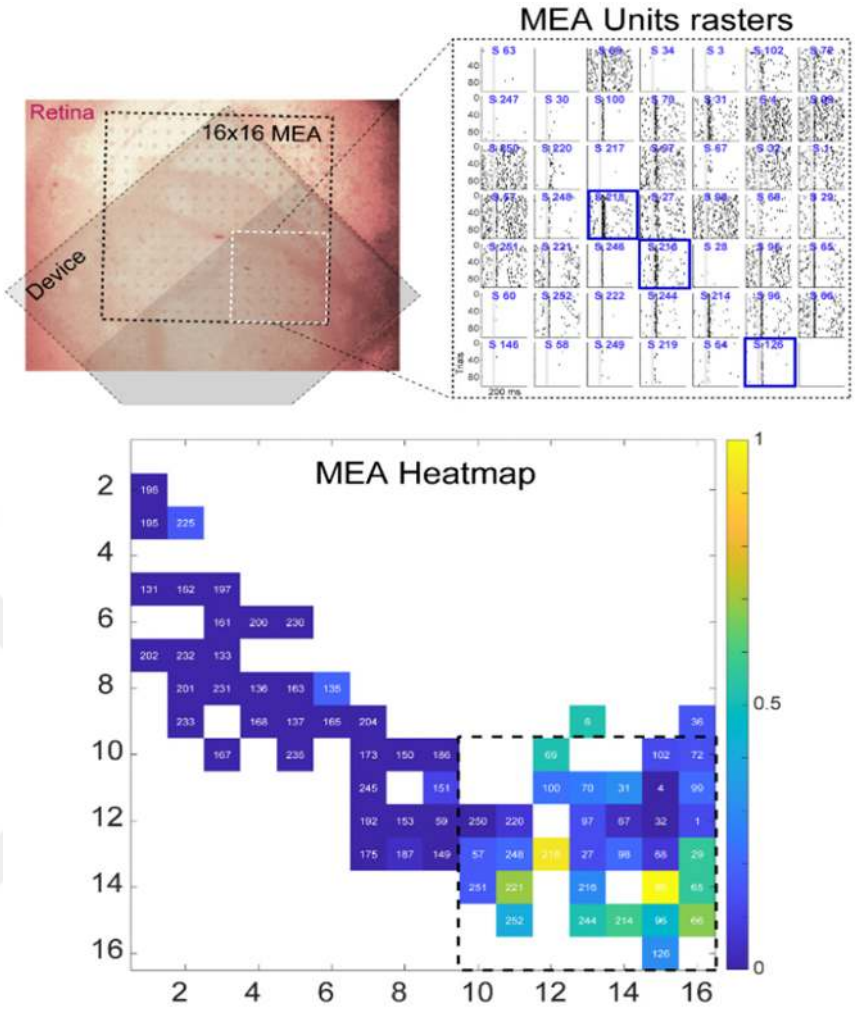

Figure 4.26: **Spatial mapping of retinal responses.** Top left: Infrared image of the retinal explant positioned over the 16x16 MEA grid, with the device represented in gray. Top right: Raster plots (black dots) showing spiking activity across multiple units during repeated stimulations (dotted white square area from top left). The vast majority of units are responsive and respond robustly in this area. Bottom: Spatial heatmap illustrating the normalized response amplitude across units (between 0: dark blue for non-responsive units and 1: yellow for the unit presenting the max response), with higher responses localized to the bottom right region of the MEA.

To investigate the impact of NIR pulse width on retinal responses, we quantified RGC activity across multiple retinas stimulated with varying pulse durations (5 ms, 10 ms, 20 ms, and 50 ms). Because laser stimulation saturates MEA sites, spikes occurring during the stimulation period are not detectable in our recordings, which directly affects the shape of the observed response profiles.

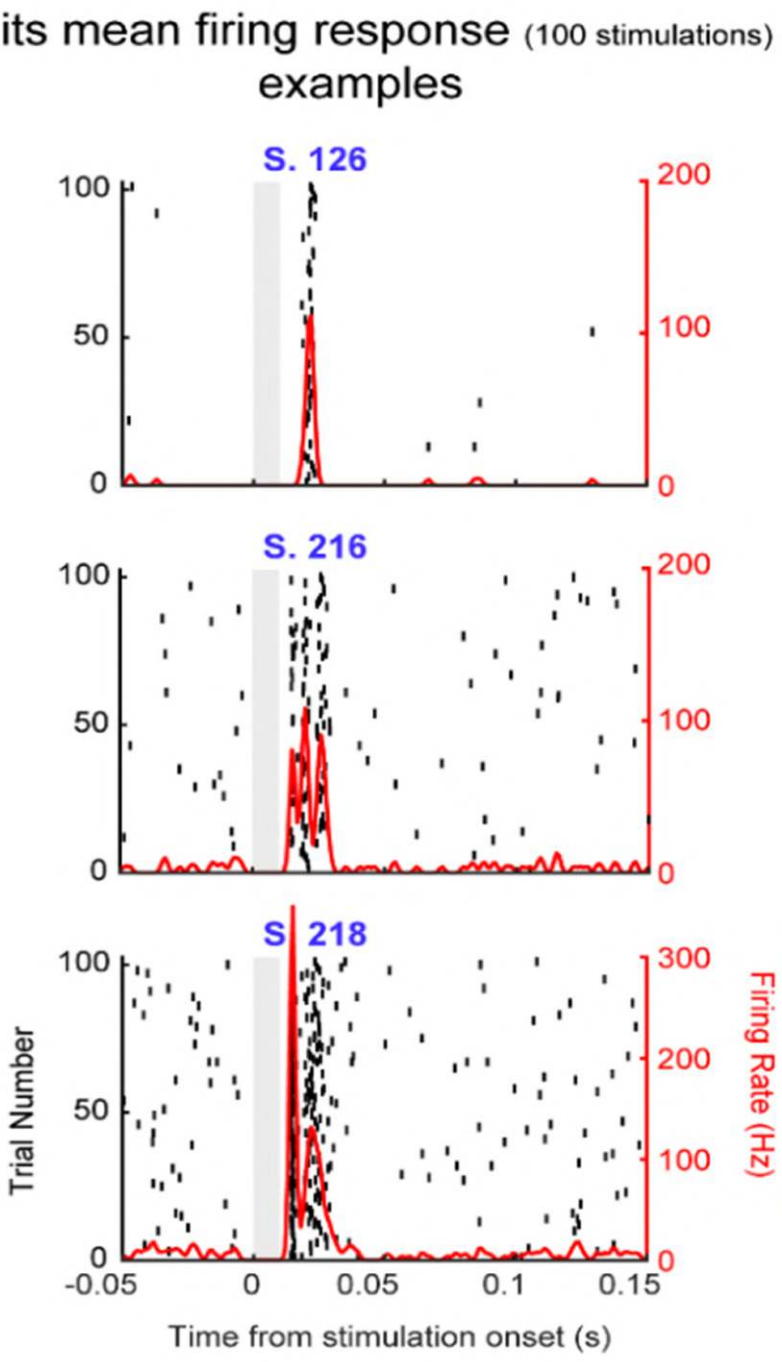

Figure 4.27: **Firing response.** Examples of raster plots and mean firing rates (red curves) from three individual units over 100 stimulation trials, demonstrating robust and time-locked responses to NIR stimulation onset.

As shown in Figures 4.28 and 4.29, in a representative retina, shorter pulses already elicited high firing rates and activated a greater number of responsive units compared to longer pulses (20-50 ms).

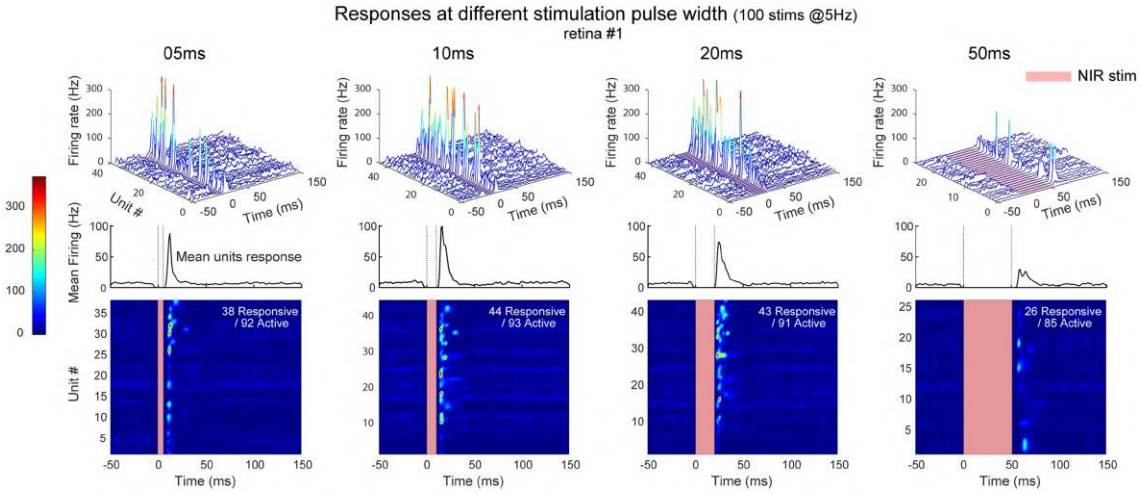

Figure 4.28: **Effect of NIR stimulation duration on retinal responses in rat retina.** Retinal responses to different NIR stimulation pulse widths (5 ms, 10 ms, 20 ms, and 50 ms) in a representative retina. Top: 3D plots of firing rates overtime for all responsive units. Middle: Mean firing rate across all units. Bottom: Heatmaps of units activity over time, with the number of active (displaying spontaneous activity) and responsive units indicated for each condition. Longer pulse widths (> 20ms) result in fewer responsive units, because spikes cannot be detected during laser artifacts in our conditions.

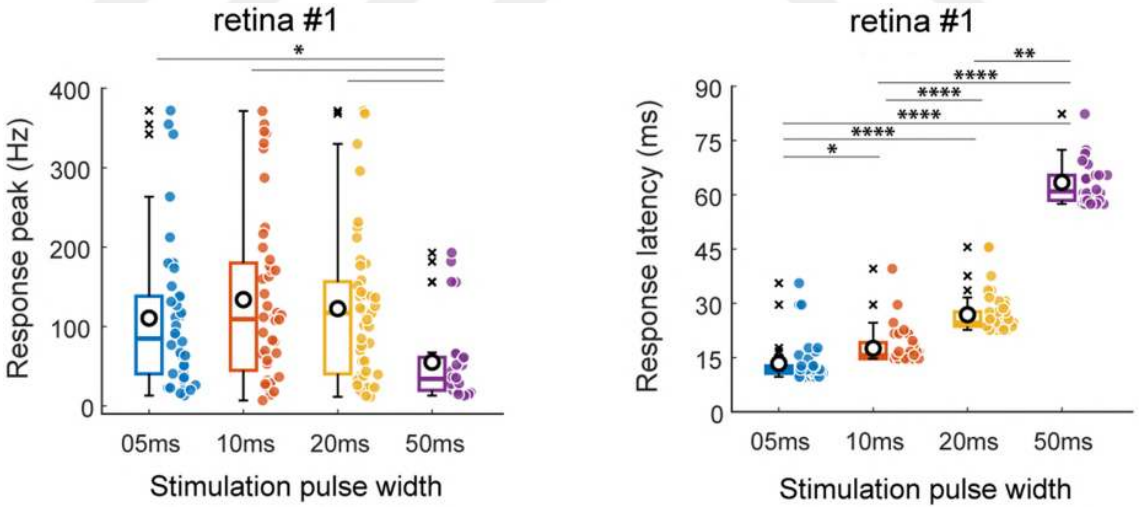

Figure 4.29: **Quantification of response peak and latency for different stimulation pulse widths in a representative retina.** Boxplots (black circles indicate the mean value) and individual data points showing the distribution of peak firing rates and latencies across units, with higher peaks and shorter latencies observed for shorter pulses. The level of significance was calculated using a Kruskal-Wallis test followed by multiple comparisons; *p < 0.05 was evaluated as statistically significant (* p < 0.05, ** p< 0.01 and **** p< 0.0001).

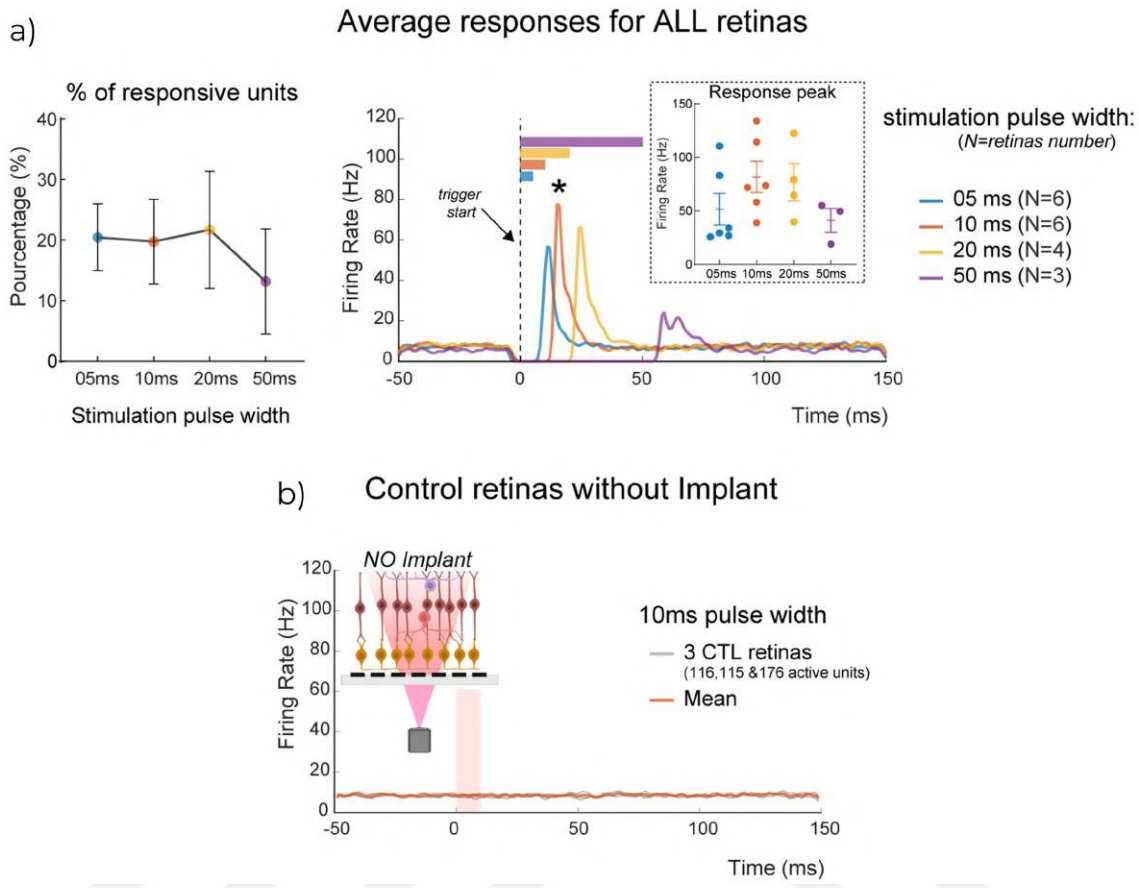

Figure 4.30: **Effect of NIR stimulation duration on retinal responses, and controls in rat retina.** a) Average responses across all retinas. Left: Percentage of responsive units (resp. units/active units*100) as a function of stimulation pulse width for all retinas (mean ± SEM). Right: Mean firing rate curves for all retinas (N = number of retinas per condition), highlighting the consistent responses at all tested pulses widths (with a peak at 10 ms marked with an black asterisk). Top Right Inset: Plot of response peaks across conditions (each dot represents a retina, and individual units firing peak values were calculated before averaging them) for all retinas (mean ± SEM). b) Control experiments. Control recordings from blind rat retinas without implant under 10 ms stimulation show no significant responses (3 control retinas are represented, displaying 116, 115, and 176 active sites, respectively), confirming the necessity of the photovoltaic device for eliciting retinal responses. A constant light intensity of 2.27 $mW.mm^{-2}$ was used for all experiments.

Shorter pulse widths (5, 10, and 20 ms) produced significantly higher peak firing rates (compared to 50 ms) and shorter response latencies across all group comparisons. With the shortest pulses (5 ms), where we believe that most elicited spikes were captured (outside of the short blind window of saturation), the measured response latency was very fast (13.38 ± 0.95 ms, $mean \pm SEM$ n = 38 units).

Taken together, responses across all tested retinas (Figure 4.30a, N = 6 retinas) showed that on average 20% of active sites responded to NIR stimulation, with 10 ms pulses yielding the highest peak firing rates (81.83±14.51 Hz, $mean \pm SEM$ N = 6 retinas). Importantly, control experiments using retinas without implants showed no significant activity under identical stimulation conditions (no responsive sites, N = 3 retinas), confirming that the observed responses were specific to photovoltaic stimulation (Figure 4.30b).

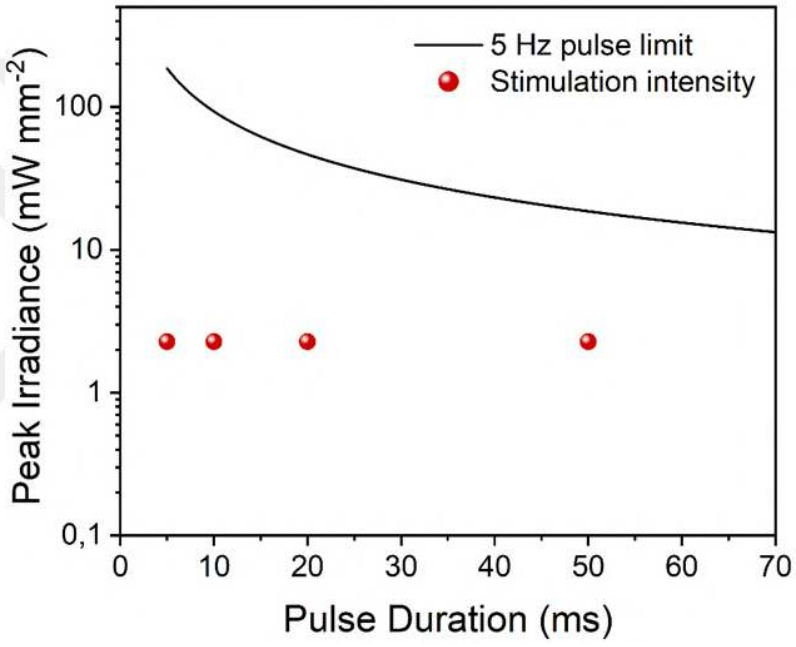

Figure 4.31: **Optical safety considerations.** Maximum permissible exposure limit calculated according to ocular safety standards for 880 nm at 5 Hz.

These results demonstrate that short NIR pulse durations (5-10 ms) enable robust retinal activation, likely due to an already efficient charge injection. Shorter pulses are also preferable for minimizing potential photodamage and thermal effects. Moreover, the light intensity at 2.27 mW.mm^{-2} at 880 nm remained below the safety threshold of the light intensity for retina applications (Figure 4.30). The observed temporal precision and fast response kinetics were achieved with full-field device stimulation. Together, these results demonstrate the capability of the device to safely, effectively, and reliably activate retinal neurons *exvivo*.

4.3.5 Discussion

Retinal degenerative diseases are among the leading causes of vision loss worldwide, and with the aging global population, it is estimated that these conditions will affect 300 million people by 2040. Currently, no definitive clinical treatment exists to prevent or cure these diseases once they develop. While companies like Alpha IMS and Argus II have discontinued their retinal implant technologies, photovoltaic retina implants (i.e., PRIMA) hold high promise for providing artificial vision to patients with retinal degenerative diseases [Palanker et al., 2022]. These implants convert incoming infrared radiation, which is not detected by the damaged photoreceptors, into subretinal photostimulation. For that, silicon photodiode based implants were mainly preferred for effective retinal photostimulation. However, the low absorption coefficient of silicon in the near-infrared (NIR) window requires a thick photoactive region (30 µm). Instead, the photovoltaic nanoassembly has a sub-micron (ca. 0.5 µm) active device thickness that has high potential for translation toward large-area devices.

The key-enabler of the photovoltaic nanoassembly is $AgBiS_2$ NCs, which are non-toxic, composed of earth-abundant elements, have broad absorption spectrum spanning from the visible to near-infrared region, high air stability, and favorable solution processability [Onal et al., 2024]. A particularly important feature of $AgBiS_2$ NCs is their high absorption coefficient ($\tilde{}10^5$ cm^{-1}), which is substantially higher than the other NCs such as CdTe, GaAs, InP, and perovskites over a broad spectral range (400–1000 nm). This high absorption coefficient allows for effective light absorption and thin device architectures while maintaining highly effective functionality.

Layer by layer assembly of nanomaterials is an adaptable and economical approach with nanoscale precision [Rowland et al., 2024]. It enables the deposition of nanocomponents onto various surfaces with complex geometries, such as the integration of nanocrystals (NCs) with nanowires (NWs), as demonstrated in this study [Balamur et al., 2025]. This approach can further add advanced functionalities, including

antimicrobial, wound healing, drug delivery, and tissue engineering capabilities [dos Santos et al., 2024]. Moreover, beyond retina, the photovoltaic nanoassemblies show high promise for the application of a wide range of electrogenic tissues such as heart, muscle, and brain [Li et al., 2024, Prominski et al., 2022].

4.3.6 Conclusion

In conclusion, this work establishes a high-performance photovoltaic nanoassembly based on ZnO nanowires sensitized with $AgBiS_2$ nanocrystals as a safe and efficient platform for near-infrared neural stimulation. By leveraging capacitive charge injections and optimizing nanowire morphology and nanocrystal integration, the system achieves high charge injection densities at low NIR intensities. Demonstrated effectiveness in evoking retinal responses in ex vivo models of blindness highlights its potential for next-generation visual prosthetics and broader neuromodulation applications.

Chapter 5

NEAR-INFRARED SENSITIVE NANOWIRE-BASED TANDEM PHOTODIODES USING QUANTUM DOTS FOR NEXT-GENERATION RETINAL IMPLANTS

5.1 Introduction

Retinal degeneration, a leading cause of severe vision impairment and blindness, is prominently exemplified by age-related macular degeneration and genetic retinitis pigmentosa. These conditions affect more than a million people worldwide, and with an aging population, the number of cases keeps growing. In these diseases, photoreceptors, the cells responsible for turning light into electrical signals, gradually break down and stop functioning. However, a critical advantage lies in the preservation of the remaining retinal neural network, suggesting that targeted stimulation of these intact pathways could restore visual function.

Emerging next-generation retinal prostheses based on colloidal quantum dots (QDs) present a high potential. These nanomaterials, already well-established in display technologies and photovoltaics, offer significant potential as neural interface components. In this work, we developed a photovoltaic device utilizing silver bismuth sulfide ($AgBiS_2$) QDs, which exhibit a higher absorption coefficient in the near-infrared (NIR) region compared to other QDs, such as lead sulfide (PbS), cadmium telluride (CdTe), perovskites, and silicon-based alternatives while avoiding toxic-heavy-metals.

The fabricated single-cell devices exhibited strong capacitive photocurrents even under low-intensity NIR illumination. To further increase the open-circuit voltage (V_{OC}) for more effective ionic stimulation, we developed a tandem photodiode ar-

chitecture. This design features a gold interconnecting layer that serially links the bottom and top photodiodes while maintaining optical transparency. The resulting ZnO NW/$AgBiS_2$ QD-based tandem device achieved over a two-fold enhancement in V_{OC} under identical illumination conditions. Additionally, the optimized photodiode structure significantly improved charge injection in artificial cerebrospinal fluid (aCSF), demonstrating its potential for efficient neural stimulation.

5.2 Methods

5.2.1 Single-cell Photodiode Fabrication

The synthesis of $AgBiS_2$ QDs was carried out following the same procedure detailed in Chapter 4. For the fabrication of single-cell photodiodes, the methodologies outlined in Chapter 3 were adopted, which included ITO substrate cleaning, ZnO seed layer deposition, ZnO NW synthesis, and $AgBiS_2$ QD deposition. Specifically, the growth time for ZnO NWs was optimized to 15 minutes to achieve a consistent nanowire length of 100 ± 10 nm. At this stage, the key requirement is for the top and bottom photodiode cells to exhibit similar or identical absorption capacities. Given that light excitation is applied from the rear of the device, the top photodiode architecture must be designed with greater thickness to enhance absorption. Conversely, the bottom photodiode structure requires thinner layers to balance the overall absorption profile. To achieve this, shorter nanowires were incorporated into the single-cell photodiode design. Following nanowire growth, a variety of spin-coating cycles were conducted to optimize the QD capping layer thickness deposited over the ZnO NWs. A QD concentration of 20 g/L was utilized during device fabrication. Finally, a Poly(3-hexylthiophene-2,5-diyl) (P3HT) coating was applied following the procedure outlined in Chapter 4 to establish the single-cell photodiode structure. Through this optimization process, three spin-coating cycles of QDs were identified as the optimal condition for device performance.

5.2.2 Tandem Photodiode Fabrication

The tandem photodiode to be fabricated will consist of a first cell (single-cell device) followed by an interconnection layer (gold). Subsequently, a second cell comprising a ZnO seed layer, ZnO NWs, $AgBiS_2$ QDs, and P3HT will be deposited on top of the interconnection layer. A gold layer was deposited as an interconnection layer on single-cell devices using thermal evaporation, a process conducted under high vacuum conditions. As part of optimization studies, gold layers with thicknesses of 2 nm and 3 nm were deposited.

ZnO nanoparticles (NPs) were synthesized, enabling deposition at 100 °C, well below the thermal limit. The NP synthesis involved dissolving zinc acetate (18.3 mg) in 1 ml of dimethyl sulfoxide (DMSO) and separately preparing a solution of tetramethylammonium hydroxide (TMAH, 90.6 mg) in 1 ml of ethanol. These solutions were mixed and stirred at room temperature for 1 h. The resulting NPs were purified via centrifugation (5000 rpm, 10 min) and washed twice with methanol. Afterward, the ZnO NPs were dispersed in butanol at a concentration of 30 mg/ml for use in tandem photodiode fabrication. Finally, the sol-gel solution (15% by volume), utilized for the fabrication of the first cell, was mixed with the synthesized NPs (85% by volume). A ZnO seed layer was then deposited via spin coating at 3000 rpm for 60 seconds, followed by annealing at 100 °C for 30 minutes.

Alternatively, $MgCl_2$-doped ZnO NPs, which also present a low annealing temperature (100 °C), were also used in the fabrication of the second cell. Moreover, $MgCl_2$ passivates surface defects, resulting in enhanced photoelectrochemical performance. For the synthesis, 66.6 mg of $MgCl_2$ was initially dissolved in 1 mL of methanol. Subsequently, 1 mL of synthesized ZnO NPs was mixed with 12 mg of the $MgCl_2$ solution, stirred, and stored at room temperature overnight. Finally, the stored $MgCl_2$-doped NPs (85% by volume) were blended with a sol-gel solution (15% by volume) for use in the second cell. The same recipe was followed for depositing the ZnO seed layer.

For the synthesis of ZnO NWs, the growth duration was optimized as 30 minutes to realize a nanowire length of 240 ± 23 nm, which enables the achievement of greater thickness to enhance light absorption. Then, five spin-coating cycles of the QD solution were performed to provide complete coverage of the ZnO NWs. Subsequently, a P3HT layer was deposited using the same method as in the first-cell fabrication. To achieve a thicker P3HT layer for tandem device applications, a concentration of 40 mg/mL was employed.

5.2.3 Chronoamperometry and Chronopotentiometry Measurements

An Autolab potentiostat galvanostat PGSTAT (Metrohm, Netherlands) system was employed for the photoelectrochemical evaluation of the tandem photodiodes under illumination. The measurements were conducted in a three-electrode configuration, with the photodiode serving as the working electrode, an Ag/AgCl reference electrode, and a platinum rod counter electrode. A 1 cm^2 active area of the photodiode was immersed in modified artificial cerebrospinal fluid (aCSF). Near-infrared-sensitive NW/QD-based photodiodes were optically excited using a 780 nm red LED. Data analysis was carried out using NOVA software, while the optical power density was calibrated using a Newport 843-R optical power meter.

5.3 Results

5.3.1 Photodiode Fabrication and Operation

The tandem photodiode structure consists of a series-connected top (first-cell) and bottom (second-cell) photodiode, integrated via an interconnection layer. To fabricate the single-cell photodiode, first, a 30 nm-thick ZnO sol-gel solution was deposited onto an indium tin oxide (ITO) substrate to form a seed layer using a spin-coating technique. Then, growth of ZnO nanowires (NWs) were enabled by chemical bath deposition method on seed layer. At this stage, the key requirement is for the top and bottom photodiode cells to exhibit similar or identical absorption capacities. Given that light excitation is applied from the rear of the device, the

top photodiode architecture must be designed with greater thickness to enhance absorption. Conversely, the bottom photodiode structure requires thinner layers to balance the overall absorption profile. Thus, shorter nanowires were formed into the single-cell photodiode design. The nanowire length was carefully optimized to around 100 nm through precise control of the growth duration. Synthesis of $AgBiS_2$ quantum dots (QDs), which have high absorption coefficient in near-infrared (NIR), high photostability, and do not contain toxic-heavy-metal elements, was performed by hot injection method. Subsequently, QDs were infiltrated into the ZnO NWs by spin-coating method, which ensure uniform deposition resulting in smooth surface. Finally, a poly(3-hexylthiophene) (P3HT) layer was deposited on the QD-capping layer (QD layer over the NWs) to complete the first-cell structure.

The interconnection layer is a critical component in tandem architectures, as it facilitates the effective series connection between the first and second cells. First, to ensure efficient light transmission, the deposited gold layer must be extremely thin—typically on the scale of a few nanometers. Excessive thickness (tens of nanometers) would significantly reduce light transmittance, resulting in poor performance of the second cell. Additionally, the interconnection layer must exhibit high conductivity and uniform deposition to enable effective recombination of electrons from the second cell with holes from the first cell. Accordingly, gold layers measuring 2 nm and 3 nm in thickness were deposited via thermal evaporation method.

To deposit the ZnO seed layer on the gold electrode, the sol-gel method used for the first cell was unsuitable due to its high annealing temperature (>150 °C), which could degrade the QD layer. As an alternative, ZnO nanoparticles (NPs) and $MgCl_2$-doped ZnO NPs were utilized as a seed layer over the interconnection layer, offering the advantage of a low annealing temperature (100 °C) that remains below the thermal threshold. To enhance the thickness of the second cell, ZnO NWs with an average length of approximately 240 nm were grown. Subsequently, QD and P3HT layers were deposited via spin-coating, completing the fabrication of the second cell and the tandem photodiode structure.

5.3.2 Photoelectrochemical Characterization

The photocurrent and photovoltage were characterized in artificial cerebrospinal fluid using a three-electrode configuration, with an Ag/AgCl reference electrode, a platinum (Pt) counter electrode, and single-cell and tandem photodiodes as the working electrodes. We evaluated single-cell devices as the control group in comparison to tandem photodiodes. The tandem devices were fabricated with varying interconnection layer thicknesses and different electron transport layer compositions for the second-cell. The single-cell exhibited two pronounced spikes during the turn-on and turn-off phases under light illumination, a phenomenon attributed to double-layer-capacitor-based photocurrent generation, which limits the charge injection performance (Figure 5.1). Following the fabrication of the second cell on the interconnection layer, all tandem devices displayed a gradual reduction in decay time within the photocurrent profile upon light activation. This behavior stems from a reversible faradaic charge-transfer-mediated photoresponse, which enhances ionic charge injection efficiency in the electrolyte. Such a mechanism is particularly favorable for safe neurostimulation applications.

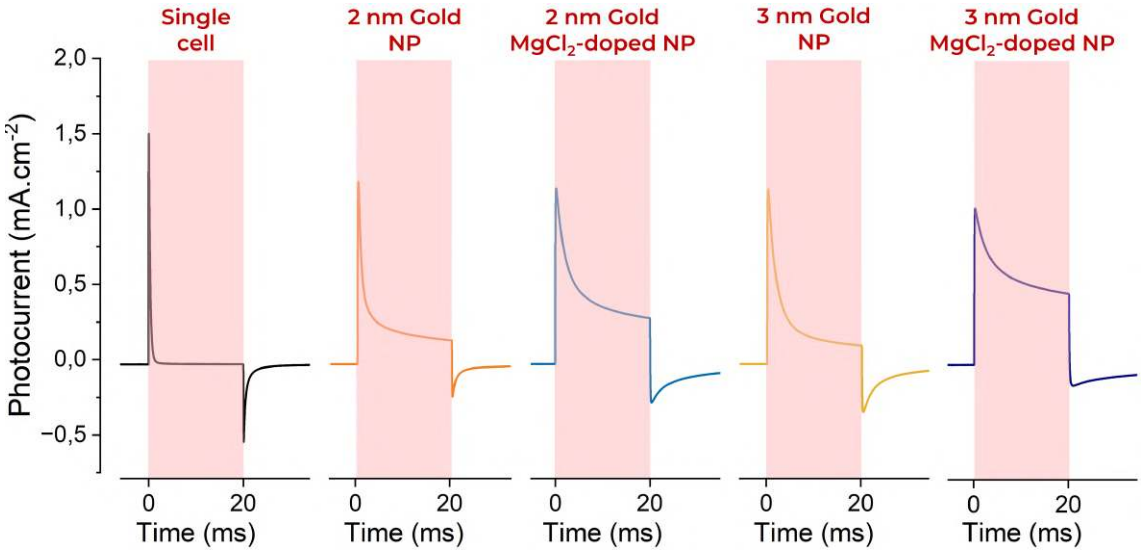

Figure 5.1: **Photocurrent profiles.** Photocurrent density of single-cell and tandem photodiodes with gold interconnection layers of varied thicknesses and different ZnO seed layers ($\lambda = 780$ nm).

The improved charge injection performance in tandem devices, despite a slight decrease in photocurrent with increased Au interconnection layer thickness (from 2 to 3 nm), can be attributed to enhanced interfacial charge transport and reduced recombination losses. A thicker Au layer improves electrical connectivity between sub-cells, facilitating more efficient charge extraction and transfer, thereby boosting faradaic processes critical for neurostimulation. Meanwhile, the superior charge injection performance of $MgCl_2$-doped ZnO NPs over undoped ZnO NPs, despite comparable photocurrent peaks, likely due to improved electronic properties, such as higher conductivity and better energy level alignment, which promote reversible faradaic charge transfer. Doping also passivates surface traps, reducing non-radiative recombination and facilites charge separation. These factors collectively contribute to more effective faradaic-dominated charge injection, which is essential for safe and efficient neuronal stimulation (Table 5.1). Compared to single-cell devices, the tandem photodiodes showed a clear improvement in photovoltage, with performance depending on both the Au interconnection layer thickness and the electron transport layer (ETL) composition.

Table 5.1: Comparative study of tandem vs. single-cell photodiodes: photocurrent, charge density, and photovoltage enhancements.

Photodiode	**Gold Layer**	**ETL**	**Photocurrent ($mA.cm^{-2}$)**	**Charge ($\mu C.cm^{-2}$)**	**Photovoltage (mV)**
Single-cell	-	-	1.3 ± 0.21	0.5 ± 0.1	245 ± 5.2
Tandem	2 nm	Undoped NPs	1.06 ± 0.14	4.51 ± 0.62	389 ± 16.2
Tandem	2 nm	$MgCl_2$-doped NPs	1.03 ± 0.12	7.9 ± 1.1	428 ± 17.8
Tandem	3 nm	Undoped NPs	1.01 ± 0.13	4.65 ± 0.56	487 ± 12.9
Tandem	3 nm	$MgCl_2$-doped NPs	0.92 ± 0.1	10.2 ± 1.51	520 ± 16.5

The weakest response came from the device with a 2 nm Au layer and undoped ZnO NPs, while increasing the Au thickness to 3 nm (still with undoped ZnO) led to a slight but measurable increase, likely due to better charge transfer between the two sub-cells. Replacing the undoped ZnO with $MgCl_2$-doped ZnO NPs further boosted performance, with the 2 nm Au/doped device surpassing both undoped configurations. Most strikingly, the tandem device combining a 3 nm Au interconnection layer and $MgCl_2$-doped ZnO NPs delivered a photovoltage more than twice as high as that of the single-cell devices (Figure 5.2). This substantial improvement likely arises from synergistic effects: (1) the thicker Au interconnection layer minimizes resistive losses and enhances inter-sub-cell charge coupling, while (2) $MgCl_2$ doping optimizes the ZnO NP ETL's work function, reduces interfacial defects, and improves charge extraction efficiency. Together, these modifications elevate the quasi-Fermi level splitting across the tandem structure, thereby maximizing the achievable photovoltage.

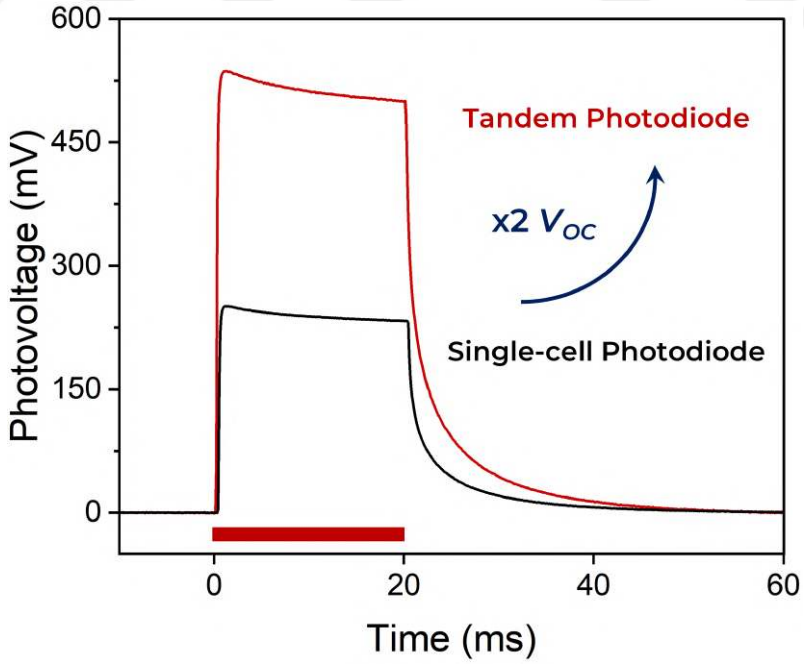

Figure 5.2: **Photovoltage profiles.** Photovoltage of single-cell and tandem photodiode (λ = 780 nm).

5.3.3 Discussion

This study demonstrates that ZnO NW/$AgBiS_2$ QD-based tandem photodiodes significantly enhance photovoltage and charge injection compared to single-cell devices. The optimized tandem structure, featuring a thin gold (Au) interconnecting layer (2–3 nm) and $MgCl_2$-doped ZnO NPs, improved faradaic charge transfer, which is critical for efficient neural stimulation. Morever, alternative interconnecting materials, such as ITO or PEDOT:PSS, could be explored in future studies to enhance optical transparency and electrical conductivity while reducing fabrication complexity. Further optimizations in QD layer thickness and ZnO NW length may also improve device performance. A thicker QD layer could improve the light absorption, while varying NW length could fine-tune charge transport and interfacial properties. Additionally, alternative QD deposition techniques (e.g., layer-by-layer assembly) may improve film uniformity and stability.

5.3.4 Conclusion

The tandem photodiode architecture with ZnO NWs and $AgBiS_2$ QDs demonstrates a high potential for retinal prostheses, achieving over two-fold increase in photovoltage and efficient faradaic charge injection. Future work should explore alternative interconnecting layers (ITO, PEDOT:PSS) and further optimize QD thickness and ZnO NW morphology to maximize device performance. Future work must focus on in vivo validation to evaluate the biocompatibility and long-term stability for clinical translation. With further development could facilitate next-generation prostheses to restore vision in retinal degeneration.

Chapter 6

CONCLUSION

Neurological disorders represent one of the most pressing global health challenges, necessitating innovative therapeutic strategies to restore lost sensory and motor functions. Bioelectronic medicine has emerged as a transformative approach, leveraging electrical stimulation to modulate neural activity and offer potential treatments for previously incurable conditions. Among these, retinal degenerative diseases, including age-related macular degeneration (AMD) and retinitis pigmentosa (RP), pose a significant burden, with millions affected globally and no established clinical interventions to halt or reverse photoreceptor loss. Retinal prostheses have shown promise in restoring partial vision, yet existing technologies face limitations in power efficiency, invasiveness, and long-term viability.

This thesis advances the field of bioelectronic medicine by introducing novel optoelectronic interfaces based on quantum dots (QDs) and nanowires (NWs) for safe, precise, and efficient near-infrared (NIR) neural modulation. In the first study, we designed a multifunctional $AgBiS_2$ QD-based biointerface that simultaneously functions as a photoabsorber, charge storage medium, and electrode-electrolyte interface with pseudocapacitive characteristics. This design enables efficient photostimulation of hippocampal neurons while minimizing oxidative stress, validating its potential as a high-performance neural interface.

Building upon these findings, the second study integrated RuO_2 with ZnO NW / $AgBiS_2$ QD nanoassemblies to create a near-infrared (NIR)-sensitive optoelectronic platform. The ZnO NWs were grown using the seeded growth method due to its ability to produce high-quality, cost-effective, and scalable fabrication, while the synthesis of QDs was accomplished using the hot-injection method. The optimized

length and thickness of the ZnO NWs and $AgBiS_2$ QD layer, were determined to meet the established threshold for charge injection, which was then validated in ex vivo retinal explants from a blind rat model. These results underscore the translational potential of this platform for vision restoration and neuroprosthetic applications.

Finally, the third study addressed the inherent voltage limitations of single-cell photodiodes by introducing a tandem photodiode architecture with an optically transparent gold interlayer. This innovation resulting in two-fold increase in the the open-circuit voltage (Voc) under NIR illumination while improving charge injection performance in physiologically relevant environments, further expanding the applicability of these devices in neural stimulation.

Collectively, this thesis contributes a versatile and high-performance framework for next-generation bioelectronic interfaces. By combining innovative material design, optoelectronic engineering, and neural modulation strategies, these studies enable for advanced neuroprosthetics, artificial vision systems, and broader applications in bioelectronic medicine. Future research should focus on in vivo validation, and clinical translation to bring these technologies closer to therapeutic implementation. Ultimately, this work represents a significant step toward addressing the unmet needs of patients with neurological and sensory impairments, offering hope for restoring lost functions and improving quality of life.

BIBLIOGRAPHY

[Aman et al., 2023] Aman, S., Alahmari, S. D., Khan, S. A., Al-Sehemi, A. G., Ejaz, S. R., Ahmad, N., Alharbi, F., Sadaf, A., and Farid, H. M. T. (2023). Hydrothermal development of bimetallic sulfide nanostructures as an electrode material for supercapacitor application. *Energy & Fuels*, 37(22):17473–17483.

[Anoshkin et al., 2024] Anoshkin, S. S., Sapozhnikova, E. V., Feng, Y., Ju, Y., Pavlov, A., Polozkov, R. G., Yulin, A., Zhong, H., and Pushkarev, A. P. (2024). Blue-emitting cs (pb, cd) br3 nanocrystals resistant to electric field-induced ion segregation. *ACS applied materials & interfaces*, 16(9):11656–11664.

[Arnold, 2018] Arnold, A. (2018). The evolution of bioelectronic medicine. *Set point medical*, pages 1–16.

[Balamur et al., 2024a] Balamur, R., Eren, G. O., Kaleli, H. N., Karatum, O., Kaya, L., Hasanreisoglu, M., and Nizamoglu, S. (2024a). A retina-inspired optoelectronic synapse using quantum dots for neuromorphic photostimulation of neurons. *Advanced Science*, 11(18):2401753.

[Balamur et al., 2025] Balamur, R., Kaya, T. S., Sariyer, S., Kaleli, H. N., Onal, A., Caliskan, U. B., Hasanreisoğlu, M., Demir-Cakan, R., and Nizamoglu, S. (2025). Biointerfacing with agbis2 quantum dots for pseudocapacitive photostimulation. *Advanced Functional Materials*, page 2422083.

[Balamur et al., 2024b] Balamur, R., Oh, J. T., Karatum, O., Wang, Y., Onal, A., Kaleli, H. N., Pehlivan, C., Sahin, A., Hasanreisoglu, M., Konstantatos, G., et al. (2024b). Capacitive and efficient near-infrared stimulation of neurons via an ultrathin agbis2 nanocrystal layer. *ACS Applied Materials & Interfaces*, 16(23):29610–29620.

[Balci Leinen et al., 2018] Balci Leinen, M., Dede, D., Khan, M. U., Caglayan, M., Kocak, Y., Demir, H. V., and Ozensoy, E. (2018). Cdte quantum dot-functionalized p25 titania composite with enhanced photocatalytic no2 storage selectivity under uv and vis irradiation. *ACS Applied Materials & Interfaces*, 11(1):865–879.

[Bernechea et al., 2016] Bernechea, M., Cates, N., Xercavins, G., So, D., Stavrinadis, A., and Konstantatos, G. (2016). Solution-processed solar cells based on environmentally friendly agbis2 nanocrystals. *Nature Photonics*, 10(8):521–525.

[Bloch et al., 2019] Bloch, E., Luo, Y., and da Cruz, L. (2019). Advances in retinal prosthesis systems. *Therapeutic advances in ophthalmology*, 11:2515841418817501.

[Brus, 1984] Brus, L. E. (1984). Electron–electron and electron-hole interactions in small semiconductor crystallites: The size dependence of the lowest excited electronic state. *The Journal of chemical physics*, 80(9):4403–4409.

[Castagnola et al., 2015] Castagnola, V., Descamps, E., Lecestre, A., Dahan, L., Remaud, J., Nowak, L. G., and Bergaud, C. (2015). Parylene-based flexible neural probes with pedot coated surface for brain stimulation and recording. *Biosensors and Bioelectronics*, 67:450–457.

[Cen and Ng, 2018] Cen, L.-P. and Ng, T. K. (2018). Stem cell therapy for retinal ganglion cell degeneration. *Neural Regeneration Research*, 13(8):1352–1353.

[Chang et al., 2022] Chang, C.-H., Chen, K.-T., Hsieh, Y.-Y., Chang, C.-B., and Tuan, H.-Y. (2022). Crystal facet and architecture engineering of metal oxide nanonetwork anodes for high-performance potassium ion batteries and hybrid capacitors. *ACS nano*, 16(1):1486–1501.

[Cheng et al., 2018] Cheng, J. J., Chuang, C.-H. M., Hentz, O., Rekemeyer, P. H., Bawendi, M. G., and Gradecak, S. (2018). Dimension-and surface-tailored zno nanowires enhance charge collection in quantum dot photovoltaic devices. *ACS Applied Energy Materials*, 1(5):1815–1822.

[Cogan, 2008] Cogan, S. F. (2008). Neural stimulation and recording electrodes. *Annu. Rev. Biomed. Eng.*, 10(1):275–309.

[Courtney et al., 2016] Courtney, C. M., Goodman, S. M., McDaniel, J. A., Madinger, N. E., Chatterjee, A., and Nagpal, P. (2016). Photoexcited quantum dots for killing multidrug-resistant bacteria. *Nature materials*, 15(5):529–534.

[Cui et al., 2023] Cui, H., Zhao, S., and Hong, G. (2023). Wireless deep-brain neuromodulation using photovoltaics in the second near-infrared spectrum. *Device*, 1(4).

[De Bastiani et al., 2021] De Bastiani, M., Mirabelli, A. J., Hou, Y., Gota, F., Aydin, E., Allen, T. G., Troughton, J., Subbiah, A. S., Isikgor, F. H., Liu, J., et al. (2021). Efficient bifacial monolithic perovskite/silicon tandem solar cells via bandgap engineering. *Nature Energy*, 6(2):167–175.

[Delori et al., 2007] Delori, F. C., Webb, R. H., and Sliney, D. H. (2007). Maximum permissible exposures for ocular safety (ansi 2000), with emphasis on ophthalmic devices. *Journal of the Optical Society of America A*, 24(5):1250–1265.

[Demir et al., 2011] Demir, H. V., Nizamoglu, S., Erdem, T., Mutlugun, E., Gaponik, N., and Eychmüller, A. (2011). Quantum dot integrated leds using photonic and excitonic color conversion. *Nano Today*, 6(6):632–647.

[Deng et al., 2019] Deng, J., Su, Y., Liu, D., Yang, P., Liu, B., and Liu, C. (2019). Nanowire photoelectrochemistry. *Chemical reviews*, 119(15):9221–9259.

[Diedenhofen et al., 2019] Diedenhofen, S. L., Bernechea, M., Felter, K. M., Grozema, F. C., and Siebbeles, L. D. (2019). Charge photogeneration and transport in agbis2 nanocrystal films for photovoltaics. *Solar RRL*, 3(8):1900075.

[Diroll et al., 2023] Diroll, B. T., Hua, M., Guzelturk, B., Pálmai, M., and Tomczak, K. (2023). Long-lived and bright biexcitons in quantum dots with parabolic band potentials. *Nano Letters*, 23(24):11975–11981.

[dos Santos et al., 2024] dos Santos, V. L., Araújo, R. C., Lisboa, E. S., Lopes, A. M., de Albuquerque-Júnior, R. L., Cardoso, J. C., Blanco-Llamero, C., Deshpande, T. A., Anderson, H. O., Priefer, R., et al. (2024). Layer-by-layer assembly: a versatile approach for tailored biomedical films and drug delivery. *Journal of Drug Delivery Science and Technology*, 91:105243.

[Feigin et al., 2019] Feigin, V. L., Nichols, E., Alam, T., Bannick, M. S., Beghi, E., Blake, N., Culpepper, W. J., Dorsey, E. R., Elbaz, A., Ellenbogen, R. G., et al. (2019). Global, regional, and national burden of neurological disorders, 1990–2016: a systematic analysis for the global burden of disease study 2016. *The Lancet Neurology*, 18(5):459–480.

[Flatae et al., 2019] Flatae, A. M., Tantussi, F., Messina, G. C., De Angelis, F., and Agio, M. (2019). Plasmon-assisted suppression of surface trap states and enhanced band-edge emission in a bare cdte quantum dot. *The journal of physical chemistry letters*, 10(11):2874–2878.

[Fu et al., 2016] Fu, T.-M., Hong, G., Zhou, T., Schuhmann, T. G., Viveros, R. D., and Lieber, C. M. (2016). Stable long-term chronic brain mapping at the single-neuron level. *Nature methods*, 13(10):875–882.

[Fujishima and Honda, 1972] Fujishima, A. and Honda, K. (1972). Electrochemical photolysis of water at a semiconductor electrode. *nature*, 238(5358):37–38.

[Han et al., 2021] Han, M., Bahmani Jalali, H., Yildiz, E., Qureshi, M. H., Şahin, A., and Nizamoglu, S. (2021). Photovoltaic neurointerface based on aluminum antimonide nanocrystals. *Communications Materials*, 2(1):19.

[Han et al., 2022a] Han, M., Karatum, O., and Nizamoglu, S. (2022a). Optoelectronic neural interfaces based on quantum dots. *ACS Applied Materials & Interfaces*, 14(18):20468–20490.

[Han et al., 2020] Han, M., Srivastava, S. B., Yildiz, E., Melikov, R., Surme, S., Dogru-Yuksel, I. B., Kavakli, I. H., Sahin, A., and Nizamoglu, S. (2020). Organic

photovoltaic pseudocapacitors for neurostimulation. *ACS applied materials & interfaces*, 12(38):42997–43008.

[Han et al., 2022b] Han, M., Yildiz, E., Kaleli, H. N., Karaz, S., Eren, G. O., Dogru-Yuksel, I. B., Senses, E., Şahin, A., and Nizamoglu, S. (2022b). Tissue-like optoelectronic neural interface enabled by pedot: Pss hydrogel for cardiac and neural stimulation. *Advanced Healthcare Materials*, 11(8):2102160.

[Huang et al., 2021] Huang, T. W., Kamins, T. I., Chen, Z. C., Wang, B.-Y., Bhuckory, M., Galambos, L., Ho, E., Ling, T., Afshar, S., Shin, A., et al. (2021). Vertical-junction photodiodes for smaller pixels in retinal prostheses. *Journal of neural engineering*, 18(3):036015.

[Jakešová et al., 2024] Jakešová, M., Kunovskỳ, O., Gablech, I., Khodagholy, D., Gelinas, J., and Głowacki, E. D. (2024). Coupling of photovoltaics with neurostimulation electrodes—optical to electrolytic transduction. *Journal of Neural Engineering*, 21(4):046003.

[Jakešová et al., 2019] Jakešová, M., Silverå Ejneby, M., erek, V., Schmidt, T., Gryszel, M., Brask, J., Schindl, R., Simon, D. T., Berggren, M., Elinder, F., et al. (2019). Optoelectronic control of single cells using organic photocapacitors. *Science advances*, 5(4):eaav5265.

[Jalali et al., 2022] Jalali, H. B., Sadeghi, S., Dogru Yuksel, I. B., Onal, A., and Nizamoglu, S. (2022). Past, present and future of indium phosphide quantum dots. *Nano Research*, 15(5):4468–4489.

[Jin et al., 2024] Jin, L., Selopal, G. S., Tong, X., Perepichka, D. F., Wang, Z. M., and Rosei, F. (2024). Heavy-metal-free colloidal quantum dots: Progress and opportunities in solar technologies. *Advanced Materials*, 36(33):2402912.

[Karatum et al., 2021] Karatum, O., Aria, M. M., Eren, G. O., Yildiz, E., Melikov, R., Srivastava, S. B., Surme, S., Dogru, I. B., Bahmani Jalali, H., Ulgut, B.,

et al. (2021). Nanoengineering inp quantum dot-based photoactive biointerfaces for optical control of neurons. *Frontiers in neuroscience*, 15:652608.

[Karatum et al., 2023] Karatum, O., Gwak, M.-J., Hyun, J., Onal, A., Koirala, G. R., Kim, T.-i., and Nizamoglu, S. (2023). Optical neuromodulation at all scales: from nanomaterials to wireless optoelectronics and integrated systems. *Chemical Society Reviews*, 52(10):3326–3352.

[Karatum et al., 2022a] Karatum, O., Kaleli, H. N., Eren, G. O., Sahin, A., and Nizamoglu, S. (2022a). Electrical stimulation of neurons with quantum dots via near-infrared light. *ACS nano*, 16(5):8233–8243.

[Karatum et al., 2022b] Karatum, O., Yildiz, E., Kaleli, H. N., Sahin, A., Ulgut, B., and Nizamoglu, S. (2022b). Ruo2 supercapacitor enables flexible, safe, and efficient optoelectronic neural interface. *Advanced Functional Materials*, 32(31):2109365.

[Khan et al., 2019] Khan, M. D., Aamir, M., Sohail, M., Bhoyate, S., Hyatt, M., Gupta, R. K., Sher, M., and Revaprasadu, N. (2019). Electrochemical investigation of uncapped agbis 2 (schapbachite) synthesized using in situ melts of xanthate precursors. *Dalton Transactions*, 48(11):3714–3722.

[Kim et al., 2020] Kim, T., Kim, K.-H., Kim, S., Choi, S.-M., Jang, H., Seo, H.-K., Lee, H., Chung, D.-Y., and Jang, E. (2020). Efficient and stable blue quantum dot light-emitting diode. *Nature*, 586(7829):385–389.

[Kim et al., 2013] Kim, T.-i., McCall, J. G., Jung, Y. H., Huang, X., Siuda, E. R., Li, Y., Song, J., Song, Y. M., Pao, H. A., Kim, R.-H., et al. (2013). Injectable, cellular-scale optoelectronics with applications for wireless optogenetics. *Science*, 340(6129):211–216.

[Ko et al., 2020] Ko, J. S., Lai, C.-H., Long, J. W., Rolison, D. R., Dunn, B., and Nelson Weker, J. (2020). Differentiating double-layer, psuedocapacitance, and

battery-like mechanisms by analyzing impedance measurements in three dimensions. *ACS applied materials & interfaces*, 12(12):14071–14078.

[Ko et al., 2018] Ko, J. S., Sassin, M. B., Parker, J. F., Rolison, D. R., and Long, J. W. (2018). Combining battery-like and pseudocapacitive charge storage in 3d mno x@ carbon electrode architectures for zinc-ion cells. *Sustainable Energy & Fuels*, 2(3):626–636.

[Krogstrup et al., 2013] Krogstrup, P., Jørgensen, H. I., Heiss, M., Demichel, O., Holm, J. V., Aagesen, M., Nygard, J., and Fontcuberta i Morral, A. (2013). Single-nanowire solar cells beyond the shockley–queisser limit. *Nature photonics*, 7(4):306–310.

[Kuncel and Grill, 2004] Kuncel, A. M. and Grill, W. M. (2004). Selection of stimulus parameters for deep brain stimulation. *Clinical neurophysiology*, 115(11):2431–2441.

[Kurra et al., 2021] Kurra, N., Uzun, S., Valurouthu, G., and Gogotsi, Y. (2021). Mapping (pseudo) capacitive charge storage dynamics in titanium carbide mxene electrodes in aqueous electrolytes using 3d bode analysis. *Energy Storage Materials*, 39:347–353.

[Lee et al., 2022] Lee, J. S., Kim, J., Ye, Y.-s., and Kim, T.-i. (2022). Materials and device design for advanced phototherapy systems. *Advanced Drug Delivery Reviews*, 186:114339.

[Li et al., 2024] Li, P., Zhang, J., Hayashi, H., Yue, J., Li, W., Yang, C., Sun, C., Shi, J., Huberman-Shlaes, J., Hibino, N., et al. (2024). Monolithic silicon for high spatiotemporal translational photostimulation. *Nature*, 626(8001):990–998.

[Liao et al., 2023] Liao, Z., Mallem, K., Prodanov, M. F., Kang, C., Gao, Y., Song, J., Vashchenko, V. V., and Srivastava, A. K. (2023). Ultralow roll-off quantum dot light-emitting diodes using engineered carrier injection layer. *Advanced Materials*, 35(47):2303950.

[Liu et al., 2015] Liu, J., Fu, T.-M., Cheng, Z., Hong, G., Zhou, T., Jin, L., Duvvuri, M., Jiang, Z., Kruskal, P., Xie, C., Suo, Z., Fang, Y., and Lieber, C. M. (2015). Syringe-injectable electronics. *Nature Nanotechnology*, 10(7):629–636.

[Liz-Marzán et al., 2023] Liz-Marzán, L. M., Artzi, N., Bals, S., Buriak, J. M., Chan, W. C., Chen, X., Hersam, M. C., Kim, I.-D., Millstone, J. E., Mulvaney, P., et al. (2023). Celebrating a nobel prize to the "discovery of quantum dots, an essential milestone in nanoscience".

[Marshall and Schnitzer, 2013] Marshall, J. D. and Schnitzer, M. J. (2013). Optical strategies for sensing neuronal voltage using quantum dots and other semiconductor nanocrystals. *Acs Nano*, 7(5):4601–4609.

[Matea et al., 2017] Matea, C. T., Mocan, T., Tabaran, F., Pop, T., Mosteanu, O., Puia, C., Iancu, C., and Mocan, L. (2017). Quantum dots in imaging, drug delivery and sensor applications. *International journal of nanomedicine*, pages 5421–5431.

[Mathieson et al., 2012] Mathieson, K., Loudin, J., Goetz, G., Huie, P., Wang, L., Kamins, T. I., Galambos, L., Smith, R., Harris, J. S., Sher, A., et al. (2012). Photovoltaic retinal prosthesis with high pixel density. *Nature photonics*, 6(6):391–397.

[Mei et al., 2022] Mei, A., Xu, Z., Wang, X., Liu, Y., Chen, J., Fan, J., and Shi, Q. (2022). Photocatalytic materials modified with carbon quantum dots for the degradation of organic pollutants under visible light: A review. *Environmental Research*, 214:114160.

[Merrill et al., 2005] Merrill, D. R., Bikson, M., and Jefferys, J. G. (2005). Electrical stimulation of excitable tissue: design of efficacious and safe protocols. *Journal of neuroscience methods*, 141(2):171–198.

[Muqit et al., 2024] Muqit, M. M. K., Le Mer, Y., de Koo, L. O., Holz, F. G., Sahel, J. A., and Palanker, D. (2024). Prosthetic visual acuity with the prima subretinal

microchip in patients with atrophic age-related macular degeneration at 4 years follow-up. *Ophthalmology Science*, 4(5):100510.

[Nikoloudakis et al., 2022] Nikoloudakis, E., López-Duarte, I., Charalambidis, G., Ladomenou, K., Ince, M., and Coutsolelos, A. G. (2022). Porphyrins and phthalocyanines as biomimetic tools for photocatalytic h 2 production and co 2 reduction. *Chemical Society Reviews*, 51(16):6965–7045.

[Norris and Bawendi, 1996] Norris, D. J. and Bawendi, M. (1996). Measurement and assignment of the size-dependent optical spectrum in cdse quantum dots. *Physical Review B*, 53(24):16338.

[Onal et al., 2024] Onal, A., Kaya, T. S., Metin, O., and Nizamoglu, S. (2024). Emergence of near-infrared photoluminescence via zns shell growth on the agbis2 nanocrystals. *Chemistry of Materials*, 37(1):255–265.

[Palanker et al., 2022] Palanker, D., Le Mer, Y., Mohand-Said, S., and Sahel, J.-A. (2022). Simultaneous perception of prosthetic and natural vision in amd patients. *Nature communications*, 13(1):513.

[Pappas et al., 2007] Pappas, T. C., Wickramanyake, W. S., Jan, E., Motamedi, M., Brodwick, M., and Kotov, N. A. (2007). Nanoscale engineering of a cellular interface with semiconductor nanoparticle films for photoelectric stimulation of neurons. *Nano letters*, 7(2):513–519.

[Parameswaran et al., 2018] Parameswaran, R., Carvalho-de Souza, J. L., Jiang, Y., Burke, M. J., Zimmerman, J. F., Koehler, K., Philips, A. W., Yi, J., Adams, E., Bezanilla, F., et al. (2018). Photoelectrochemical modulation of neuronal activity with free-standing coaxial silicon nanowires. *Biophysical Journal*, 114(3):393a.

[Parameswaran et al., 2019] Parameswaran, R., Koehler, K., Rotenberg, M. Y., Burke, M. J., Kim, J., Jeong, K.-Y., Hissa, B., Paul, M. D., Moreno, K.,

Sarma, N., et al. (2019). Optical stimulation of cardiac cells with a polymer-supported silicon nanowire matrix. *Proceedings of the National Academy of Sciences*, 116(2):413–421.

[Patil and Patil, 2023] Patil, S. S. and Patil, P. S. (2023). 3d bode analysis of nickel pyrophosphate electrode: a key to understanding the charge storage dynamics. *Electrochimica Acta*, 451:142278.

[Patolsky et al., 2006] Patolsky, F., Timko, B. P., Yu, G., Fang, Y., Greytak, A. B., Zheng, G., and Lieber, C. M. (2006). Detection, stimulation, and inhibition of neuronal signals with high-density nanowire transistor arrays. *Science*, 313(5790):1100–1104.

[Prévot et al., 2020] Prévot, P.-H., Gehere, K., Arcizet, F., Akolkar, H., Khoei, M. A., Blaize, K., Oubari, O., Daye, P., Lanoë, M., Valet, M., et al. (2020). Behavioural responses to a photovoltaic subretinal prosthesis implanted in non-human primates. *Nature biomedical engineering*, 4(2):172–180.

[Prominski et al., 2022] Prominski, A., Shi, J., Li, P., Yue, J., Lin, Y., Park, J., Tian, B., and Rotenberg, M. Y. (2022). Porosity-based heterojunctions enable leadless optoelectronic modulation of tissues. *Nature Materials*, 21(6):647–655.

[Ramasamy et al., 2015] Ramasamy, K., Gupta, R. K., Palchoudhury, S., Ivanov, S., and Gupta, A. (2015). Layer-structured copper antimony chalcogenides (cusbse x s2–x): stable electrode materials for supercapacitors. *Chemistry of Materials*, 27(1):379–386.

[Ren et al., 2020] Ren, X., Yu, D., Yuan, L., Bai, Y., Huang, K., Liu, J., and Feng, S. (2020). In situ exsolution of ag from agbis 2 nanocrystal anode boosting high-performance potassium-ion batteries. *Journal of Materials Chemistry A*, 8(30):15058–15065.

[Ronzani et al., 2018] Ronzani, C., Cottineau, T., Gonzalez-Valls, I., Keller, V., Picaud, S., Keller, N., and Roux, M. J. (2018). High-frequency stimulation of normal

and blind mouse retinas using tio2 nanotubes. *Advanced Functional Materials*, 28(50):1804639.

[Rowland et al., 2024] Rowland, S., Aghakhani, A., Whalley, R. D., Ferreira, A. M., Kotov, N., and Gentile, P. (2024). Layer-by-layer nanoparticle assembly for biomedicine: Mechanisms, technologies, and advancement via acoustofluidics. *ACS Applied Nano Materials*, 7(14):15874–15902.

[Sahoo et al., 2023] Sahoo, R. C., Moolayadukkam, S., Seok, J. H., Lee, S. U., and Matte, H. R. (2023). Enhanced charge storage capacity and high rate capabilities of ni 2 co-layered double hydroxides/expanded-graphite composites as anodes for li-ion batteries. *Journal of Materials Chemistry A*, 11(13):7142–7151.

[Sang et al., 2022] Sang, M., Kim, K., Shin, J., and Yu, K. J. (2022). Ultra-thin flexible encapsulating materials for soft bio-integrated electronics. *Advanced Science*, 9(30):2202980.

[Shi et al., 2022] Shi, J., Sun, C., Liang, E., and Tian, B. (2022). Semiconductor nanowire-based cellular and subcellular interfaces. *Advanced Functional Materials*, 32(11):2107997.

[Sun et al., 2023] Sun, P., Xing, Z., Li, Z., and Zhou, W. (2023). Recent advances in quantum dots photocatalysts. *Chemical Engineering Journal*, 458:141399.

[Taal et al., 2023] Taal, A. J., Uguz, I., Hillebrandt, S., Moon, C.-K., Andino-Pavlovsky, V., Choi, J., Keum, C., Deisseroth, K., Gather, M. C., and Shepard, K. L. (2023). Optogenetic stimulation probes with single-neuron resolution based on organic leds monolithically integrated on cmos. *Nature Electronics*, 6(9):669–679.

[Taberna et al., 2003] Taberna, P., Simon, P., and Fauvarque, J.-F. (2003). Electrochemical characteristics and impedance spectroscopy studies of carbon-carbon supercapacitors. *Journal of the Electrochemical Society*, 150(3):A292.

[Tang et al., 2018] Tang, J., Qin, N., Chong, Y., Diao, Y., Yiliguma, Wang, Z., Xue, T., Jiang, M., Zhang, J., and Zheng, G. (2018). Nanowire arrays restore vision in blind mice. *Nature communications*, 9(1):786.

[Tomar et al., 2022] Tomar, A. K., Kshetri, T., Kim, N. H., and Lee, J. H. (2022). Cation and anion (de) intercalation into mxene/perovskite oxides for high-rate intercalation pseudocapacitance. *Energy Storage Materials*, 50:86–95.

[Vagni et al., 2022] Vagni, P., Airaghi Leccardi, M. J. I., Vila, C.-H., Zollinger, E. G., Sherafatipour, G., Wolfensberger, T. J., and Ghezzi, D. (2022). Polyretina restores light responses in vivo in blind göttingen minipigs. *Nature Communications*, 13(1):3678.

[Vázquez-Guardado et al., 2020] Vázquez-Guardado, A., Yang, Y., Bandodkar, A. J., and Rogers, J. A. (2020). Recent advances in neurotechnologies with broad potential for neuroscience research. *Nature neuroscience*, 23(12):1522–1536.

[Wang et al., 2007] Wang, J., Polleux, J., Lim, J., and Dunn, B. (2007). Pseudocapacitive contributions to electrochemical energy storage in tio2 (anatase) nanoparticles. *The Journal of Physical Chemistry C*, 111(40):14925–14931.

[Wang et al., 2022] Wang, Y., Kavanagh, S. R., Burgués-Ceballos, I., Walsh, A., Scanlon, D. O., and Konstantatos, G. (2022). Cation disorder engineering yields agbis2 nanocrystals with enhanced optical absorption for efficient ultrathin solar cells. *Nature Photonics*, 16(3):235–241.

[Xiao et al., 2021] Xiao, Y., Wang, H., Awai, F., Shibayama, N., Kubo, T., and Segawa, H. (2021). Eco-friendly agbis2 nanocrystal/zno nanowire heterojunction solar cells with enhanced carrier collection efficiency. *ACS Applied Materials & Interfaces*, 13(3):3969–3978.

[Yang et al., 2024] Yang, R., Zhao, P., Wang, L., Feng, C., Peng, C., Wang, Z., Zhang, Y., Shen, M., Shi, K., Weng, S., et al. (2024). Assessment of visual

function in blind mice and monkeys with subretinally implanted nanowire arrays as artificial photoreceptors. *Nature Biomedical Engineering*, 8(8):1018–1039.

[Zhang et al., 2021] Zhang, A., Lee, J.-H., and Lieber, C. M. (2021). Nanowire-enabled bioelectronics. *Nano Today*, 38:101135.